THE UNIVERSITY

OF BIRMINGHAM

Terahertz Frequency Doubling Circuits for Communications

David William Glynn

A thesis submitted to the University of Birmingham for the degree of Doctor of Philosophy

School of Electronic, Electrical and Computer Engineering
The University of Birmingham

August 2016

Abstract

Exploitation of the terahertz frequency region offers tantalising rewards over other parts of the congested spectrum, however current technologies and manufacturing methods are not yet commercially effective to capitalise on its riches. This thesis is concerned with developing new techniques to enable and improve radio frequency engineering design for tomorrow's terahertz applications. The techniques in this thesis will provide engineer's the knowledge to creatively tackle some of the challenges when designing at the terahertz scale.

A novel design of a 9 to 18 GHz microstrip diode frequency doubler using the coupling matrix method is presented, which demonstrates new techniques for matching and integration of the circuit components. It illustrates a new approach for diode doubler design and provides a guide for solving the matching and integrating of passive circuits, such as input and output filters, to the active part of a circuit. Complex circuit interactions are controlled in the design, without the traditional reliance on circuit optimisation.

Terahertz manufacturing technologies are investigated, and a 150 GHz E field plane terahertz waveguide using a polymer (SU-8) etching, layering and metal coating technology, is designed, constructed and measured. Such a device would be a fundamental component in a future terahertz frequency communication system.

To M,

For believing in me and always being there.

Acknowledgements

I would like to thank my supervisor, Professor Michael Lancaster for his support, guidance and mentoring during this work within the Emerging Device Technology Group at the University of Birmingham. I also owe a great deal of gratitude to Dr Jeffrey Powell for his advice and insights, and his patience in handing over the knowledge to allow me to complete this project. My thanks also go to Dr Xiaobang Shang for his helpful advice along with practical assistance in the laboratory, and Dr Paul Smith for his additional guidance and advice.

I would also like to thank Donna Johnson for her help, practical guidance and printed circuit board fabrication skills, Dr Yingtao Tian for his SU-8 fabrication prowess, Mary Winkles for her keen organisation and guiding me in the quagmire of administration, and Warren Hay for the metalworking he did for me.

I want to mention the gratitude I have for the support and patience I have received from my wife and family, without whom I would not have been able to even start this great work. And finally I want to thank all those who took the time to give me knowledge on my way here.

Thank you all.

Table of Contents

Page

List of Figures

Page

List of Tables

Page

Chapter 1

Introduction

1.1 Research Motivation

The terahertz region represents the largest unexploited span of the radio spectrum, but very little commercial investigation is ongoing here due to a lack of innovative techniques and devices to capitalise on it. This thesis explains some of the potential rewards and also gives reasons why it has not been straightforward to take advantage of this band of frequencies. There is therefore a requirement for research into techniques and methods to unlock the terahertz spectrum, and allow low cost, large scale manufacture of circuits and devices to improve on the costly and impractical systems that currently operate at terahertz wavelengths.

Microwave filters are essential components for communication systems, required for the rejection of unwanted frequencies that would disrupt the function of the system, and also to prevent emission of frequencies that could interfere with other systems. Tools to assist the design of filters are numerous, with most microwave CAD packages providing a simple parameterised process for the engineer [1,2]. However, as operating frequencies increase into the terahertz region the resonator dimensions and novel structures can force a return to more fundamental design methods such as the coupling matrix method. This method is outlined in Chapter 3 and shows a general bandpass filter design method that can be applied to filter design at any frequency. Knowledge of this method is also later applied in a novel way to assist in the simultaneous design of circuit stages which have complex interactions, such as filters and

frequency multipliers. Previously this would have required designing stages in isolation, or attempting a design with heavy reliance on circuit optimisation.

Many high frequency communication systems use waveguide structures in part, if only as transmission paths, due to their low loss and high isolation attributes. However, waveguide use is denied to low cost, mass produced circuits due to the high expense of manufacture, traditionally using metal machining techniques. Chapter 4 explores a low cost method of manufacturing waveguide using a structure constructed from metal coated layers of polymer which can be built to dimensions exceeding the capabilities of metal machining processes.

Terahertz communication systems face many design challenges, however a major obstacle to overcome is the generation of source frequencies in the terahertz range. There are many methods of terahertz frequency generation [3,4], but to improve upon existing technology that allows low cost mass production, the method investigated here is the multiplication of an efficiently generated lower frequency, up to a higher frequency. This builds on firm foundations and techniques with the benefit of new breakthroughs in device technology to enable higher and higher frequency multiplication [5]. A method of integrating common frequency multiplier components (filters, matching circuits and diodes) using coupling matrix theory is investigated in Chapters 6 and 7, which shows how to design streamlined integrated circuits without the reliance on optimisation. This reduces circuit volume and complexity by sharing resonating elements between circuit stages, providing a useful and flexible technique for terahertz system design.

1.2 Thesis Organisation

This chapter outlines the motivation for this research, which is expanded upon in Chapter 2. This chapter also provides an overview of the whole thesis structure.

Chapter 2 gives an overview of existent terahertz systems and the challenges facing designers hoping to exploit this region. It also highlights the advantages gained by working at terahertz frequencies and why it is worth pursuing, along with a proposed terahertz receiver system design.

Chapter 3 provides theoretical background into the design of microwave bandpass filters and coupling matrix theory. This is used later in the thesis to provide a technique for designing frequency multipliers. Frequency multipliers are essential circuits that require improvement to allow easier exploitation of the terahertz region due to the difficulty of generating high frequencies in this range.

Chapter 4 illustrates the design of a 150 GHz waveguide using SU-8 polymer layers with ninety degree E field plane bends. It shows how to manufacture such circuits and that components built this way could be key to accurate low cost mass production for future terahertz systems.

Chapter 5 illustrates two designs for bandpass filters using coupling matrix methods. The first circuit uses microstrip and the second is a waveguide resonator design. The techniques proven here are to be used in a novel way later, to integrate filters with active circuit components.

Chapter 6 provides theoretical background for varactor diode doubler design and illustrates a crude method of frequency doubler design by optimiser, which is improved upon greatly with techniques shown in subsequent chapters.

Chapter 7 details the design of a shared resonator microstrip frequency doubler. It doubles a 9 GHz fundamental band to 18 GHz, and uses coupling matrix theory to integrate an input and output filter with a shared resonator used by each filter and also the diode mounting. This enables a compact design with no need for impedance transforming circuitry.

Chapter 8 summarises the work in this thesis, and outlines suggestions for future work that could benefit from the research contained here.

Appendix 2 contains a description of a method that uses previous work in this thesis and coupling matrix theory to provide an alternative approach for impedance matching of circuit components such as bandpass filters to active circuit devices. It uses the fact that selecting a particular bandwidth solution for a filter section will allow the selection of a matching impedance, which can be used to provide the best match between circuit stages. This allows the design of a controlled impedance matched circuit and provides a powerful technique for circuit design that can enable creative solutions to engineering problems.

References

[1] Microwave Studio, CST. 2011. "CST GmbH." Darmstadt.

[2] Agilent Advanced Design System[tm]. Keysight Technologies. http://www.keysight.com/

[3] Erik Bründermann, Heinz-Wilhelm Hübers, Maurice FitzGerald Kimmitt. **Terahertz Techniques**, Springer series in optical sciences, 2012

[4] Hamid Khatibi; Ehsan Afshari. **Towards efficient high power mm-wave and terahertz sources in silicon: One decade of progress.** IEEE 17th Topical Meeting on Silicon Monolithic Integrated Circuits in RF Systems, 2017. Pages 4-8.

[5] Jae-Sung Rieh; Daekeun Yoon; Jongwon Yun**. An overview of solid-state electronic sources and detectors for Terahertz imaging**. 12th IEEE International Conference on Solid-State and Integrated Circuit Technology, 2014. Pages 1-4.

Chapter 2

Terahertz Systems

2.1 Introduction

Electromagnetic waves are useful in two basic ways; they can be modulated to convey information or they can be used to gain information about a target by observing their interaction. Terahertz electromagnetic waves differ from other electromagnetic waves only in frequency, however their challenges of scale and their idiosyncrasies when interacting with the environment means their benefits have yet to be capitalized upon.

This chapter outlines some of the limiting considerations and engineering highlights of using terahertz radiation, and how modified electronic technologies from radio frequency engineering disciplines can be employed to manipulate it.

2.2 An Overview of Terahertz

The radio frequency band 300-3000 GHz is defined by the International Telecommunications Union (I.T.U.) [1] as the Terahertz band, or less conventionally termed THF band (Tremendously High Frequency). Microwave textbooks often omit this region, deeming it beyond the reach of their technologies and best left to the optical disciplines. However only a few optical books claim this region, labelling it the lower part of the far infrared. The scarcity of existent terahertz systems reflect this dual discipline no one's land, and those that venture in are forced to assemble

large inefficient constructions using expensive bespoke components, often combining light manipulation with expertly crafted machined microwave devices.

One of the benefits of exploiting the terahertz band can be illustrated by examining Figure 2.1. Figure 2.1 shows how many standard 8 MHz wide Wi-Fi channels that can potentially fit into each of the designated ITU bands.

Wi-Fi currently manages to squeeze a few tens of bands across the UHF / SHF regions competing with radar, cable and satellite broadcasting, DBS, amateur radio, high-frequency microwave radio relay and microwave remote sensing for space. It can be seen from this chart that if the whole of the SHF band was given to Wi-Fi that 5,400 Wi-Fi bands could fit in that space. However the THF region which is currently only used for some scientific research (medicine, spectroscopy, imaging,) and a handful of communication applications, could accommodate 540,000 Wi-Fi channels.

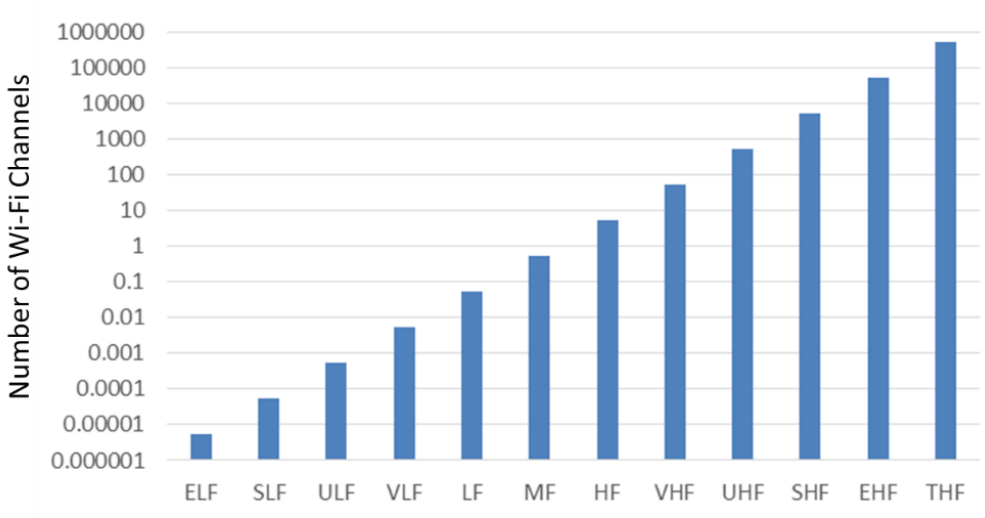

Figure 2.1 - Wi-Fi channels per ITU frequency band

Another way to view the bandwidth advantage of the THF region is if Shannon's theorem is considered, which determines transmission channel capacity *C*

$$C = B\ log_2(1 + S/N) \qquad 2.1$$

Where *B* is the bandwidth and *S/N* is the signal to noise ratio. It can be seen that the most efficient way to increase channel capacity is to increase bandwidth, which can be facilitated by moving into the terahertz region where there is ample bandwidth capacity.

The terahertz spectrum has therefore been a rich territory to conquer and efforts to do so have been on the increase for the last few decades. Proposals for communication systems are numerous [2,3,4,5,6] with some promising results from demonstration systems [7,8,9], which show off the capability for massive data transfer rates. A summary of several approaches and a review of terahertz technologies that may succeed in the construction of terahertz communication systems in the future can be found in papers such as [10]. However, there are good reasons why the majority of terahertz systems that are reported are still design proposals or lab based demonstrators, and these reasons are discussed in the next section

2.3 Design Issues at Terahertz Frequencies

The cost rewards of being able to exploit the huge bandwidth of the terahertz region are potentially colossal, however this frequency band has barely been capitalised yet, and some of the reasons why are discussed in this section.

2.3.1 Terahertz Wave Propagation

No discussion on terahertz communications is complete without a diagram showing atmospheric attenuation of an electromagnetic wave versus frequency that includes the terahertz region. Figure 2.2 [11] shows this attenuation profile, where the red line is the horizontal transmission path attenuation at sea level, and the other black lines show attenuations due to scattering from moisture related events in the atmosphere.

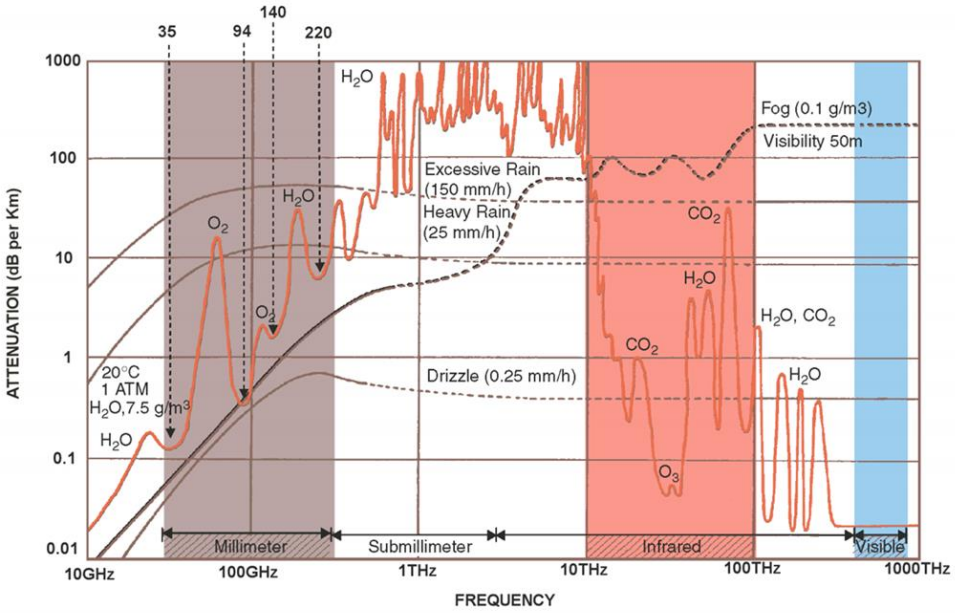

Figure 2.2 - Atmospheric attenuation versus frequency. Taken from [11]

It should be clear from Figure 2.2 that atmospheric attenuation of frequencies in the terahertz range limits propagation distance considerably. To operate with this physical constraint, terahertz waves must either propagate without atmospheric gases or moisture, such as in space, or be limited to applications that require short distances. Moderate distances are still feasible but need high power transmission and have increased demand on receiver sensitivity. For this reason there are not many applications that utilise terahertz waves for long distance propagation, but of

the few these include remote sensing [12] and satellite communications and radio astronomy [13,14,15,16]. Applications that require transmission distances of a few metres are probably where the lower cost, commercially viable terahertz systems are likely to emerge from. Current examples of this include imaging [17,18, 19] spectroscopy [20,21] and wireless data communication, with novel applications in medicine [22,23, 24] and security [25,26]. However one of the main limits to these applications is explained in the next section.

2.3.2 Terahertz Frequency Generation

Most of the aforementioned applications require the local generation of a frequency at or close to the frequency of operation, to use as a reference or a mixing product. Communication systems especially require a locally generated oscillation frequency to convert signals to a lower manageable value or to combine low information signals with a self-generated higher frequency carrier ready for transmission. Imaging and spectroscopy require an oscillating wave to interact with a target material and this must be sourced somehow within the system. However, as frequencies increase, so does the difficulty of generating them, limiting the design of such applications. A common example of the approach of optical frequency generation can be seen in [27] which describes a local oscillator generation for the latest generation of THz astronomical telescopes. This system, if anything highlights the difficulty and complexity of producing this high reference frequency and only specialised applications such as radio astronomy can afford the investment.

Developments in the radio frequency electronics domain have continued to push into the terahertz region with heterodyne receiver systems such as [28,29,30,31], however these efforts are still held back by often having to use expensive and cumbersome Gunn based frequency multipliers to obtain practical high frequency source signals of sufficient power. Gunn oscillators work because they have a negative resistance profile when biased correctly and along with a tuned resonator (usually a precisely machined metal cavity or crystalline sphere) and they can oscillate at very high frequencies with relatively high power. Other similarly cumbersome methods include gyrotrons which have very high power, backward wave oscillators and optically based oscillators which have very lower power but high frequency reach.

There is therefore a need to provide practical high frequency reference signals affordably. The conventional engineering solution to this problem is to use frequency multiplication techniques which take an easily generated low oscillation frequency and upscale it to the desired higher frequency.

Existing implementations of high frequency multipliers include [32, 33, 34, 35] which describe efficient designs to produce frequencies between 125 GHz and 620 GHz using the nonlinear characteristics of diodes for harmonic multiplication. These instances demonstrate that devices and techniques exist to produce terahertz signal sources using the frequency multiplication method and new devices and technology refinements are improving the performance and upper frequency limit all the time. However, each of the above designs do not suit low cost mass reproduction, each requiring precision machining and craftsmanship assembly practices.

Multiplier design consists of separating circuit components and modelling each part separately, combining them later with heavy reliance on optimisation techniques. To reach the highest frequencies, chains of these multiplication stages are required, generating an even greater demand on simulation, optimization and inter-stage impedance matching. While engineering solutions have maintained the efficiencies of each frequency multiplication step, it can be seen that after cascading stages just a few times that very little output power is left [36], which places emphasis on inter-stage amplification and very careful optimising, matching and power budgeting of the overall design. The conclusion of papers such as [37, 38, 39] is that there is a need for new techniques for matching and manufacture if the designs of frequency multipliers are ever to produce commercially cost effective solutions for high production numbers.

2.3.3 Terahertz Frequency Multipliers

Section 2.3.2. gives an overview of the major methods and systems involved with terahertz frequency generation, and this section continues that discussion, focusing on the current state of the art of frequency multipliers for terahertz applications using varactor diode technology. Diodes are good devices to use for frequency multiplication as their technological evolution builds upon commercially successful volume manufacturing processes, and high frequency development can capitalize on this foundation [40].

The upper frequency limit, multiplication efficiency and output power of frequency doublers is improving all the time. Some of the highest frequency diode based multipliers to date include the Jet Propulsion lab 2.75 THz frequency tripler [41] and the Virginia Diodes Inc.

2.7 THz tripler [42], however multiplication efficiencies are less than 2%. Lower down the frequency spectrum is the Advanced Compound Semiconductor Technologies 500GHz multiplier, again with a low efficiency of around 1% [43]. For comparison, the highest efficiency multipliers at terahertz frequencies are the Chalmers University of Technology device which multiplies with an efficiency of 35%, operating at 168 GHz [44], the Farran Technologies 44% efficiency device which operates at 200 GHz [45], the Rutherford Laboratories 96 GHz multiplier with a conversion efficiency of 25% [46], and the University of Virginias 160 GHz multiplier with an efficiency of 29% [47]. These results are summarised in Table 2.1 for ease of comparison, along with a brief description of the diode technology used and fabrication method.

It can be seen that diode based multiplier technology is capable of reaching the terahertz frequencies, with the downside of a low power output due to poor multiplication efficiencies. The low efficiency is usually attributed to dominating parasitics in the diode devices themselves, and the step to a packaged mass produced unit will only worsen this. Therefore much more work is needed before a commercially suitable diode for terahertz frequencies is available. It can also be seen that most of the devices reported use split block machined waveguide housings to mount the devices in. While this is a good method for prototyping, it would be an expensive option for scaled up production volumes. Therefore parallel development is required for more cost efficient housings and waveguide connections for these terahertz circuits, micromachining is an excellent solution here.

Table 2.1 Comparison of Frequency Multipliers

Institution	Operating Freq. (THz)	Efficiency (%)	Fabrication Technology	Diode Technology	Reference
Jet Propulsion Laboratory	2.75	<2	Split block waveguide	4 power combined 6 anode GaAs	[41]
Virginia diodes Inc.	2.7	2	Split block waveguide	Schottky harmonic mixer	[42]
Chalmers university of technology	0.168	35	Membrane mounted circuit	GaAs Schottky	[44]
Faran	0.2	44	Split block waveguide	Anti-series array	[45]
Rutherford Laboratories	0.96	25	Split block waveguide	Anti-series array GaAs diode on quartz substrate	[46]
ACST	0.5	1	Split block waveguide	Anti-parallel diodes	[43]
University of Virginia	0.16	29	Split block waveguide	GaAs Quasi-vertical fabrication	[47]

2.3.4 Terahertz Fabrication

Terahertz wavelengths range from 1 mm to less than 0.1 mm. This assures that any circuit operating at terahertz frequencies will have some part of it requiring construction on a very small scale. While this is a blessing for the engineer who wants to design compact space saving designs, it is the bane of circuit fabricators. With the exception of MMIC manufacture, technologies such as printed circuit board lithography become redundant at these wavelengths due to their dimension constraints and the inability of substrates to handle the propagating modes. The traditional machined metal waveguide structures now become prohibitively expensive and difficult to manufacture due to restrictions on tooling size and manufacturing tolerances overwhelming the construction. For this reason, alternative media are to be investigated for the design of terahertz circuits, to help reduce cost, meet dimension tolerances and eventually enable mass production. Some alternative forms of terahertz fabrication include substrate integrated waveguide, micromachining and 3-D printing.

Substrate integrated waveguide is created using a substrate as the transmission medium, enclosed top and bottom with a metallic cover, and using an enclosing structure along the waveguides lengths, such as regularly spaced metallic vias through the substrate, [48, 49]. This method has an advantage compared to microstrip in that conductor losses are much less. However the potential for leakage losses through the waveguide walls means it is not ideal for use in communication systems. Compared to air filled waveguide, this dielectric transmission method will have greater loss also. Frequencies for circuits using this waveguide method have been reported as high as 340 GHz [50].

Micromachining falls into various categories with conventional computer numerical control techniques struggling to improve upon waveguide dimensions smaller than WR-3 [51]. To try to improve on this, investigations into laser micromachining [52] and also SU-8 micromachining, as discussed in detail in Chapter 4 of this thesis, are attempting to exploit higher frequencies with potential for large volume manufacture.

Another potential fabrication technique is 3-D printing, with good weight saving potential due to low density material use and flexibility of geometry, [53,54]. While this method may have great advantage for novel design structures and low cost volume manufacture, there are significant challenges to overcome such as surface roughness and fine resolution, as well as problems introduced by using materials unfamiliar to the microwave environment. The highest frequencies reported for 3-D printed circuits are around 110 GHz [55].

2.4 Solutions Investigated in this Thesis

This thesis investigates some new design methods and manufacturing technologies to assist in the progression of terahertz system designs. It concentrates on the discussed area of frequency multiplication as well as technologies to assist in the fabrication of such circuits.

One fabrication method that is proposed for the design of a terahertz communication system is the use of SU-8, a polymer layer formed by printed lithographic methods that can be metal coated and built up in layers to form cavities and circuit structures. The details of SU-8 manufacture are discussed in later chapters, but a concept terahertz receiver system drawing can be seen in Figure 2.3. The SU-8 process for circuit fabrication is investigated because it is a low

cost method of manufacture for commercial volumes of circuits as well as having benefits for dimensional tolerance compared to more traditional machining methods.

Figure 2.3 illustrates a SU-8 layered construction that will be explained in more detail in later chapters and shows how the novel technologies developed and demonstrated in this thesis could be brought together to construct a communication system in a compact and cost efficient

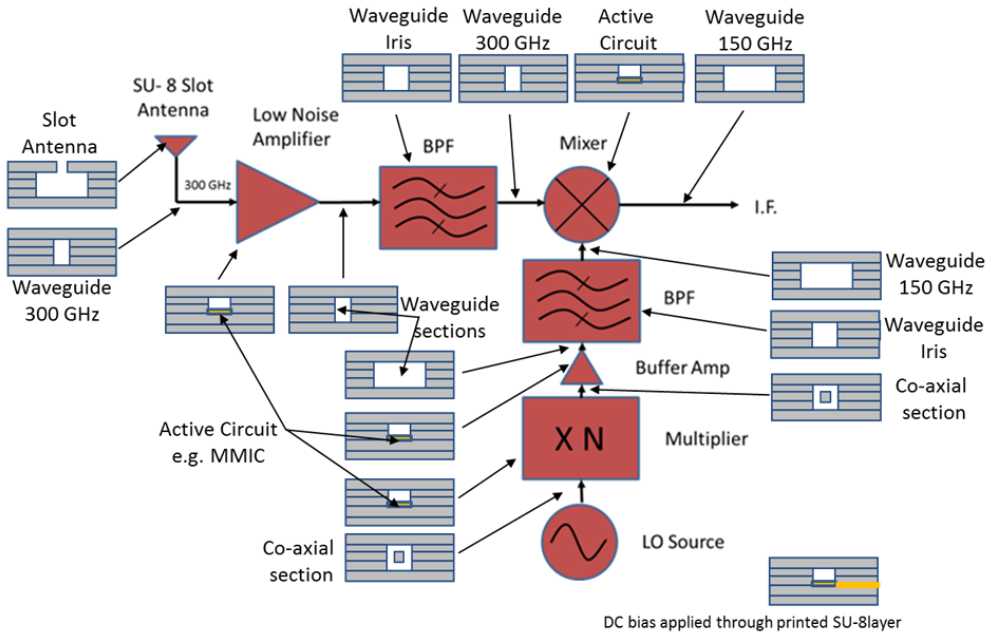

Figure 2.3 - Terahertz receiver system concept, constructed from layers of metal coated SU-8 polymer

way that has never been done before at terahertz frequencies . This layering technology is an alternative to metal machining for constructing sections of circuit such as waveguide connections, coaxial connections, cavity resonators for filters and cavities for the mounting of active circuit components such as frequency doubling diodes and buffer amplifier transistors. The layered structure can also be used to construct cavities and stubs for impedance matching sections where needed.

2.5 Conclusions

It has been shown that the terahertz region has potential for exploitation and that the technology to do so already exists, at a cost. Breakthroughs in low cost manufacture for high frequency, along with refinements in design techniques, are needed to assist in the conquering of this part of the spectrum. The terahertz region is an ideal arena for creative engineering and applications yet unthought-of, which will flourish as the terahertz barriers crumble.

Refererences

[1] International Telecommunications Union. I.T.U. http://www.itu.int/en/Pages/default.aspx

[2] C. Jastrow, K. M. **300 GHz transmission system.** Electronics Letters 2008. Volume 44, issue 3, pages 213-214.

[3] Radoslaw Piesiewicz, T. K.-O. **Short-Range Ultra-Broadband Terahertz Communications: Concepts and Perspectives**. IEEE Antennas and Propagation Magazine, 2007. Volume 49, pages 24-39.

[4] Dalu Guo, Weiwen Yuan, Xiguo Sun, Haidong Qiao, Xin Lv. **A terahertz High Speed Communication Research Based on TMIC at 340 GHz**. IEEE Asia-Pacific Microwave Conference, 2015. Volume 3, pages 1-3.

[5] Woon-Gi Yeo, N. K. **New Frontiers for Commercial Applications of Terahertz**. Proceedings of the IEEE National Aerospace and Electronics Conference, 2011. Pages 5-8.

[6] Shian U. Hwu, K. B. **Terahertz Wireless Systems for Space Applications**. IEEE conference paper: Sensors Applications Symposium, 2013. Pages 171 – 175.

[7] Ho-Jin Song, K. A. **Terahertz Wireless Communication Link at 300 GHz**. IEEE International Topical Meeting on Microwave Photonics, 2010. Pages 42-45.

[8] Shi-Wei Dong, Z. **Advances of Terahertz Research and Terahertz Satellite Communications.** International Conference on Electronics, Communications and Control, 2011. Pages 4122-4125.

[9] C. Jastrow, S. Priebe, B. Spitschan, J. Hartmann, M. Jacob, T. Kurner, T. Schrader and T. Kleine-Ostmann. **Wireless digital data transmission at 300 GHz**. Electronics Letters, April 2010. Volume 46, number 9, pages 661-663.

[10] Jae-Sung Rieh, S. J. **An Overview of Integrated THz Electronics for Communication Applications**. IEEE 54th International Midwest Symposium on Circuits and Systems, 2011. Pages 1-4.

[11] Oberdan Donadio, **G-band Waveguide to Microstrip Transition for MMIC Integration**. University of Glasgow School of Engineering. January, 2012.

[12] Maagt, Peter.Janet Charlton. **Terahertz Space Applications and Technology** IEEE, International Microwave Symposium Digest, 2005. Page 4.

[13] J. Stutzki, U. G. **Terahertz Receivers for Astronomy**. Joint 30th International Conference on Infrared and Millimeter Waves and 13th International Conference on Terahertz Electronics, 2005. Volume 2, pages 403-404.

[14] Goutam Chattopadhyay, Nuria Llombart, Choonsup Lee, Cecile Jung, Robert Lin, Ken B. Cooper, Theodore Reck, Jose Siles, Erich Schlecht, Alessandro Peralta, Bertrand Thomas, and Imran Mehdi. **Terahertz Array Receivers with Integrated Antennas**. IEEE International Workshop on Antenna Technology, 2012. Pages 319-322.

[15] Christopher K. Walker & Craig A. Kulesa. **Terahertz Astronomy from the Coldest Place on Earth**. Joint 30th International Conference on Infrared and Millimeter Waves and 13th International Conference on Terahertz Electronics, 2005. Volume 1, pages 3-4.

[16] Wild, W. **Terahertz heterodyne technology for astronomy and planetary science**. Joint 32nd International Conference on Infrared and Millimeter Waves and the 15th International Conference on Terahertz Electronics, 2007. Pages 323-325.

[17] J. Bianca Jackson, John Bowen, Gillian Walker, Julien Labaune, Gerard Mourou, Michel Menu, and Kaori Fukunaga, **A Survey of Terahertz Applications in Cultural Heritage Conservation Science**. IEEE Transactions on Terahertz Science and Technology, 2011. Volume 1, issue 1, pages 220-231.

[18] Woon-Gi Yeo, Niru K. Nahar, Robert Lee and John L. Volakis. **New Frontiers for Commercial Applications of Terahertz.** Proceedings of the IEEE National Aerospace and Electronics Conference, 2011. Pages: 5-8.

[19] Iwao Hosako, Naoki Oda, Norihiko Sekine, Kaori Fukunaga, and Yuichi Ogawa. **Real-time terahertz camera system; its technology and applications**. Conference Proceedings, 20th International Conference on Applied Electromagnetics and Communications, 2010. Pages 1-3.

[20] J. Cunningham, M.B. Byrne, C.D. Wood and L. Dazhang. **On-chip terahertz systems for spectroscopy and imaging**. Electronics Letters, 2010. Volume 46, issue 26, pages s34-s37.

[21] H. Yoneyama, M. Yamashita, S. Kasai, H. Ito and T. Ouchi. **Application of Terahertz Spectrum in the Detection of Harmful Food Additives**. Joint 32nd International Conference on Infrared and Millimeter Waves and the 15th International Conference on Terahertz Electronics, 2007. Pages 281-282.

[22] Tyler Bowman and Magda El-Shenawee. **Pulsed Terahertz Spectrometry of Excised Breast Cancer Tissue**. USNC-URSI Radio Science Meeting, 2013. Page 207.

[23] Kanis W.C. Kana, Wing-Sze Leeb, W. H. Cheungb, and Emma Pickwell-MacPhersona. **Imaging of Osteoarthritis using a Hand-held Terahertz Probe**. 34th International Conference on Infrared, Millimeter, and Terahertz Waves, 2009. Pages 1-2.

[24] K. Humphreys, J. P. Loughran, M. Gradziel, W. Lanigan, T. Ward, J.A. Murphy, C. O'Sullivan. **Medical applications of Terahertz Imaging: a Review of Current Technology and Potential Applications in Biomedical Engineering**. The 26th Annual International Conference of the IEEE Engineering in Medicine and Biology Society, 2004. Volume 1, pages 1302-1305.

[25] K. Kawase, H. Hoshina, A. Iwasaki, Y. Sasaki and T. Shibuya. **Mail screening applications of terahertz Radiation**. IEEE Terahertz Technology - Electronics Letters, December, 2010.

[26] Jianming Dai, Xiaoyu Guo, and X.-C. Zhanga. **Terahertz Air Photonics for Standoff Explosive Detection.** IEEE Conference on Technologies for Homeland Security, 2009. Pages 461-464.

[27] Iván Cámara Mayorga, A. S. **First In-Field Application of a Full Photonic Local Oscillator to Terahertz Astronomy**. IEEE Transactions on Terahertz Science and Technology, 2012. Volume 2, issue 4, pages 393-399.

[28] Ekaterina Laskin, Pascal Chevalier, Alain Chantre, Bernard Sautreuil, and Sorin P. Voinigescu. **165-GHz Transceiver in SiGe Technology**. IEEE Journal of Solid-State Circuits, 2008. Volume 43, issue 5, pages 1087-1100.

[29] S. Marsh, B. Alderman, D. Matheson and P. de Maagt. **Design of low-cost 183 GHz subharmonic mixers for commercial applications.** IET Circuits, Devices & Systems, 2007. Volume 1, issue 1, pages 1-6.

[30] Binbin Li, Bo Zhang, Yong Fan. **Design of a 440GHz Frequency Doubler based on planar Schottky diodes**. IEEE International Conference on Electron Devices and Solid-State Circuits, 2014. Pages 1-2.

[31] J. Schur,S. Biber, O. Cojocari, B. Mottet, L.-P. Schmidt, H.-L. Hartnagel. **600 GHz Heterodyne Mixer in Waveguide Technology using a GaAs Schottky Diode**. Joint 30th International Conference on Infrared and Millimeter Waves and 13th International Conference on Terahertz Electronics, 2005. Volume 2, pages 469-470.

[32] Chuying Mao, Chakravartula Shashank Nallani, Swaminathan Sankaran, Eunyoung Seok, and Kenneth K. O. **125-GHz Diode Frequency Doubler in 0.13-µm CMOS**. IEEE Journal of solid-state circuits, 2009. Volume 44, pages 1531-1538.

[33] Peng Chen, Xian-Jin Deng, Bin-Bin Cheng, Cheng Wang. **A 220GHz Frequency Doubler Based on Planar Schottky Diodes**. IEEE MTT-S International Microwave Workshop Series on Advanced Materials and Processes for RF and THz Applications, 2016. Pages 1-3.

[34] J. Treuttel, L. Gatilova, A. Maestrini, D. Moro-Melgar, F. Yang, F. Tamazouzt, T. Vacelet, Y. Jin, A. Cavanna, J. Matéos, A. Féret, C. Chaumont, and C. Goldstein. **A 520–620-GHz Schottky Receiver Front-End for Planetary Science and Remote Sensing With 1070 K–1500 K DSB Noise Temperature at Room Temperature**. IEEE transactions on terahertz science and technology, 2016. Volume 6, pages 148-155.

[35] M. Kim, B.H. Fujiwara, D.A. Humphrey, S.C. Martin, R.P. Smith, and P.H. Siegel. **A 600 GHz Planar Frequency Multiplier Feed On a Silicon Dielectric-Filled Parabola**. GaAs IC

Symposium. IEEE Gallium Arsenide Integrated Circuit Symposium. 19th Annual Technical Digest 1997. Pages 287-29.

[36] John Ward, Erich Schlecht, Goutam Chattopadhyay, Alain Maestrini1, John Gill, Frank Maiwald, Hamid Javadi, and Imran Mehdi. **Capability of THz sources based on Schottky diode frequency multiplier chains**. IEEE MTT-S International Microwave Symposium Digest, 2004. Volume 3, pages 1587-1590.

[37] Thomas W. Crowe. **Muliplier Technology for Terahertz Applications**. 33rd International Conference on Infrared, Millimeter and Terahertz Waves, 2008. Page 1.

[38] Eunyoung Seok, Dongha Shim, Chuying Mao, Ruonan Han, Swaminathan Sankaran, Changhua Cao, Wojciech Knap, and Kenneth K. O. **Progress and Challenges Towards Terahertz CMOS Integrated Circuits**. IEEE journal of solid-state circuits, 2010. Volume 45, pages 1554-1564.

[39] José V. Siles, and Jesús Grajal. **Physics-Based Design and Optimization of Schottky Diode Frequency Multipliers for Terahertz Applications**. IEEE Transactions on microwave theory and techniques, July 2010. Volume 58, issue 7, pages 1933-1942.

[40] Imran Mehdi , Jose V. Siles , Choonsup Lee, and Erich Schlecht. **THz Diode Technology: Status, Prospects, and Applications.** Proceedings of the IEEE, 2017. Volume PP, issue 99, pages 1-18.

[41] Alain Maestrini; Imran Mehdi; José V. Siles; John S. Ward; Robert Lin; Bertrand Thomas; Choonsup Lee; John Gill; Goutam Chattopadhyay; Erich Schlecht; John Pearson; Peter Siegel. **Design and Characterization of a Room Temperature All-Solid-State Electronic Source Tunable From 2.48 to 2.75 THz.** IEEE Transactions on Terahertz Science and Technology, 2012. Volume 2, issue 2, pages 177-185.

[42] B.T. Bulcha1, J.L. Hesler, V. Drakinskiy, J. Stake, N.S. Barker, **1.9-3.2 THz Schottky Based Harmonic Mixer Design and Characterization**. IEEE Microwave Conference (EuMC), 2015, pages 837-840.

[43] Hugh J.E. Gibson, Achim Walber, Bertrand Thomas**. Sub-millimeter wave balanced mixers and multipliers at the 5th harmonic**. International Symposium on Space Terahertz Technology, Moscow, 2014. Page 175.

[44] V. Drakinskiy; P. Sobis; H. Zhao; T. Bryllert; J. Stake. **Terahertz GaAs Schottky diode mixer and multiplier MIC's based on e-beam technology**. International Conference on Indium Phosphide and Related Materials, 2013. Pages 1-2.

[45] Tomasz Waliwander; Martin Fehilly; Emmet O'Brien**. An ultra-high efficiency high power Schottky varactor frequency doubler to 180–200 GHz**. Global Symposium on Millimeter Waves and ESA Workshop on Millimetre-Wave Technology and Applications, 2016. Pages 1-4.

[46] Byron Alderman, Manju Henry, Hoshiar Sanghera, Hui Wang; Simon Rea, Brian Ellison, Peter. de. Maagt. **Schottky diode technology at Rutherford Appleton Laboratory.** IEEE International Conference on Microwave Technology & Computational Electromagnetics, 2011. Pages 4-6

[47] Naser Alijabbari, Matthew F. Bauwens, Robert M. Weikle. **160 GHz Balanced Frequency Quadruplers Based on Quasi-Vertical Schottky Varactors Integrated on Micromachined Silicon.** IEEE Transactions on Terahertz Science and Tech, 2014. Vol 4, issue 6, pages 678-685

[48] K. Wu, D. Deslandes and Y. Cassivi. **The Substrate Integrated Circuits - A New Concept for High-Frequency Electronics and Optoelectronics.** 6th International Conf. on Telecoms in Modern Satellite, Cable and Broadcasting Service, 2003. Volume 1, pages P-III-P-X

[49] J. E. Rayas-Sanchez and V. Gutierrez-Ayala. **A General EM-Based Design Procedure for Single-Layer Substrate Integrated Waveguide Interconnects with Microstrip Transitions.** IEEE International Microwave Symposium, Atlanta, 2008. Pages 983-986.

[50] Xiao-Dong Deng, Yihu Li, Wen Wu, Yong-Zhong Xiong**. 340-GHz SIW Cavity-Backed Magnetic Rectangular Slot Loop Antennas and Arrays in Silicon Technology**. IEEE Transactions on Antennas and Propagation, 2015. Volume 63, issue 12, pages 5272-5279.

[51] Zhuang, J, Hong, W, Hao,Z. **Design and analysis of a terahertz bandpass filter**. International Wireless Symposium, Shenzen, China. 2015. Pages 1-4.

[52] Walker, C.K., Knoepfle, H, Capara, J**. Laser micromachining of silicon: a new technique for fabricating high quality terahertz waveguide components**. Proceedings of the 8th International symposium of Space Terahertz Technology, 1997. Pages 358-376.

[53] X Shang, P Penchev, C Guo. **W-band waveguide filters fabricated by laser micromaching and 3-D printing.** IEEE transactions in microwave theory and technology, 2016. Volume 64, issue 8, pages 2572-2580.

[54] C Guo, X Shang, M Lancaster**. A 3-D printed lightweight X-band waveguide filter based on spherical resonators**. IEEE Microwave wireless components letters, 2015. 25(7) pages 442-444.

[55] Mario D'Auria, William J. Otter, Jonathan Hazell, Brendan T. W. Gillatt, Callum Long-Collins, Nick M. Ridler, Stepan Lucyszyn. **3-D Printed Metal-Pipe Rectangular Waveguides**. IEEE Transactions on Components, Packaging and Manufacturing Technology, 2015. Volume 5, issue 9, pages 1339-1349.

Chapter 3

Microwave Bandpass Filters

3.1 Introduction

The microwave spectrum is a congested range of frequencies shared by a multitude of disciplines and applications. It is therefore essential to be able to screen out unwanted signals to select and contain the information of importance, and the technology to enable this are filters. Filters are in general constructed from resonating elements that are coupled together so that a desired range of frequencies is passed, excluded or both. It is therefore fundamental to general filter design theory that any element that resonates and couples energy to another circuit element, could be used to construct a filter. This chapter demonstrates this assumption and outlines how coupling matrix theory can be used to design filters using resonating elements. It also shows how resonators can be constructed using both microstrip and waveguide techniques and details some of the theory required to use both these media in the construction of filters.

This background is used later to investigate novel methods of filter construction at highly dimensionally demanding terahertz frequencies, and also forms the basis of constructing active circuits with integrated filters, hence eliminating the traditional requirement for matching circuits.

3.2 Microwave Resonators

A microwave resonator can be broadly defined as any structure that can contain an oscillating microwave field. A fundamental parameter of a resonant circuit is its *Q* or quality factor. The *Q* is

the ratio of energy stored in the circuit to the energy lost over time. This is summarised in the following equation [1]

$$Q = \omega \frac{average\ engergy\ stored}{energy\ lost\ per\ second} \tag{3.1}$$

We can therefore say that *Q* is a measure of loss in a resonant circuit, and a high loss circuit will have a low *Q*, and a low loss circuit will have a relatively high *Q*. The losses in the resonator are therefore important in understanding the value of *Q*, as is also the mechanism for energy storage in the resonator. The loss and energy stored differ depending on resonator type, and require a detailed analysis if they are to be understood fully. For example, in the case of a microstrip resonator the loss mechanisms are dominated by conductor, dielectric and radiation losses, each with an associated quality factor (Q_c, Q_d, and Q_r respectively). Once these are known, they can be combined to determine the total unloaded circuit quality factor Q_u, as shown in: [2]

$$\frac{1}{Q_u} = \frac{1}{Q_c} + \frac{1}{Q_d} + \frac{1}{Q_r} \tag{3.2}$$

The next step is to examine the case where the resonator is connected to the external source and load and an external coupling, Q_e is applied. This coupling can bring in energy, as well as remove energy, and can be viewed as a loss mechanism in a similar way as explained above. So, we can combine this coupling to determine a loaded *Q* factor, Q_l which is given in:

$$\frac{1}{Q_l} = \frac{1}{Q_u} + \frac{1}{Q_e} \tag{3.3}$$

3.3 Filter Analysis

A microwave frequency filter can be described as a two port network with the characteristics of passing or supressing particular frequency bands. Such a network is represented in Figure 3.1 and here it is introduced with analysis using scattering, or S parameters.

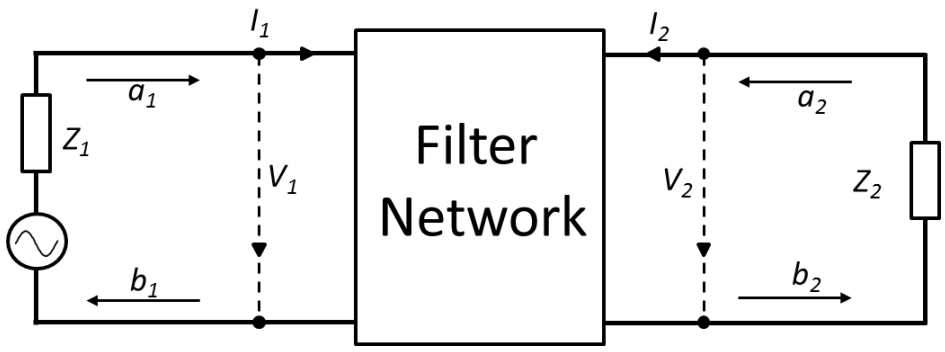

Figure 3.1 – Network Analysis of a filter

S parameters are useful for the analysis of microwave circuits, as voltages and currents are difficult to measure at high frequencies, but transmitted and reflected waves are much easier to determine instead. It is important to be able to reverse engineer these waveforms back into voltages and currents for the analysis of the circuits used in this thesis, therefore a brief summary of S parameters are given here to allow this.

In Figure 3.1, V_1 and V_2 are the voltage scalar quantities, I_1 and I_2 are the current scalars, and Z_1 and Z_2 are the impedances of the input and output terminations (usually 50 Ω). The

incident waves are represented by a_1 and a_2 and the reflected waves by b_1 and b_2, with the relationships of the parameters described by the following equations where n = 1 and 2.

$$V_n = \sqrt{Z_n}\,(a_n + b_n) \tag{3.4}$$

$$I_n = \frac{1}{\sqrt{Z_n}}(a_n - b_n) \tag{3.5}$$

$$a_n = \frac{1}{2}\left(\frac{V_n}{\sqrt{Z_n}} + \sqrt{Z_n} I_n\right) \tag{3.6}$$

$$b_n = \frac{1}{2}\left(\frac{V_n}{\sqrt{Z_n}} - \sqrt{Z_n} I_n\right) \tag{3.7}$$

The S parameters are now defined in terms of the incident and reflected waves thus

$$S_{11} = \frac{b_1}{a_1} \qquad (a_2 = 0) \tag{3.8}$$

$$S_{12} = \frac{b_1}{a_2} \qquad (a_1 = 0) \tag{3.9}$$

$$S_{21} = \frac{b_2}{a_1} \qquad (a_2 = 0) \tag{3.10}$$

$$S_{22} = \frac{b_2}{a_2} \qquad (a_1 = 0) \tag{3.11}$$

Where $a_n = 0$ requires a perfect impedance match with no reflection from the termination.

We can also define the power at either port using

$$P_n = \frac{1}{2} Re(V_n I_n^*) \tag{3.12}$$

Or

$$P_n = \frac{1}{2} (a_n a_n^* - b_n b_n^*) \tag{3.13}$$

Where * denotes a conjugate quantity.

3.4.1 Coupling Matrix Method for Bandpass Filter Design

The coupling matrix is used to represent physical elements in a circuit and is a powerful tool for filter design [3]. This is because filters are made up of resonating elements with energy being coupled between these elements, which the matrix and the developed mathematical techniques [4,5,6] simplifies and summarises. Here we introduce the method of using coupling matrix to

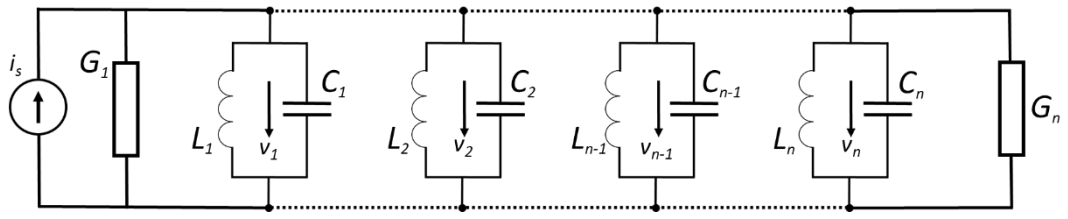

Figure 3.2 – Resonator Configuration of *n* capacitive coupled resonators

design coupled resonator bandpass filters. A useful outcome of the coupling matrix method is that it shows that it is possible to construct a microwave bandpass filter by arranging a series of coupled resonators, such as those represented in Figure 3.2. The coupling can be described either in the case of mutual inductance (for magnetic coupling), or in the case of Figure 3.2, mutual capacitance (for capacitive coupling), where *C* and *L* are the lumped capacitance and inductance values, and *v* is the node voltage. Using Kirchhoff's current law with Figure 3.2, for an *n* coupled resonator, the node equations can be derived as [3]

$$\left(G_1 + j\omega C_1 + \frac{1}{j\omega L_1}\right) v_1 - j\omega C_{12} v_2 \ldots - j\omega C_{1n} v_n = i_s$$

$$-j\omega C_{21} v_1 + \left(j\omega C_2 + \tfrac{1}{j\omega L_2}\right) v_2 \ldots - j\omega C_{2n} v_n = 0 \qquad 3.14$$

$$-j\omega C_{n1} v_1 - j\omega C_{n2} v_2 \ldots + \left(G_n + j\omega C_n + \frac{1}{j\omega L_n}\right) v_n = 0$$

Where *G* represents conductance, i_s is the source current. Equation 3.14 can also be expressed in matrix form such as

$$\begin{bmatrix} \left(G_1 + j\omega C_1 + \frac{1}{j\omega L_1}\right) & -j\omega C_{12} & \cdots & -j\omega C_{1n} \\ -j\omega C_{21} v_1 & j\omega C_2 + \frac{1}{j\omega L_2} & \cdots & -j\omega C_{2n} \\ \vdots & \vdots & \vdots & \vdots \\ -j\omega C_{n1} & -j\omega C_{n2} v_2 & \cdots & G_n + j\omega C_n + \frac{1}{j\omega L_n} \end{bmatrix} \begin{bmatrix} v_1 \\ v_2 \\ \vdots \\ v_n \end{bmatrix} = \begin{bmatrix} i_s \\ 0 \\ \vdots \\ 0 \end{bmatrix} \qquad 3.15$$

Or $[Y] \cdot [v] = [i]$, where $[Y]$ is an *n* by *n* admittance matrix.

To simplify the problem, the filter is assumed to be synchronously tuned, with all elements resonating at the same frequency $\omega_0 = \frac{1}{\sqrt{LC}}$, where $L=L_1=L_2=\ldots=L_n$, $C=C_1=C_2=\ldots=C_n$. The admittance matrix in 3.15 can be expressed by

$$[Y] = \omega_0 C \cdot FBW \cdot [\bar{Y}] \tag{3.16}$$

Where $FBW = \frac{\Delta\omega}{\omega_0}$ is the fractional bandwidth and the normalised admittance matrix is denoted by $[\bar{Y}]$. For a synchronously tuned filter, $[\bar{Y}]$ can be given by [3]

$$[\bar{Y}] = \begin{bmatrix} \frac{G_1}{\omega_0 C \cdot FBW} + p & -j\frac{\omega}{\omega_0}\frac{C_{12}}{C}\cdot\frac{1}{FBW} & \cdots & -j\frac{\omega}{\omega_0}\frac{C_{1n}}{C}\cdot\frac{1}{FBW} \\ -j\frac{\omega}{\omega_0}\frac{C_{21}}{C}\cdot\frac{1}{FBW} & p & \cdots & -j\frac{\omega}{\omega_0}\frac{C_{2n}}{C}\cdot\frac{1}{FBW} \\ \vdots & \vdots & \vdots & \vdots \\ -j\frac{\omega}{\omega_0}\frac{C_{n1}}{C}\cdot\frac{1}{FBW} & -j\frac{\omega}{\omega_0}\frac{C_{n2}}{C}\cdot\frac{1}{FBW} & \cdots & \frac{G_n}{\omega_0 C \cdot FBW} + p \end{bmatrix} \tag{3.17}$$

Where p is the frequency variable given as

$$p = j * \frac{1}{FBW}\left(\frac{\omega}{\omega_0} - \frac{\omega_0}{\omega}\right) \tag{3.18}$$

It can be shown that [3]

$$\frac{G_i}{\omega_0 C} = \frac{1}{Q_{ei}} \qquad \text{for } i=1,n \tag{3.19}$$

Where Q_e is the external quality factor. The coupling coefficient is also defined as [3]

$$M_{ij} = \frac{C_{ij}}{C} \tag{3.20}$$

And that if $\frac{\omega}{\omega_0} \approx 1$ can be assumed for a narrow band approximation, then equation 3.17 can be simplified to

$$[\bar{Y}] = \begin{bmatrix} \frac{1}{q_{e1}} + p & -jm_{12} & \cdots & -jm_{1n} \\ -jm_{21} & p & \cdots & -jm_{2n} \\ \vdots & \vdots & \vdots & \vdots \\ -jm_{n1} & -jm_{n2} & \cdots & \frac{1}{q_{en}} + p \end{bmatrix} \quad 3.21$$

Where q_{ei} is the scaled external quality defined by

$$q_{ei} = Q_{ei} \cdot FBW \qquad \text{for } i=1,n \quad 3.22$$

and m_{ij} is the normalised coupling coefficient defined by

$$m_{ij} = \frac{M_{ij}}{FBW} \quad 3.23$$

As stated in [3], in case of asynchronously tuned filters, self-coupling (m_{ii}) can be added into the entries on the main diagonal of the normalised admittance matrix, as shown below.

$$[\bar{Y}] = \begin{bmatrix} \frac{1}{q_{e1}} + p - jm_{11} & -jm_{12} & \cdots & -jm_{1n} \\ -jm_{21} & p - jm_{22} & \cdots & -jm_{2n} \\ \vdots & \vdots & \vdots & \vdots \\ -jm_{n1} & -jm_{n2} & \cdots & \frac{1}{q_{en}} + p - jm_{nn} \end{bmatrix} \quad 3.24$$

As discussed in Section 3.3, the filter can also be represented using the network model. The S-parameters of the filter equivalent circuit network can be expressed as [3]

$$S_{11} = \pm\left(1 - \frac{2}{q_{e1}}[\bar{Y}]_{11}^{-1}\right) \quad 3.25$$

$$S_{21} = \frac{2}{\sqrt{q_{e1}q_{en}}}[\bar{Y}]_{n1}^{-1} \quad 3.26$$

Filters coupled by mutual inductances can be analysed in a similar way [3]. The S-parameters of the inductance coupled filter network can be expressed as

$$S_{11} = \pm\left(1 - \frac{2}{q_{e1}}[\bar{Z}]_{11}^{-1}\right) \tag{3.27}$$

and

$$S_{21} = \frac{2}{\sqrt{q_{e1}q_{en}}}[\bar{Z}]_{n1}^{-1} \tag{3.28}$$

Where $[\bar{Z}]$ is the normalised impedance matrix, given by [3]

$$[\bar{Z}] = \begin{bmatrix} \frac{1}{q_{e1}} + p - jm_{11} & -jm_{12} & \cdots & -jm_{1n} \\ -jm_{21} & p - jm_{22} & \cdots & -jm_{2n} \\ \vdots & \vdots & \vdots & \vdots \\ -jm_{n1} & -jm_{n2} & \cdots & \frac{1}{q_{en}} + p - jm_{nn} \end{bmatrix} \tag{3.29}$$

It can be found that $[\bar{Z}]$ and $[\bar{Y}]$ has the same expression. Therefore a general matrix $[A]$ (see below) can be introduced to deal with filters based on different types of couplings (i.e. magnetic, electric, or a combination of both).

$$[A] = [qm] + p[U] - j[m] \tag{3.30}$$

or

$$[A]=\begin{bmatrix} 1/q_{e1} & \dots & 0 & 0 \\ \vdots & \vdots & \vdots & \vdots \\ 0 & \dots & 0 & 0 \\ 0 & \dots & 0 & 1/q_{en} \end{bmatrix}+P\begin{bmatrix} 1 & \dots & 0 & 0 \\ \vdots & \vdots & \vdots & \vdots \\ 0 & \dots & 1 & 0 \\ 0 & \cdots & 0 & 1 \end{bmatrix}-j\begin{bmatrix} m_{11} & \dots & m_{1(n-1)} & m_{1n} \\ \vdots & \vdots & \vdots & \vdots \\ m_{(n-1)1} & \cdots & m_{(n-1)(n-1)} & m_{(n-1)n} \\ m_{n1} & \cdots & m_{n(n-1)} & m_{nn} \end{bmatrix}$$

3.31

Where [*U*] is the $n \times n$ unit matrix, [*qm*] is an $n \times n$ matrix with all entries zero, except for $q_{11}=1/q_{e1}$, $q_{nn}=1/q_{en}$, and [*m*] is the coupling matrix.

S-parameters can be calculated from the general coupling matrix as follows [3]

$$S_{11} = \pm\left(1 - \frac{2}{q_{e1}}[A]^{-1}_{11}\right) \quad 3.32$$

$$S_{21} = \frac{2}{\sqrt{q_{e1}q_{en}}}[A]^{-1}_{n1} \quad 3.33$$

Now for a Chebyshev filter we can calculate the external quality factor Q_e and the internal couplings *M* using the '*g*' values determined in equations 3.34 to 3.46.

$$Q_{e1} = \frac{g0*g1}{FBW} \quad 3.34$$

$$Q_{en} = \frac{gn*gn+1}{FBW} \quad 3.35$$

$$M_{i,i+1} = \frac{1}{\sqrt{g_i g_{i+1}}}FBW \quad for\ i = 1, \dots, n-1 \quad 3.36$$

$$M_{i+1,i} = \frac{1}{\sqrt{g_i g_{i+1}}} FBW \quad 3.37$$

Where the *g* values are representative of the low pass prototype filter response, and in the case of a Chebyshev response are given by

$$g_0 = 1 \quad 3.38$$

$$g_1 = \frac{2a_1}{sinh\left(\frac{\beta}{2n}\right)} \quad 3.39$$

$$g_i = \frac{4a_{i-1}a_i}{b_{i-1}g_{i-1}} \quad 3.40$$

$$g_{n+1} = \begin{cases} coth^2\left(\frac{\beta}{4}\right) & n\ even \\ 1 & n\ odd \end{cases} \quad 3.41 \text{ and } 3.42$$

Where

$$\beta = ln\left(\frac{\sqrt{1+\varepsilon}+1}{\sqrt{1+\varepsilon}-1}\right) \quad 3.43$$

$$a_i = sin\left(\frac{(2i-1)\pi}{2j}\right) \quad 3.44$$

$$b_i = sinh^2\left(\frac{\beta}{2j}\right) + sin^2\left(\frac{i\pi}{j}\right)^2 \quad 3.45$$

Where ε is the ripple specification, and is related to the maximum desired S_{11} in the following way.

$$\varepsilon = 10^{\frac{S_{11max}}{10}} \qquad 3.46$$

3.4.2 Determining the Couplings

It can be seen from the above sections, that as long as the resonators are synchronously tuned, all that is required is to construct a filter are specific couplings q and k between the external circuit and the internal resonators. These coupling values can be determined by calculation using the above equations. The minimum specifications required to for a filter design are:

1. A centre frequency, ω_0.
2. The filter bandwidth, $\Delta\omega$.
3. The desired reflection, S_{11max}.
4. The number of poles, n.

An example output of the computation is shown in Figure 3.3. This is for a specification of a 9 GHz centre frequency, 0.5 GHz bandwidth, 3 pole filter with a S_{11} of -20dB. The external q_e values are calculated at 15.39 and the internal k values are 0.057.

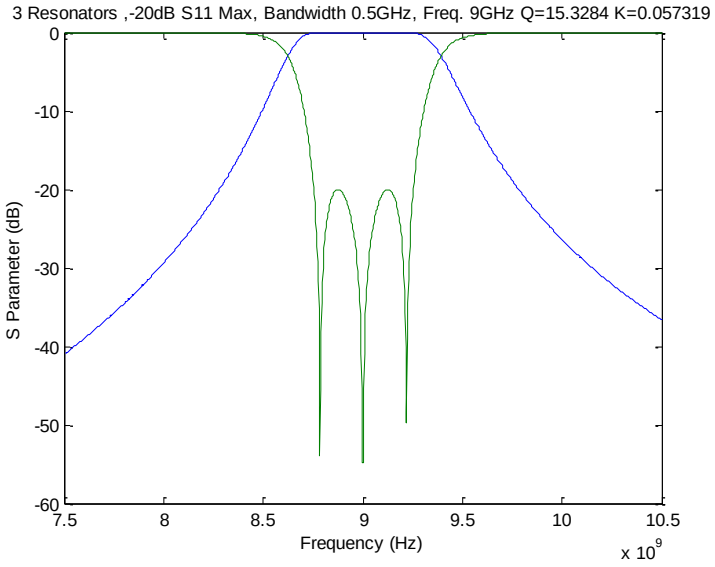

Figure 3.3 - Computed synthesis output

With this computed information, the next step is to realise the solution in a real circuit. The coupling q represents loss and energy transfer in and out of the circuit, and k represents the energy transfer between the resonators and the next step is to implement both these in a practical circuit. The coupling method of a circuit depends on its physical construction, for example a microstrip coupled line circuit couples across a gap between microstrip lines, whereas in a waveguide cavity resonator circuit, the couplings are via gaps / irises between resonators. The quality factor and the coupling can be varied by means dependant on the physical construction. Again in our two examples the external quality factor in a microstrip coupled line is affected by the physical distance between the first resonator and the feed line. In a waveguide cavity resonator circuit, the aperture size of the iris will vary the external quality factor.

3.4.3 Determining the external couplings

The schematic to determine the external coupling is shown in Figure 3.4.

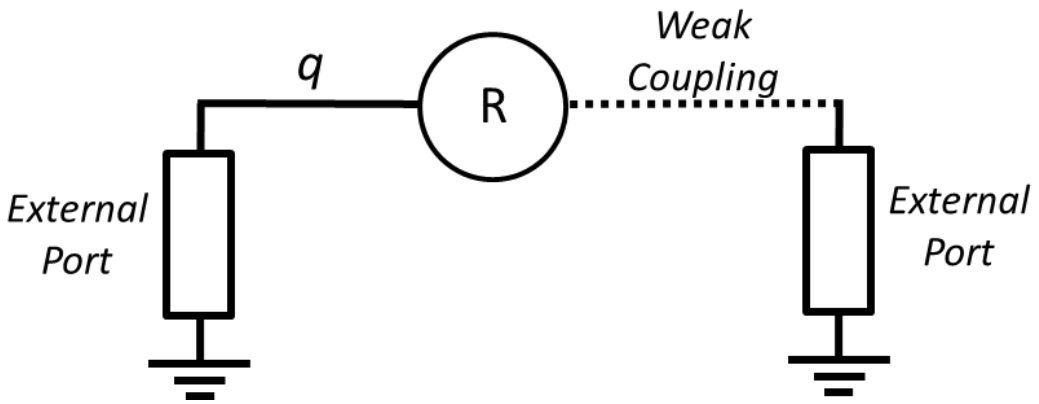

Figure 3.4 – Measuring the external coupling

Figure 3.4 shows the resonator R connected in a network analysis system set up to record S_{21}. This configuration can be set up in a simulation system such as Agilent's ADS [7] or CST [8]. The resultant measurement should be similar to that in Figure 3.5 and a quality factor measurement can be taken using:

$$q = \frac{f_{peak}}{\Delta f_{3dB}} \qquad 3.47$$

Where f_{peak} is the frequency at the maximum S_{21} value and Δf_{3dB} is the bandwidth of the curve measured at the point 3dB from f_{peak}.

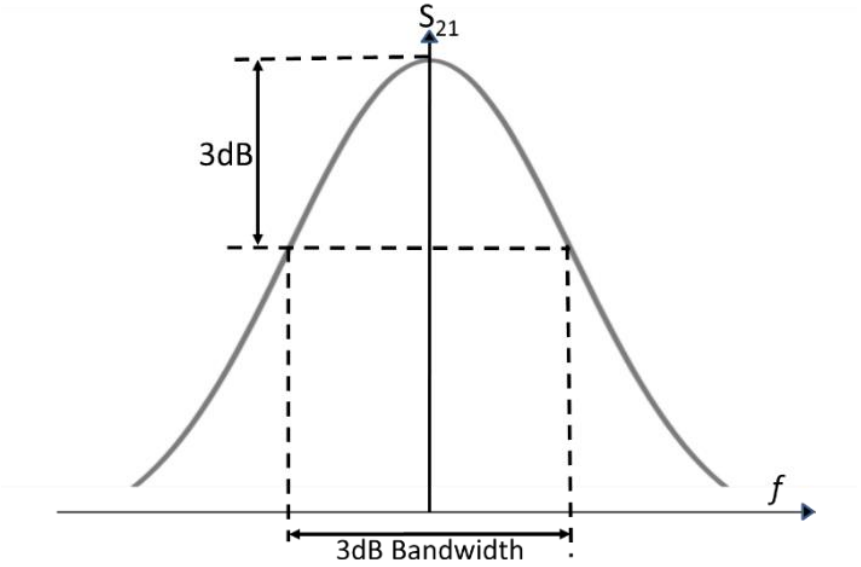

Figure 3.5 - Typical q curve

With one side of the resonator coupled weak enough so the q measurement is no longer affected (adjusting the external coupling at the output of the circuit to a very weak value), the quality factor can now be measured for the circuit, dominated as required by the input gap quality factor being profiled. It is useful to profile this quality factor to produce a plot of q couplings versus physical parameter change (e.g. track gap in microstrip or iris aperture in waveguide), as in the example graph in Figure 3.6. This will allow the required q to be selected and also helps to ensure no spurious couplings are affecting the circuit as the physical parameter is swept.

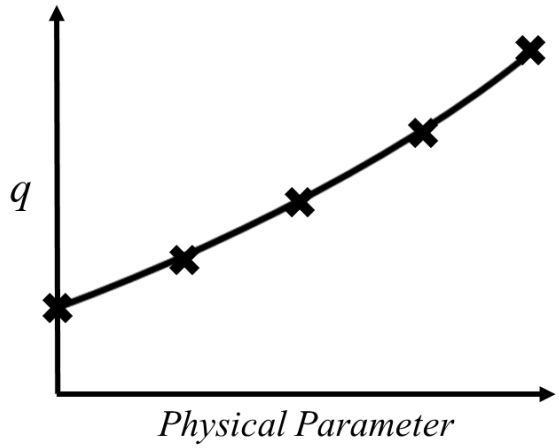

Figure 3.6 - Range of external couplings measured by varying the physical parameter

3.4.4. Determining the internal couplings

Next it is required to profile the internal couplings *k*. Figure 3.7 shows a network analysis setup to record S_{21} again, with the internal coupling between two resonator set by the physical parameter *k*.

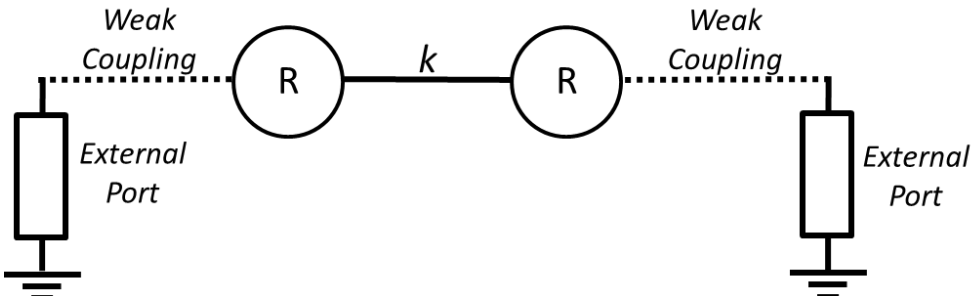

Figure 3.7 - Measuring the internal couplings

A two peak plot similar to that in Figure 3.8 should be obtained. Note it is not essential to reduce the external coupling so that it doesn't influence the circuit this time, but it can be set to give the clearest peaks to allow a definite measurement of the frequency points f_1 and f_2.

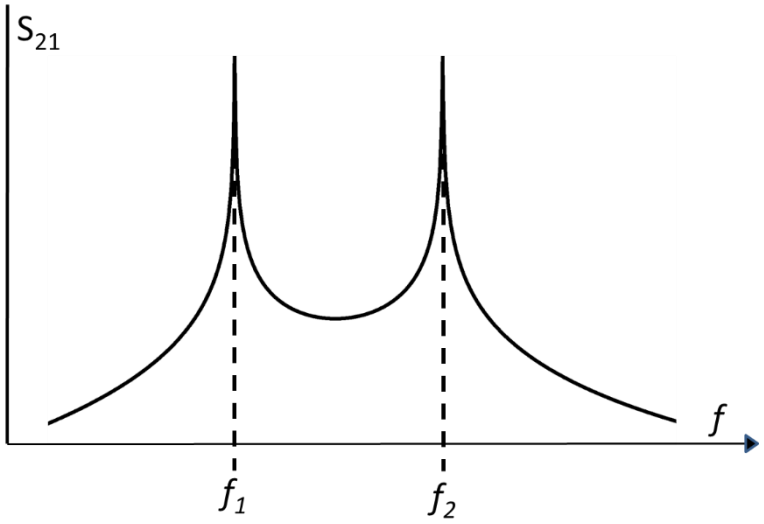

Figure 3.8 - Two peak plot of internal couplings

With f_1 and f_2 measured, the internal coupling k can be calculated using equation 3.48.

$$k = \frac{f_2^2 - f_1^2}{f_2^2 + f_1^2} \qquad 3.48$$

Once again, it is useful to sweep the physical parameter over a range of values to obtain a plot similar to Figure 3.9.

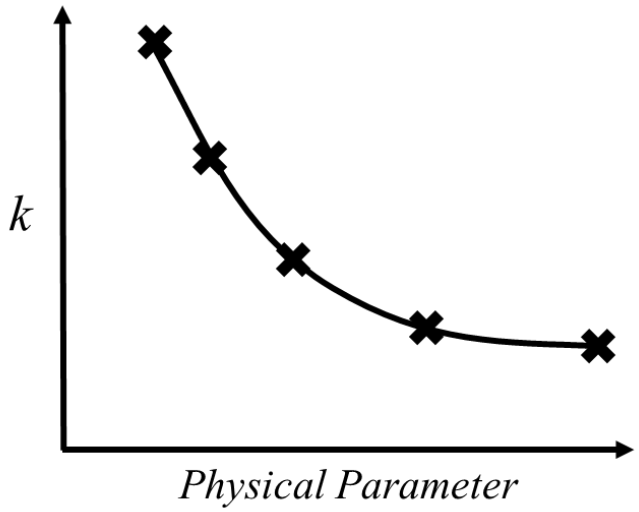

Figure 3.9 - Range of internal couplings measured by varying the physical parameter

Now that the internal and external couplings are found (Figure 3.6 and Figure 3.9), and a calculation has been made to determine the required *q* and *k* couplings for the specified filter parameters (Figure 3.3), the physical parameters can be read from the *q* and *k* curves in and entered into the simulated model of the whole filter.

We now have a method of determining the physical internal and external couplings for our specified filter solution, and the next step is to design a physical circuit to apply the above theory and design the filter. One such circuit type that we can use is microstrip, as it is possible to construct and model the resonators using simple lengths of track as detailed in the next section.

3.5 Microstrip Fundamentals

Microstrip is a useful medium for the construction of circuits. Not only is it fabricated easily by printed circuit technology inexpensively implemented in small laboratories, but there is also a wealth of work detailing the application of microstrip structures for microwave circuits. For example, microstrip tracks and shapes can be used for transmission lines, resonators, matching and short circuit stubs, capacitors, inductors, and therefore they can also form more advanced structures such as antenna, filters, and couplers. Active and passive components are easily integrated onto a microstrip circuit, generally by surface mount techniques or sometimes through a plated hole. Other consideration for circuit fabrication included co-planar waveguide, grounded coplanar waveguide, slotline, finline and stripline.

Coplanar waveguide has a lot of advantages such as good suitability for high frequency applications, good isolation due to the proximity of the ground, easy fabrication due to being able

to use thicker substrates and lower inductance from not having to use vias. However, coplanar and grounded coplanar circuits lack simulation tools for sub circuits and component equivalents, and it also has the potential requirement for circuit ground straps due to the appearance of additional transmission modes. It also has an overall larger circuit size.

Slotline is an easily fabricated method of circuit construction, but its lossy characteristics, difficulty in mounting components and lack of simulation tools means it is not suitable either.

Finline on the other hand has very low loss due to having no radiation and has broadband characteristics compared to the other methods, however it is complex to manufacture and is expensive and again has difficulty in mounting components.

Stripline is non dispersive, but hard to fabricate, and while there are simulation tools available, they are still not as comprehensive as those for microstrip, and again has difficulty in mounting components due to its enclosed structure.

Considering all the above advantages and disadvantages, microstrip has been chosen for its familiarity of use and hence easier comparison with common designs, easier manufacturability and low cost of fabrication. Microstrip is considered the best method to produce a prototype circuit to clearly demonstrate the principles this thesis is concerned with.

One of the drawbacks of microstrip is its upper frequency limit, which is largely determined by the thickness of the substrate. The calculation of the upper frequency limit is not straightforward due to many factors coming into play such as high order transmission modes, larger losses and the increase in influence of discontinuities as well as fabrication constraints. The board thickness at which significant coupling occurs between the main mode of transmission

(quasi-TEM) and the lowest order surface wave mode can provide an estimate of the upper frequency and is given by: [9]

$$h = \frac{150\times10^{12}}{\pi f_c}\sqrt{\frac{2}{\varepsilon_r - 1}}\,tan^{-1}\,\varepsilon_r \qquad 3.49$$

Where f_c is the cut-off frequency, h is the dielectric thickness and ε_r is the relative permittivity of the dielectric and this equation is plotted in Figure 3.10.

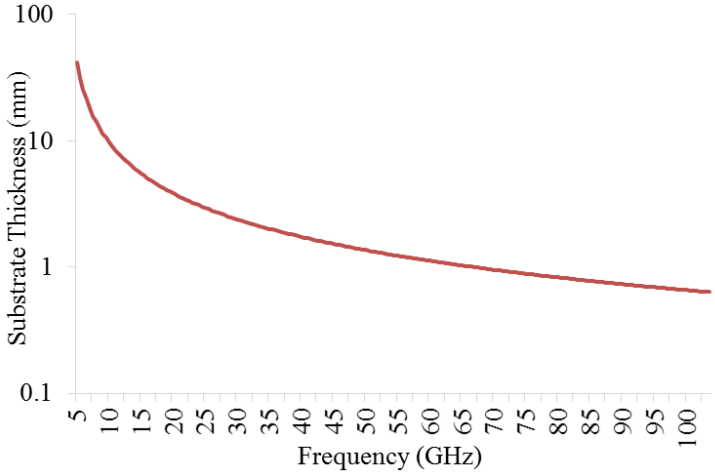

Figure 3.10 – Maximum useable frequency estimations determined by substrate thickness

We can see that a typical 1 mm thick microstrip substrate should be useable for frequencies approaching the 100 GHz range, however it is necessary to consider radiation losses if using high frequencies with microstrip.

Radiation losses at higher frequencies soon exceed those due to the conductor and dielectric [9], but these can be compensated for by using an even thinner substrate.

Another limitation to the highest useable frequency comes when we consider the effect of radiation due to discontinuities in the resonating tracks we use. These discontinuities can be due to common design structures such as bends, steps and open ends. An estimation to where the

effect of this radiation can become significant can be made using the equation for the approximate radiation Q factor Q_r for a λ /2 microstrip resonator [9]

$$Q_r = \frac{3\epsilon_r Z_0 \lambda_0^2}{32\eta h^2} \quad 3.50$$

Where $\eta = 120\Omega$, ϵ_r is the substrates dielectric constant, Z_0 is the resonators characteristic impedance (generally 50 Ω), λ is the wavelength and h is the substrate height in mm. Use of this information can force the user to opt for very thin substrates, however extra losses, a requirement for thinner tracks and gaps and practical implications of fragile and expensive materials will mean a compromise has to be made.

With careful choice of substrate material and thickness, microstrip is a useful media for proving some of the techniques in this thesis. Even though we will only be using microstrip at sub terahertz frequencies, we can later apply the knowledge and techniques to other resonating structures such as metal waveguide and SU-8 waveguide, which can operate at much higher frequencies. To use microstrip structures for the purpose of developing the ideas in this thesis, it is useful to define the microstrip structure and some of its important characteristics. We can then use it for our circuit, transmission lines and resonators.

Figure 3.11 shows the structure of a typical microstrip board with a conducting strip of thickness *t*, length *l* and width *w*. This sits on top of a dielectric substrate with a relative dielectric

constant ε_r and a thickness h. Beneath this is a conducting ground plane, typically of the same thickness as the conducting microstrip, t.

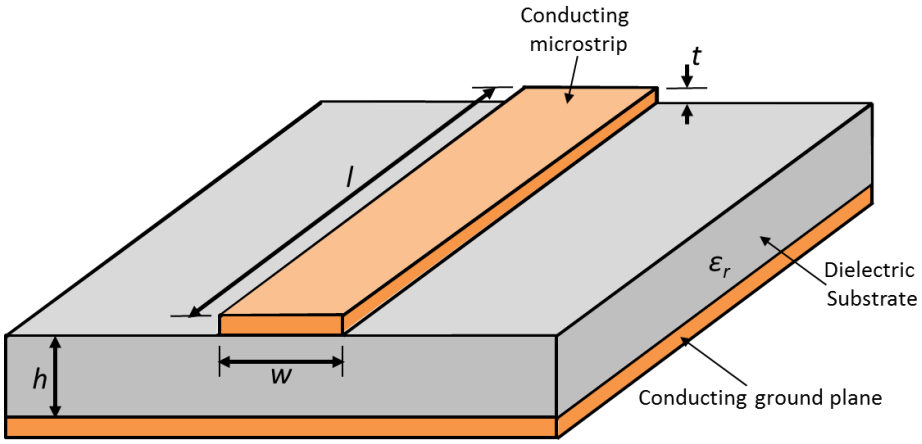

Figure 3.11 – Microstrip structure

We can use the parameters in Figure 3.11 to approximately calculate the characteristic impedance of a length of microstrip track using: [1]

$$Z_o = \frac{60}{\sqrt{\varepsilon_e}} ln\left(\frac{8h}{W} + \frac{W}{4h}\right) \qquad \text{where} \quad \frac{W}{h} \leq 1 \qquad 3.51$$

Or

$$Z_o = \frac{120\pi}{\sqrt{\varepsilon_e}} \times \frac{1}{\left(\frac{W}{h}+1.393+ln\left(\frac{W}{h}+1.414\right)\right)} \qquad \text{where} \frac{W}{h} \geq 1 \qquad 3.52$$

We will see in future chapters that equation 3.52 is the case for all our designs, as we always use track widths much wider than the dielectric thickness.

ε_e is the effective dielectric constant, and is given by [1].

$$\varepsilon_e = \frac{\varepsilon_r+1}{2} + \frac{\varepsilon_r-1}{2} \frac{1}{\sqrt{1+12h/W}} \qquad 3.53$$

The effective dielectric constant calculation is required as the electromagnetic field is not only in the dielectric, but also in the air gap above, as indicated Figure 3.12.

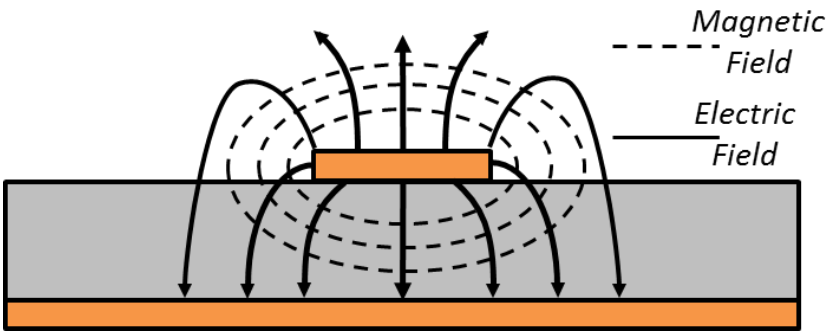

Figure 3.12 – Microstrip track showing field patterns around conductor

The situation we are interested in is the case where two microstrip resonators interact; the coupled line, as shown in Figure 3.13. This depicts the situation where both conductors are symmetrical and with equal line impedance. The coupled microstrip line occurs where two transmission lines are close enough for the electromagnetic field lines (shown in Figure 3.12), are able to interact with another transmission line. The analysis of this interaction concerns both the case where the currents in the lines are equal in amplitude and direction (even mode), and the case where the currents are equal in amplitude but in opposite direction (odd mode).

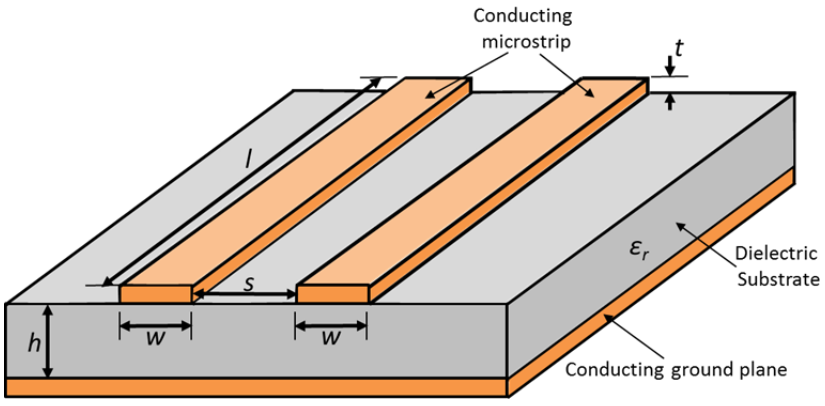

Figure 3.13 – Microstrip Coupled line

In the case of the even mode, no current flows between the conductors, but for the odd mode a voltage null or virtual ground exists between the conductors. From each of these situations, a different characteristic impedance can be calculated which will co-exist and form the basis of computational analysis in a circuit simulator such as Advanced Design System [7]. The strength of the coupling between the conductors can be varied by simply adjusting the gap size *s*. A larger gap results in a weaker coupling, and smaller gap gives a stronger coupling, and the *Q* can be selected as desired, by selecting a suitable gap.

It is now possible to use this basic theory to construct a model to use microstrip transmission lines in coupled resonator circuits, and this is done in chapter 5.

3.6 Rectangular Waveguide Fundamentals

While microstrip is often the medium of choice for microwave circuits due to its compact size and ease of integration, rectangular waveguide still has some advantages over microstrip, especially in high power and high frequency applications. Limited by physical bulk at low frequencies, and machining constraints at high frequencies, commercially available waveguides tend to come in the range from 1 GHz to a couple of hundred GHz, however we have shown in chapter 4 and [10] that with SU-8 manufacturing techniques, higher frequencies can be achieved beyond the range of microstrip and even commercial waveguide. In this section we will outline some of the fundamental waveguide theory, to allow us to use waveguide technologies for the purpose of illustrating the ideas in this thesis.

3.6.1 Propagation Modes

The theory of waveguides is well covered in text books, for example [1], and we shall repeat some of the basic theory here to allow an understanding for the ideas in this thesis. The

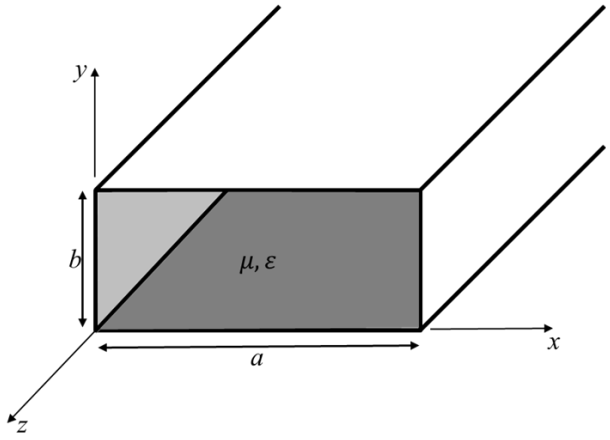

Figure 3.14 – Rectangular waveguide dimensions

rectangular waveguide is shown in Figure 3.14, with the height and width dimensions conventionally defined as *a* and *b* respectively.

The material in the centre of the waveguide is this thesis assumed to be vacuum with the properties of permittivity ε and permeability μ.

The waveguide can propagate transverse magnetic (TM), and transverse electric waves (TE) inside its hollow interior, but it cannot propagate transverse electromagnetic waves (TEM) [1] because of the presence of only a single conductor; the waveguide. There is identical cut-off frequency f_c for each of the TM_{mn} and TE_{mn} modes, given by:

$$f_{cmn} = \frac{1}{2\pi\sqrt{\mu\epsilon}}\sqrt{\left(\frac{m\pi}{a}\right)^2 + \left(\frac{n\pi}{b}\right)^2} \qquad 3.54$$

For the waveguides in this thesis we assume the *a* dimension is greater than *b*. It can be shown [1] that when *a* is twice *b*, that TE_{10} is the dominant mode and is given by:

$$f_{c10} = \frac{1}{2a\sqrt{\mu\epsilon}} \tag{3.55}$$

TE_{10} is the dominant mode as it has the lowest cut off frequency (f_{c10}), with the next highest cut off frequency being the TE_{20} mode (f_{c20}). If the waveguide is chosen to cover the frequency band between the cut-off of both these modes then only the TE_{10} will propagate in the waveguide and the bandwidth will be given by f_{c20}-f_{c10} = f_{c10}.

3.6.2 Waveguide resonators

A resonator can be constructed from waveguide by forming a cavity such as that shown in Figure 3.15. Such a structure is able to meet our criteria for a resonator in that it is able to store energy in both oscillating electric and magnetic fields. It can be shown [1] that to set the desired resonant centre frequency the dimension *c* should be an integer multiple of half of its wavelength.

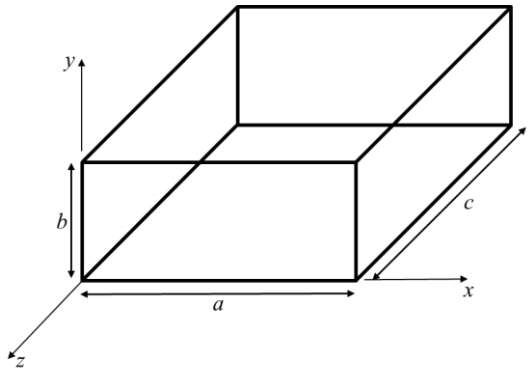

Figure 3.15 - Waveguide cavity

A sealed waveguide cavity is of no use however unless we can couple the energy into and out of it, and that is normally done via an aperture, as shown in Figure 3.16.

Figure 3.16 shows two waveguide cavity resonators of standard dimension *a* x *b*, and length half a wavelength at the resonant frequency. Separating the cavities is an iris block made of conducting material, usually the same material as the waveguide walls. The iris block is of thickness *t* and has a gap at the top *s*, which determines the strength of coupling between the cavities. Also indicated is the situation of weak input and output coupling using the small aperture set by the dimension *r*.

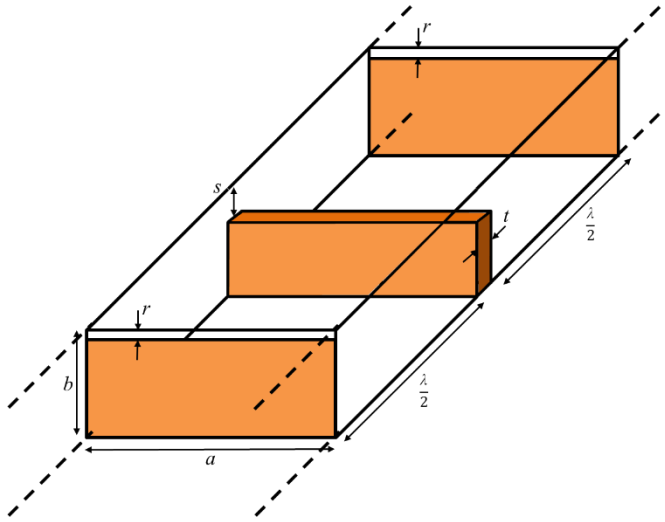

Figure 3.16 - Illustration of waveguide cavities with capacitive ‘iris’ aperture coupling

The coupling coefficient between the internal resonators controlled by the dimension *s*, is defined as a ratio of coupled energy to stored energy [3], as depicted in Figure 3.17.

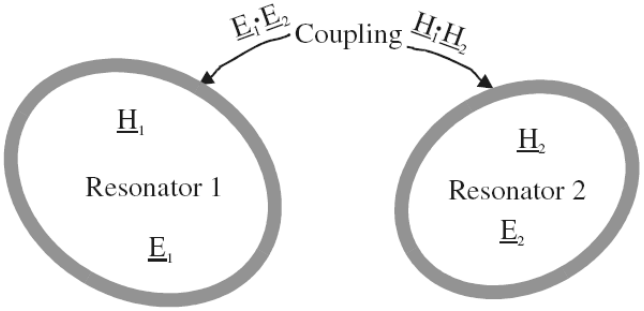

Figure 3.17- Coupling between two resonators. Taken from [3].

E and H are the electric and magnetic fields between the resonators that result in a superposition of magnetic and electric couplings. In the case of Figure 3.16 the irises orientation is orientated in the plane of the waveguides electric field, hence capacitive coupling between the resonating cavities will occur.

3.7 Conclusion

This chapter has shown some of the fundamental design principles needed for creating circuits using resonators. We have shown how to profile couplings to use with the coupling matrix filter solutions. We have outlined the resonator design principles of both microstrip and waveguide resonators.

We are now able to use this information to construct filter circuits in both microstrip and waveguide, and also later develop a theory in utilising this to integrate active devices with passive resonator circuits.

References

[1] **Pozar, D.M.** Microwave Engineering. Third edition, John Wiley & Sons, Inc, 2005.

[2] Lancaster, M. J. **Passive Microwave Device Applications of High-Temperature Superconductors**. Cambridge University Press, 1997.

[3] Hong Jia-Sheng, Lancaster Mike J. **Microstrip Filters for RF/Microwave Applications**. Wiley & Sons Inc., 2001.

[4] Mokhtaari M., Borenemann J., Rambabu K., Amari S. **Coupling Matrix Design of Dual and Triple Passband Filters**. IEEE Transactions on microwave theory and techniques, 2006. Vol. 54, issue 11, pages 3940-3946.

[5] Atia W. A., Zaki. K. A, and Atia A. E. **Synthesis of General Topology Multiple Coupled Resonator Filters by Optimisation**. IEEE MTTS International Microwave Symposium, 1998. Vol. 2, pages 821-824.

[6] Cameron, Richard J. **General Coupling Matrix Synthesis Methods for Chebyshev Filtering Functions.** IEEE Trans. on microwave theory and techniques, 1999. Vol 47, pages 433-442.

[7] **ADS 2011.** Advanced Design System. Agilent, 2011.

[8] **GmbH, CST.** CST Microwave Studio. Darmstadt, Germany. CST GmbH, 2012.

[9] **K.C. Gupta, Ramesh Garg, Inder Bahl, Prakash Bhatia.** Microstrip Lines and Slotlines. Artech House, London, 1996.

[10] David Glynn, Tianhao He, Jeff Powell, Yingtao Tian, Xiaobang Shang and Michael J. Lancaster. **Submillimetre Rectangular Waveguides based on SU-8 photoresist micromachining technology.** IEEE 46th European Microwave Conference (EuMC), 2016. Pages 1346-1349.

Chapter 4

Terahertz Waveguides

4.1 Introduction

Waveguides are vital microwave components for the transmission of energy and information from one location to another. They work by confining propagating energy into a single direction, while minimising losses.

Waveguides are the energy and information conduit of choice for many microwave applications, however, the desire to use the higher regions of the electromagnetic spectrum has made the construction of waveguide a challenge. This is due to the decreasing physical dimensions required for higher frequencies, and these demandingly small dimensions often go beyond the capabilities of conventional machining techniques. One method to tackle the challenges of constructing high frequency waveguide is to use micro machining technologies [4, 6, 11], such as SU-8 etching as described in this chapter. SU-8 is an epoxy based photo resist [1] that can be shaped into sheets patterned with designed cavities (using UV exposure and a precision mask), and these layers can be metal coated and built up into complicated waveguide structures. This technology enables rectangular waveguide transmission lines and passive circuits to be used for submillimeter frequency designs. Such micro-machined circuits are also ideal conduits for active components and enable novel methods of matching, allowing efficient high frequency systems to be constructed. One such circuit considered when initiating this thesis was the frequency multiplier. Multipliers are used as it is often difficult to generate a very high local oscillation frequency in a single step. Frequency multipliers typically utilize a nonlinear harmonic

response to distort a lower frequency into a required harmonic multiple. The frequency spans of the waveguide in this thesis were chosen to coincide with an input frequency for such a multiplying circuit. Care was taken to design the waveguide using just five layers of SU-8 photo resist, so that the waveguides orientations would allow an input circuit of 150 GHz to connect to a future frequency doubler design. It can be seen in this chapter that using just 5 layers for a 150 GHz waveguide has potential problems with the way the field must orientate within the waveguide, which unlike other similar layered waveguides constructed so far will have the layered gaps in the worst place for surface current interruption. It is therefore essential to build and test this waveguide to ensure its design is feasible for a future application. To measure the waveguide, a ninety degree E field plane bend [14] was designed and constructed to connect to test equipment, and potentially to other stages in a communication system.

4.2 150 GHz SU-8 Waveguide

The 150 GHz waveguide dimensions are derived from the WR-6 waveguide specification (a=1650 µm, b=830 µm), which covers the frequency range 110 GHz to 170 GHz. This was chosen for a 150 GHz centre frequency, which would be useful as it could form part of the local oscillator frequency multiplier circuit in a 300 GHz communication system. However, because the waveguide is to be constructed from layers of SU-8 photoresist, which has a thickness of 288 µm per layer, there is a restriction of using a multiple of 288 µm for one of its dimensions. This is because the layers of SU-8 are built up using a spin process to evenly spread the SU-8 material to a specific thickness. The acceleration and final spin rate are carefully controlled and the best repeatable results are obtained when targeting a spin thickness of 288 µm.

The process for SU-8 construction can be found in [1, 12]. This details the lithographic method of using ultra violet light exposure onto a layer of SU-8 material, screened by a precision mask. The mask determines which areas shall remain after an etching process. The etched SU-8 piece is then coated with a metal film.

The chosen implementation of the SU-8 photoresist layers is shown in Figure 4.1 and it can be seen that with just 5 layers a close approximation to WR-6 can be made. The only minor compromise is that the *b* dimension differs in the SU-8 case by a small increase of 34 µm (4%). A waveguide length of 16 mm was chosen for the waveguide as this will allow the test circuit to fit well with common lab test fixtures.

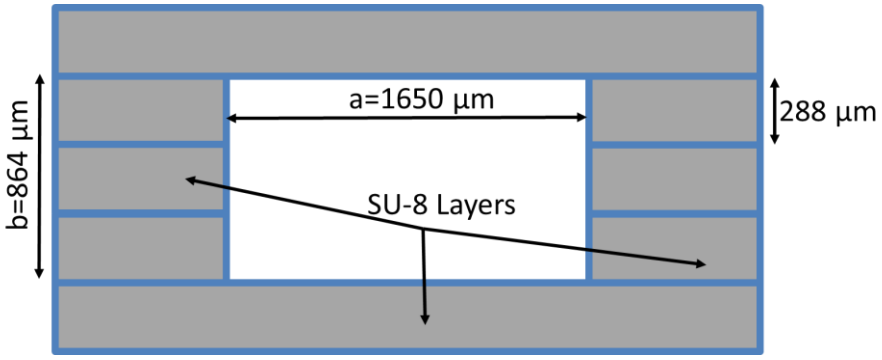

Figure 4.1 - WR-6 Waveguide structure with five SU-8 Layers

Five layers is also a good choice for the solution when considering real circuit applications as it allows us to construct coaxial lines from the SU-8 structure [2] as shown in Figure 4.2, which could be used for low loss long transmission paths within a communications system.

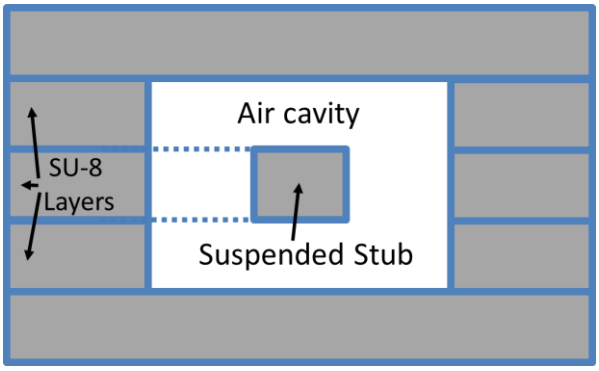

Figure 4.2- Example of a coaxial structure made with five SU-8 layers.

4.2.1 150 GHz SU-8 Waveguide Bend Design

Figure 4.3 [3] shows the currents and field orientations in a typical waveguide section and its dominant transverse electric propagation mode TE_{10}. In Figure 4.3, green denotes electric fields, purple denotes magnetic fields and the orange denotes surface currents. It can be seen that it is not desirable to have any gaps in the waveguide walls, as currents flowing on these surfaces will be interrupted.

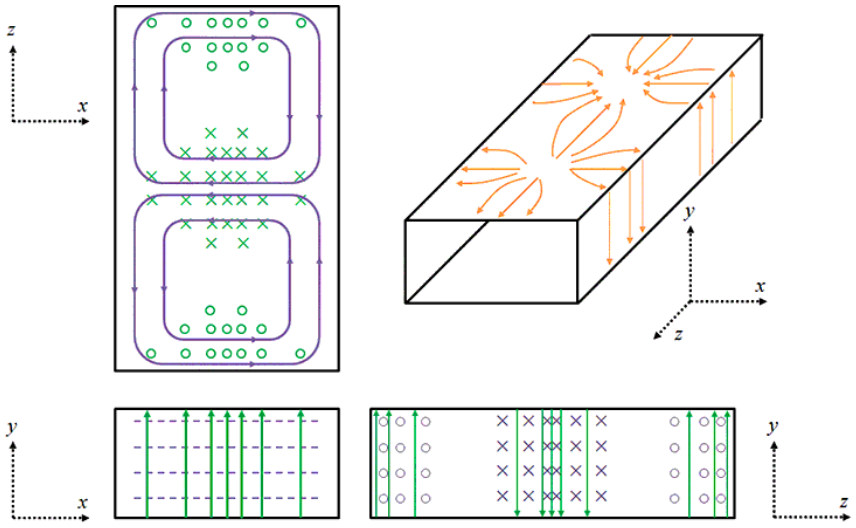

Figure 4.3 - TE_{10} Waveguide Propagation Mode (taken from [3])

To construct the waveguide shown in Figure 4.1, there will inevitably be gaps between the press fitted layers. If the surface currents for such a structure are considered, the situation shown in Figure 4.4 can be seen, where the surface current will cross the gaps, causing an undesirable discontinuity.

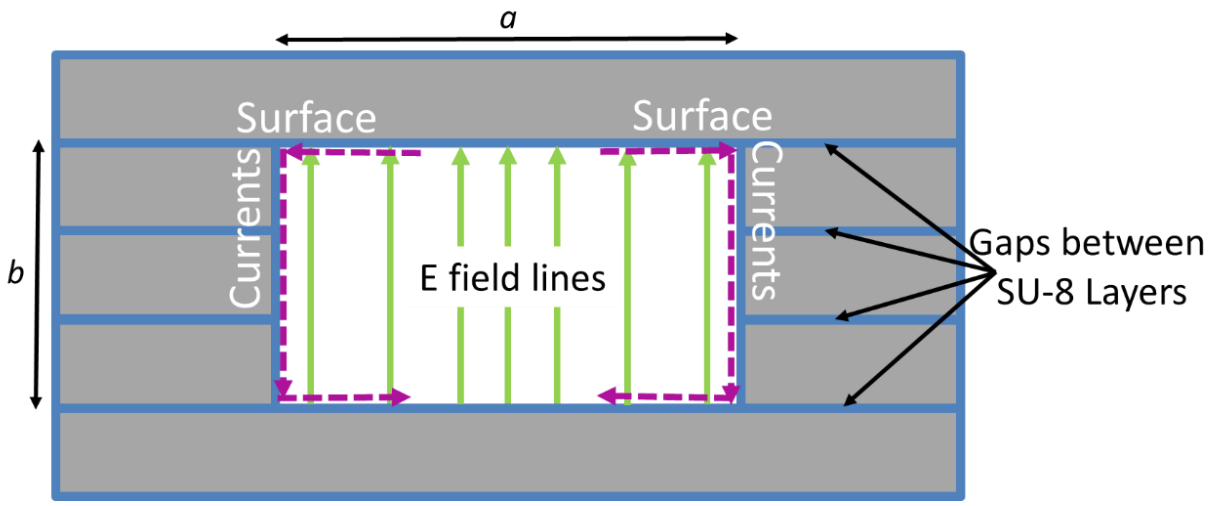

Figure 4.4 - E field lines (green), surface current (purple) and gaps within layered SU-8 waveguide structure

Previous waveguide designs [4,12,14] have had the advantage that the gaps appear along the `*a*` side, where interruptions to the surface currents are less problematic, however for the design because of the 150 GHz centre frequency and having five 288 µm SU-8 layers, the design is forced to have the gaps along the `*b*` side.

It is therefore essential to show that a waveguide constructed with `*b*` side layer gaps has an adequate performance for use in a communication system and that the channeled energy is not significantly lost along the layer gaps.

This problem was encountered in previous projects [4,5], showing that gaps formed by building the structure up from individually coated layers and press fitting them all together can be problematic. One way to reduce the impact of the layer gaps is to bind the layers together. The developed method to overcome this problem is to expose one layer of SU-8 and then add a second layer of SU-8, and then exposing that one before etching and coating to form a joined two layer structure. This method much reduces the gap between layers [6], and improves the waveguide performance.

Another problem to solve when constructing this waveguide is how to connect with the test equipment. The 150 GHz waveguide is to be constructed with 5 layers of SU-8 photoresist. Therefore the overall thickness of the device is $5 \times 288\ \mu m = 1440\ \mu m$. It is not possible to connect test equipment directly in-line to the constructed SU-8 waveguide due to the thinness of the final structure, and also it would be very difficult to manufacture a test port on the edge of a SU-8 sheet. It is therefore necessary to construct two ninety degree E plane bends to allow the connection of test equipment to the waveguide section. Figure 4.5 shows a cross section of a three step design concept for the bends.

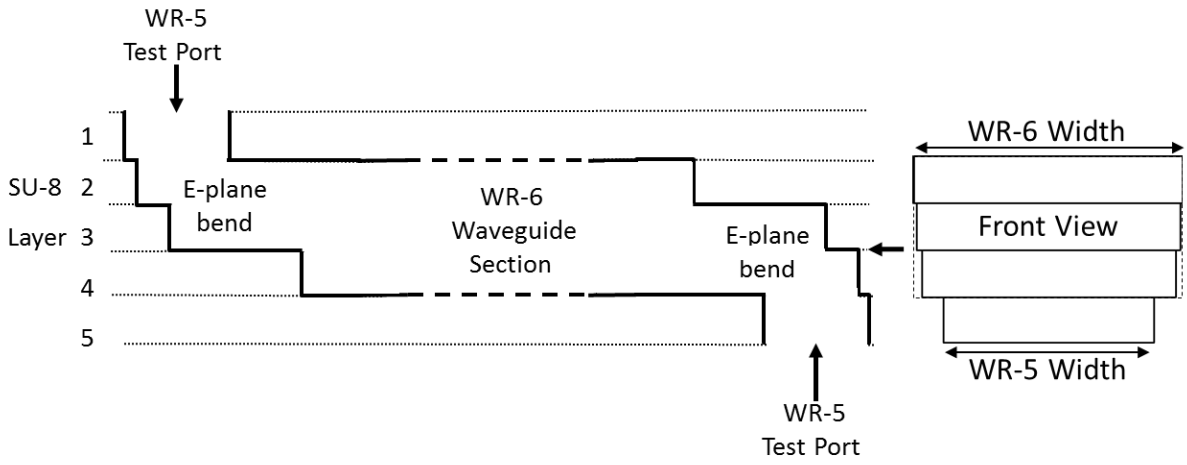

Figure 4.5 - Cross section of SU-8 Waveguide Structure

An additional complication to consider when designing the WR-6 waveguide, is that only WR-5 (a=1295.4 µm, b=677.7 µm) test heads are available for the laboratory Vector Network Analyser. Therefore a conversion is required from the WR-5 test head to the WR-6 waveguide section, and this was done as part of the bend structure, which is illustrated in the front view of Figure 4.5.

The bend was designed by constructing a parameterized staircase structure using 3-D electromagnetic modelling software package. The steps widen gradually from the WR-5 test head orifice to the WR-6 waveguide section. A simple optimisation routine was used to adjust each step to find the best solution. Commercial machined 90 degree waveguide bends tend to be as smooth as machining will allow for the greatest reduction in reflection, however a curved bend is impossible to achieve when using five layers of material that can only be etched perpendicular to the plane, so the best alternative is a stepped bend. It can be seen in [7] however that having a bend consisting of just a few steps can give good results. With this in mind an extra step was created by offsetting the waveguide port by adjusting the test equipment's WR-5 connection location slightly, as shown in Figure 4.6.

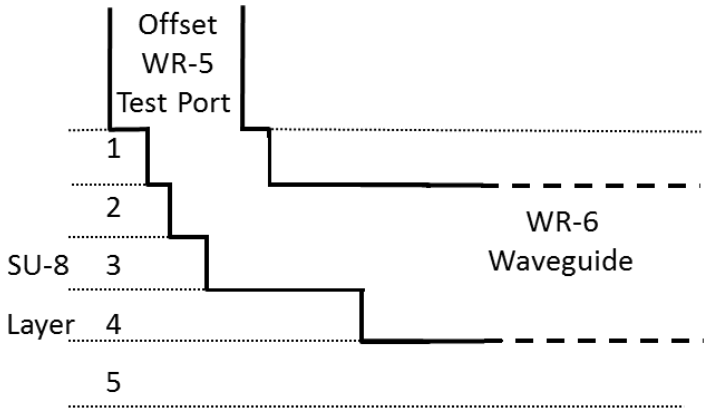

Figure 4.6 - Waveguide Cross section with Extra Step

A 3-D view of the optimized waveguide bend model can be seen in Figure 4.7.

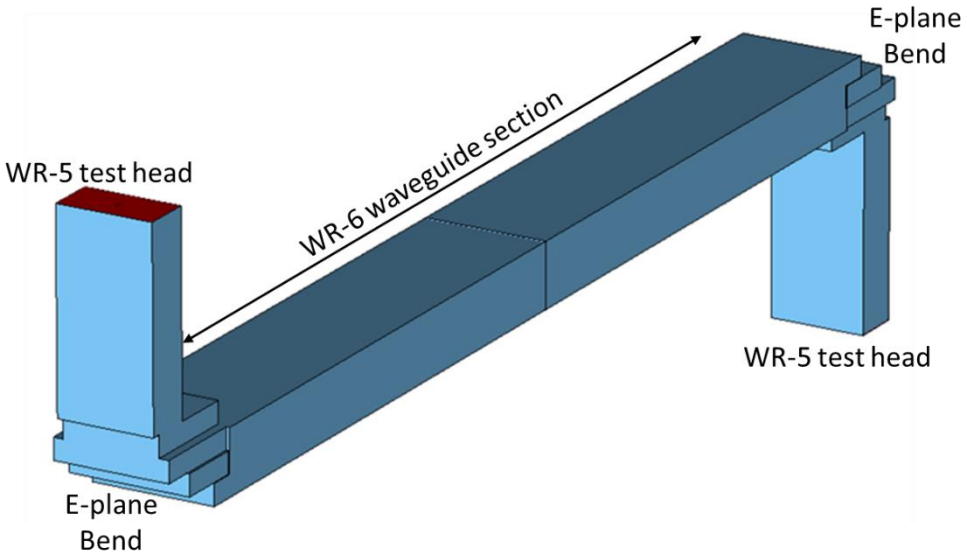

Figure 4.7 – 3-D Waveguide Bend Structure.

In Figure 4.7, blue denotes vacuum, with the boundary of the model being perfect electrical conductor. The red rectangle shown is the model's test port. The test equipment waveguide ports have been left attached to highlight the staggered offset connection required.

Two identical brass plates were manufactured to sandwich the SU-8 layers and also facilitate the accurate connection dowels and fastening screws essential for alignment, connection and testing. One of these plates is illustrated in Figure 4.8.

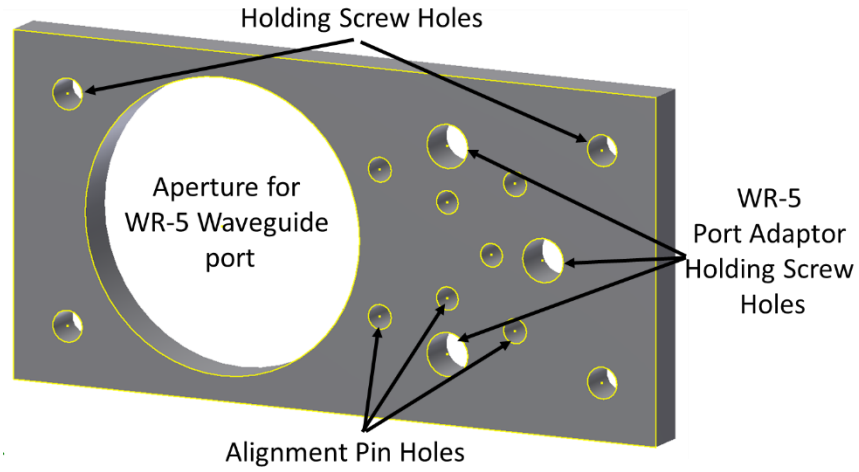

Figure 4.8 - Brass Waveguide Bend test plate

The 3-D model in Figure 4.7 is converted to the 5 layers needed to construct the UV exposure masks, as shown in Figure 4.9.

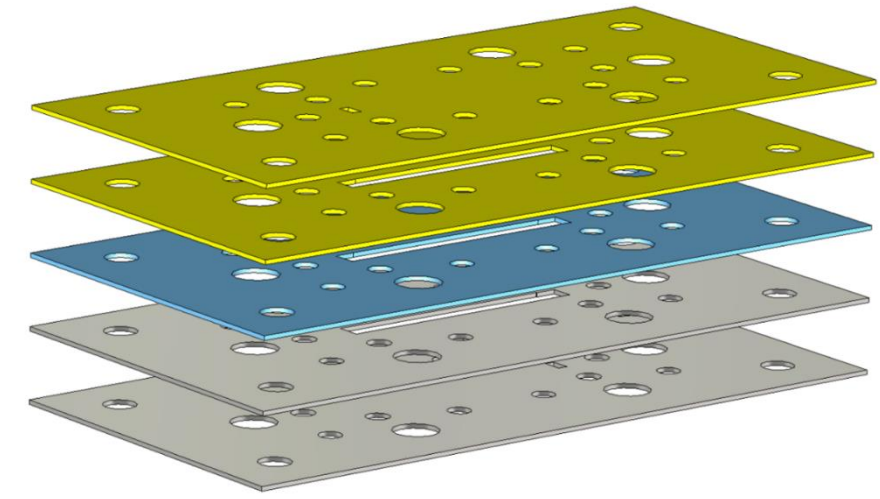

Figure 4.9 - SU-8 Layers forming the waveguide structure. Colours indicate which layers are to be joined into a single piece

The different false colours are to indicate which layers are to be joined together to form a single piece before the metal coating. The resultant structure can therefore be considered as a 3 layer SU-8 waveguide with two 90 degree E plane bends.

The completed waveguide bend SU-8 structure and brass mounting plates can be seen in Figure 4.10. Note that a second high accuracy alignment pin is omitted as its position would be through the waveguide structure.

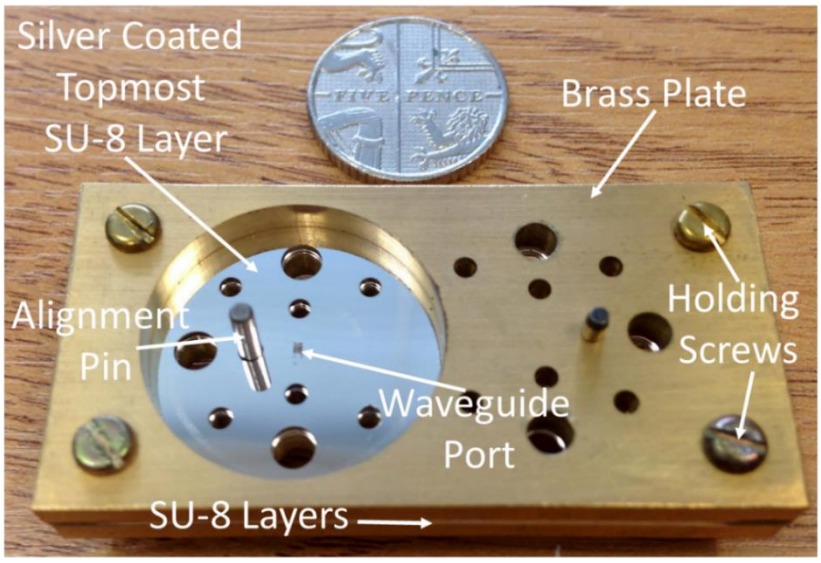

Figure 4.10 - Photograph of the assembled waveguide bend layered structure and adaptor plates

4.2.2 150 GHz Waveguide Test and Results

The 150 GHz waveguide was tested using an Agilent E8361A Vector Network Analyser, and the test setup is shown in the photograph in Figure 4.11, which shows the WR-5 test heads offset mounted into the brass plates which sandwich the SU-8 layers.

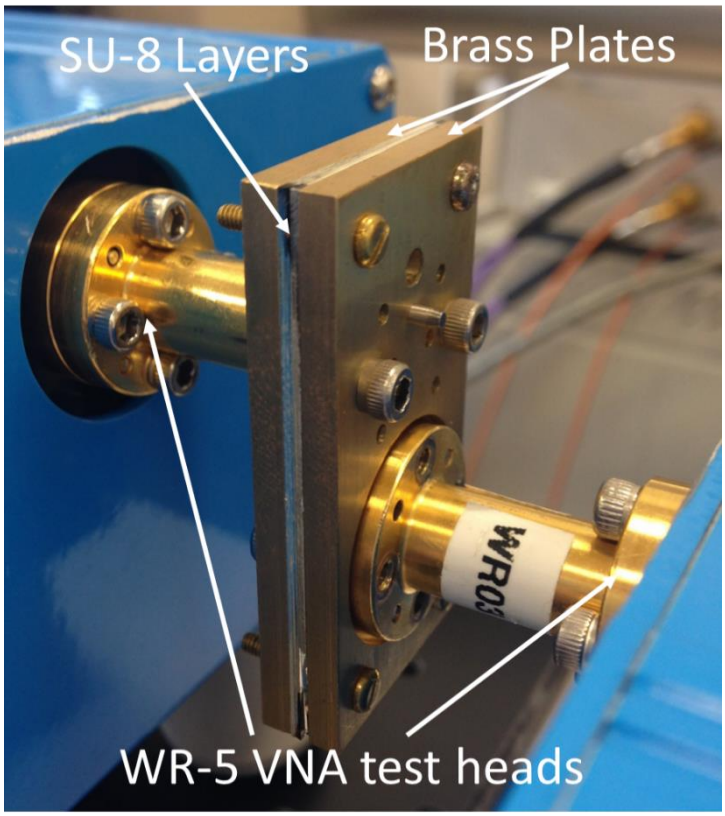

Figure 4.11 - Photograph of waveguide bend test fixture, ports and VNA test heads

The Agilent E8361A Vector Network Analyser only covers the range 140 GHz to 220 GHz as shown in Figure 4.12 . The simulated range is from 120 GHz to 170 GHz, so only measured results from 140 GHz upwards, as shown in Figure 4.13 and Figure 4.14 can be reported. The gain shown in Figure 4.14 is because of a problem with the VNA receive head which has a ~6dB mismatch causing the calibration routines to struggle to produce a smooth response [8]. Noisy calibrations at this frequency and with this test equipment were difficult to avoid, and the calibration was repeated several times, and measurements taken with averaging over sweeps to try to eliminate this effect. However, even after calibration with the “through” attached, a noisy

result showing gain in places was still observed. The drop in response in the 145 GHz to 150 GHz region may be due to the effect of radiation loss through the remaining gaps between the SU-8 layers. The effect could be worsened by releasing the pressure between the brass mounting plates, while the result seen was taken with the highest torque applied without wanting to risk the integrity of the circuit layers. Some of the measured loss can also be accounted as perfect electrical conductor was used in the simulation model, and the use of SU-8 will add some losses compared to this. The measured loss per mm has also been shown in Figure 4.15. It can be seen that both S_{11} and S_{21} follow the simulated results well.

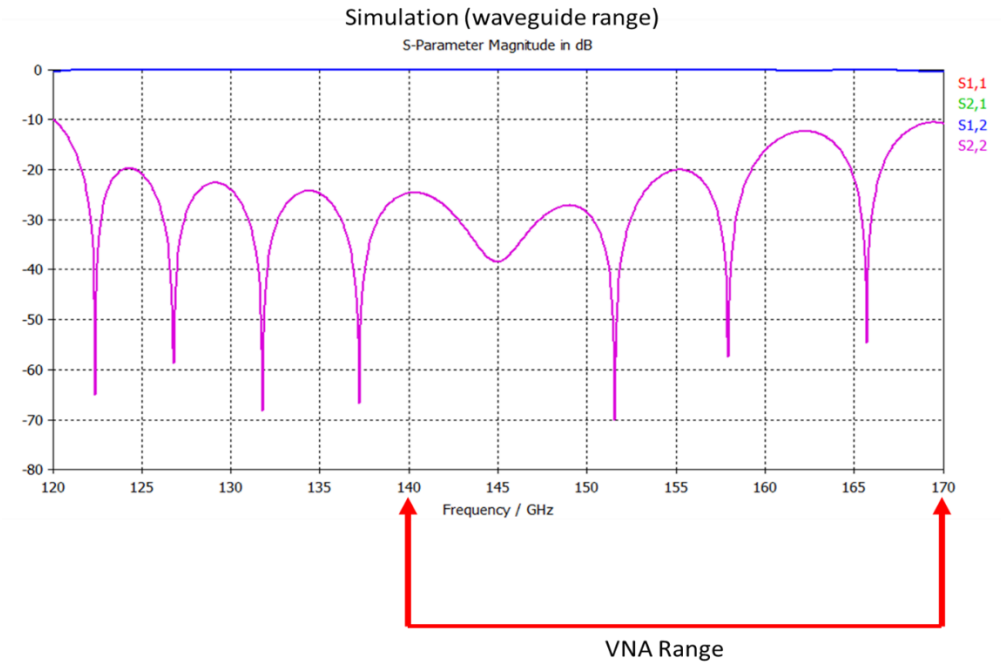

Figure 4.12 - Simulated results with VNA frequency range indicated

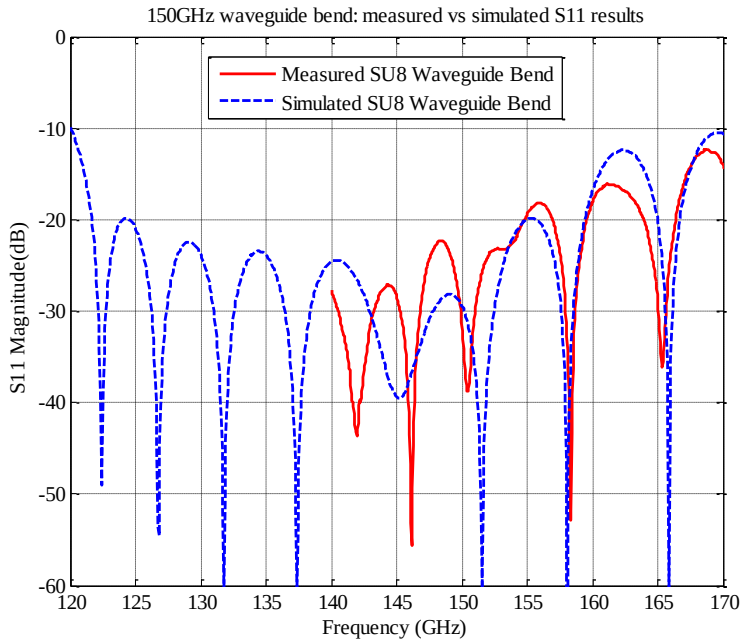

Figure 4.13 - S_{11} Results, measured and simulated

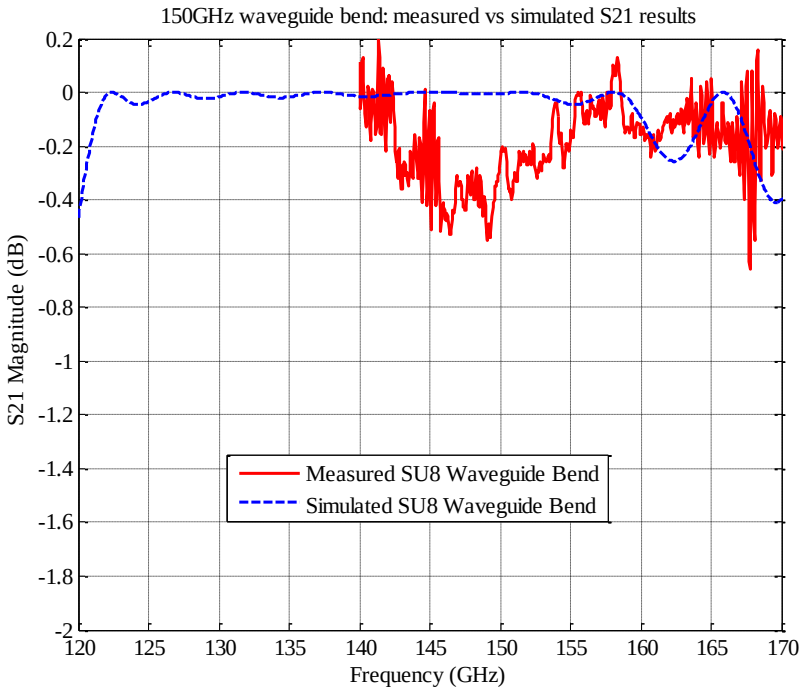

Figure 4.14 - S_{21} Results Measured and simulated

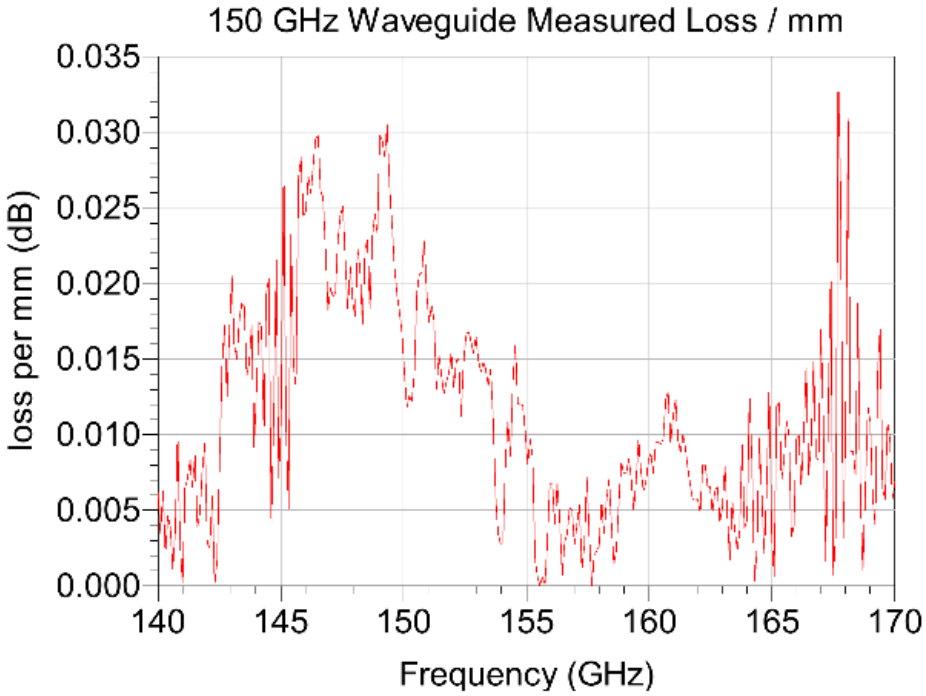

Figure 4.15 - Measured Insertion less of waveguide bend

A tolerance analysis based on the measured dimensions of the dismantled bend was initiated to determine how much an effect in the performance of the bend can be attributed to manufacturing dimension variability. The variation in dimensions could be caused by

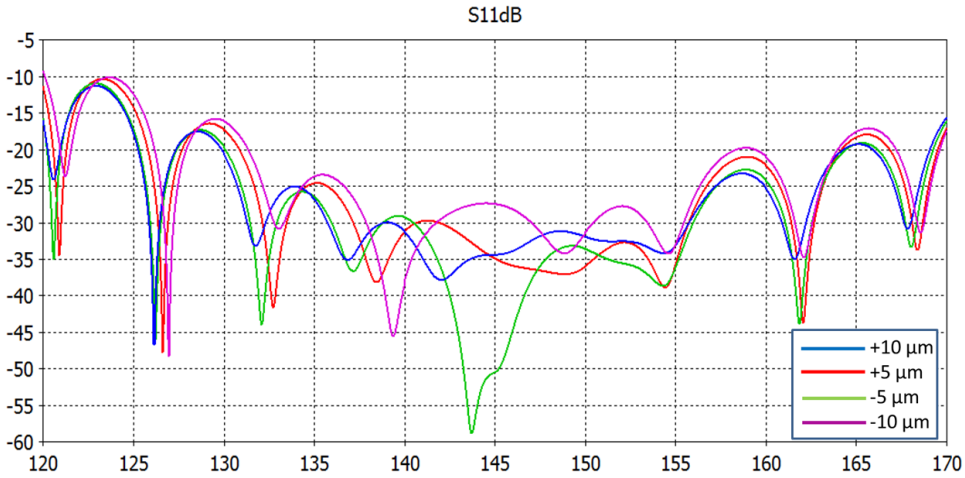

Figure 4.16 - Simulated tolerance analysis (all waveguide dimensions)

inaccuracies in the generation and application of the UV exposure masks and also the SU-8 layer thickness variability caused by inaccuracies in the spinning process. It was found that width and length dimensions varied by about 5 µm, with some dimensions varying up to 10 µm, so the tolerance simulation was set up to measure dimension variations of +/- 5 µm and +/- 10 µm. Figure 4.16 shows the effect of the variation of all the parameterised dimensions, i.e. all widths, lengths and also SU-8 layer thicknesses. The thickness variation of each of the assembled SU-8 layers was found to also be within +/- 10 µm, and the overall assembled thickness was within 30 µm of the anticipated 5 x 288 µm range. Figure 4.17 shows an analysis of varying each layer by +/- 10 µm to see the effect on the performance. It can be seen that even with all these variations in the waveguides dimensions the simulated results are not dramatically affected.

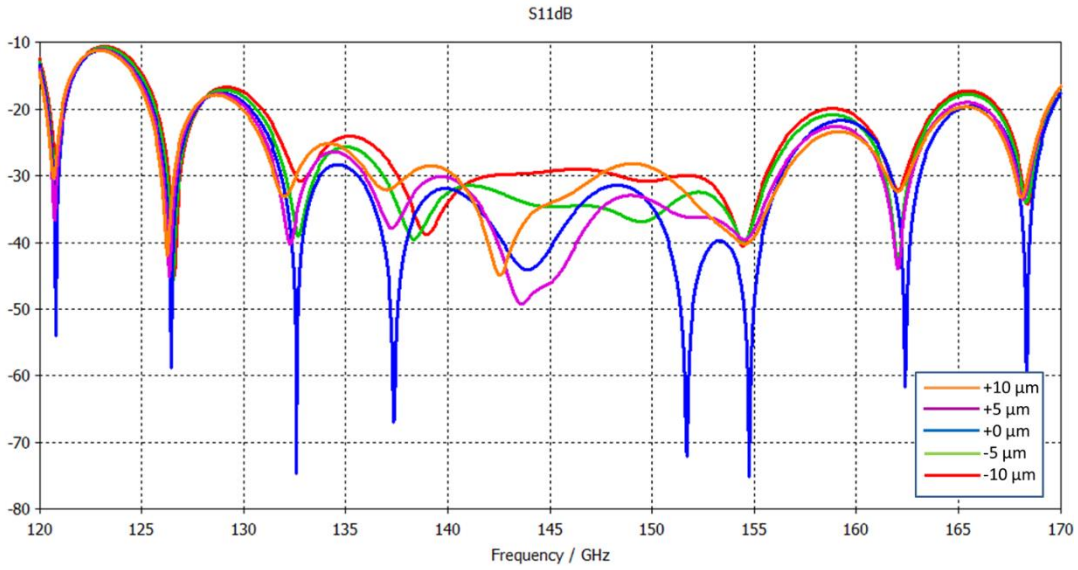

Figure 4.17 - Simulated tolerance analysis (SU-8 thickness only)

Another factor that could detrimentally affect the performance of the waveguide by causing additional losses is the surface roughness of the material used, such as silver coated SU-8 for the manufactured waveguide. This is due to additional scattering of the wave from the surface of the material. An estimate of this loss can be found using: [9]

$$\frac{\alpha_c}{\alpha_{c0}} = 1 + \frac{2}{\pi} tan^{-1}\left(1.4\left(\frac{\Delta}{\delta}\right)^2\right) \quad 4.1$$

Where α_c is the attenuation in dB/m of a conductor with surface roughness Δ, α_{c0} is the loss in dB of a perfectly smooth conductor ($\Delta = 0$) and δ is the skin depth given by:[10]

$$\delta = \sqrt{\frac{2}{\omega \mu_r \sigma}} \quad 4.2$$

Where μ_r is the permeability of the conducting material and σ is the conductivity. So the silver coating has a permeability of approximately 1 [11] and conductivity of 6.21×10^7 Siemens per metre. Using equation 4.2 this gives a skin depth of 0.18μm at 150 GHz, which is much less than the silver coating which is controlled in the coating process to be approximately 2 μm thick. Using the results from [12,13] it can be seen that the root mean square surface roughness of the SU-8 is measured to be around 40-50 nm before and also after the silver metallisation process. Substituting in a midpoint of 45 nm for the surface roughness into equation 4.1, the loss is calculated to be 0.014 dB/mm. Therefore, neither the surface roughness nor the skin depth of the metallisation is a significant factor in the losses measured for the waveguide, which as previously mentioned are probably due to radiation losses from gaps between the SU-8 layers.

4.3 Conclusion

It has been shown that is it possible to construct a usable WR-6 waveguide using 5 layers of SU-8 material employing the two layer joining technique of [4]. It has also been shown that it is possible to convert waveguide size while performing a 90 degree E plane bend for the design without a significant increase in reflected signal from the waveguide structure. All these techniques are valuable for the construction of a SU-8 structured terahertz receiver system. To put this work into context, Table 4.1 shows results of similar work using a variety of manufacturing methods obtained from [8]. It can be seen that this method of waveguide fabrication gives very competitive results as well as a low bulk cost of manufacturing compared to more conventional machining techniques. The better result of the waveguide detailed in this chapter, compared to the other waveguides operating at higher frequencies could be attributed to the increasing detrimental effect of manufacturing tolerances at higher frequencies. The work here has also been presented in the paper found in appendix 1, [14].

Table 4.1 – Comparison of similar waveguide structures

	Techniques employed	Length (mm)	Insertion loss	Return loss	Reference
WR-6 Waveguide by EDT (this work)	SU-8	15.95	0.009-0.034 dB/mm Average: **0.011 dB/mm**	Better than 12.3 dB (140-170 GHz)	[14]
Straight WG by RAL	CNC milling, then gold plating	51	0.017-0.025 dB/mm Average: **0.021 dB/mm**	Better than 22 dB (220-325 GHz)	[12]
Straight WG by University of Virginia	KMPR based UV-LIGA	23.88	0.042-0.126dB/mm Average: **0.096 dB/mm**	Average: 13.5 dB (220-325 GHz)	[15]
Straight WG by University of Virginia	SU-8	11.4	0.088-0.438dB/mm Average:**0.263 dB/mm**	Average: 15 dB (220-325 GHz)	[16]
A Gold Plated Waveguide by ALMA	CNC milling, then gold plating	254	0.013-0.017dB/mm Average: **0.015 dB/mm**	Better than 25 dB (210-280GHz)	[17]
Straight WG by University of Leeds	SU-8	8	Average: **0.75 dB/mm**	Average:12 dB (220-325 GHz)	[18]

References

[1] Micro Chem. Nano™ SU-8, negative tone photoresist formulations. http://www.microchem.com/pdf/SU8_50-100.pdf

[2] Maolong Ke, Yi Wang, Kyle Jiang, Michael J. Lancaster. **Micromachined Rectangular Coaxial Line and Cavity Resonator for 77 GHz Applications using SU8 Photoresist** . IEEE Asia-Pacific Microwave Conference, 2008. Pages 1-4.

[3] Microwave_Studio, CST. 2011. "CST GmbH." Darmstadt.

[4] X. Shang, M.L. Ke, Y. Wang and M.J. Lancaster. **A Micromachined WR-3 Waveguide Filter With Embedded Bends**. Electronics Letters, 2011. Volume 47, issue 9, pages 545–547.

[5] X. Shang, M.J. Lancaster, M. Ke, Y. Wang. **Measurements of Micromachined Submillimter Waveguide Circuits.** IEEE Microwave Measurement Symposium (ARFTG), Florida, 2010. Pages 1–4.

[6] Ke M., Shang X., Wang Y., Lancaster M. J. 2011. **Improved Insertion Loss for a WR-3 Waveguide Using Fully Cross-Linked Two-layer SU8 Processing Technology**. The 12th International Symposium on RF-MEMS and RF-Microsystems (MEMSWAVE 2011), Athens. Pages 232-237.

[7] Kirilenko, Sergey F. Kulishenko and Anatoly A. **Waveguide Bend Matched by the Stepped Miter.** International Conference on Antenna Theory and Techniques, Sevastopol, 2003. Volume 2, pages 767-768.

[8] Yi Wang, Michael J. Lancaster, Maolong Ke, Xiaobang Shang. **Measurements of Micromachined Waveguide Devices at WR-3 Band using a T/R-T Module Based Network Analyzer.** Microwave Measurement Conference (77th ARFTG), 2011. Pages 1-4.

[9] Milan V. Lukic, Dejan S. Filipovic. **Modeling of 3-D Surface Roughness Effects With Application to Coaxial Lines**. IEEE Transations on Microwave Theory and Techniques, 2007. Volume 55, issue 3, pages 518-525.

[10] Pozar, D.M. **Microwave Engineering**. J. Wiley, 2005.

[11] Nathan Ida, **Engineering Electromagnetics**. Springer Science, 2000.

[12] Shang Xiaobang, Ke Maolong,Wang Yi, and M. J. Lancaster. **WR-3 band waveguides and filters fabricated using su8 photoresist micromachining technology**. IEEE Transactions on Terahertz Science and Technology, 2012.Volume 2, issue 6, pages 629-637.

[13] Y. Wang, M.L. Ke, M.J. Lancaster, J. Chen. **Micromachined 300 GHz SU8 based slotted waveguide antenna**. IEEE Antennas and Wireless Components Letters, 2011. Volume 10, pages 573-576.

[14] David Glynn, Tianhao He, Jeff Powell, Yingtao Tian, Xiaobang Shang and Michael J. Lancaster. **Submillimetre Rectangular Waveguides based on SU-8 photoresist micromachining technology**. IEEE 46th European Microwave Conference (EuMC), 2016. Pages 1346-1349.

[15] J. R. Stanec and N. S. Barker, **Fabrication and integration of micro-machined millimeter-wave circuits.** IEEE Microwave Wireless Components Letters, 2011. Volume 21, no. 8, pages 409–411.

[16] C. H. Smith, III, A. Sklavounos, and N. S. Barker. **SU-8 micromachining of millimeter and submillimeter-wave waveguide circuits.** IEEE International Microwave Symposium, 2009. Pages 961-964.

[17] A. R. Kerr, C. Litton, G. Petencin, D. Koller, andM. Shannon. **Loss of gold plated waveguides at 210-280 GHz.** ALMA Memo 585, 2009.

[18] W. H. Chow, A. Champion, and D. P. Steenson. **Measurements to 320 GHz of millimetre-wave waveguide components made by high precision and economic micro-machining techniques.** High Frequency Postgraduate Student Colloquium. 2003. Pages 90-93.

Chapter 5

Coupling Matrix Filter Design

5.1 Introduction

Using the theory work outlined in Chapter 3, it is possible to design and construct filters from resonating elements, by analysing and arranging them using coupling matrix techniques. In this chapter two different implementations of this design method are shown. The first design uses microstrip lines as resonators that are proximity coupled to other lines. The second design uses waveguide cavity resonators that are coupled using irises. The purpose of this chapter is to demonstrate the coupling matrix approach and show two clear examples of its implementations, with measured results from a physical circuit.

5.2.1 Microstrip coupled line Bandpass Filters Using the Coupling Matrix

Microstrip coupled lines can be used to construct a bandpass filter by the analysis method outlined in chapter 3. This section demonstrates this to show the versatility of the method and ease of determining a set of filter solutions to suit the bandwidth requirements for a particular application in microstrip.

A three pole filter of centre frequency 9 GHz with a target return loss of -20 dB is to be constructed. The implementation of the microstrip coupled line bandpass filter is shown in Figure 5.1. The figure shows the external coupling gaps d_1 and d_4, and internal coupling gaps d_2 and d_3, and also labels the three resonators R_1, R_2 and R_3.

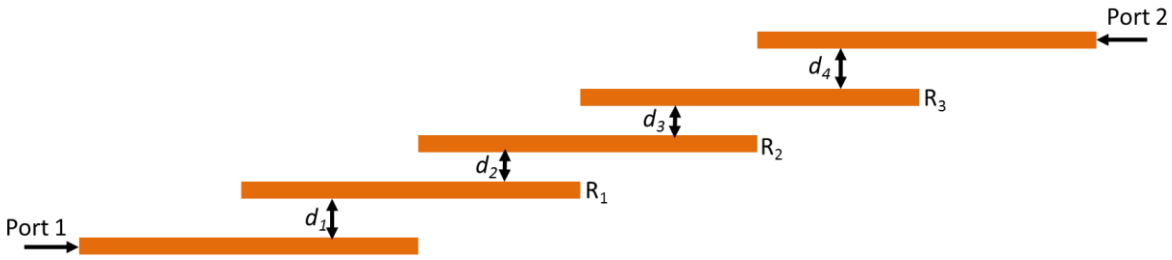

Figure 5.1 - Structure of microstrip coupled line bandpass filter

The width of a resonator will affect the unloaded *Q*, and the width at the resonator end will affect how it couples to the next resonator, which will influence the bandwidth of the filter. The track width chosen therefore should take the desired filter bandwidth into consideration. The input track has an impedance of 50 Ω to match with common test equipment. For 9 GHz this will be 0.74 mm (see chapter 3 using a substrate with dielectric constant of 2.33 and dielectric thickness of 0.254 mm).

From chapter 3 it is known that that the first requirement is to profile the external coupling *Q*. This requires the setup in Figure 5.2 to be constructed to allow this measurement to be made. The greyed out resonators are in practice removed from the simulator to eliminate spurious couplings, but they are left in the diagram for navigation purposes.

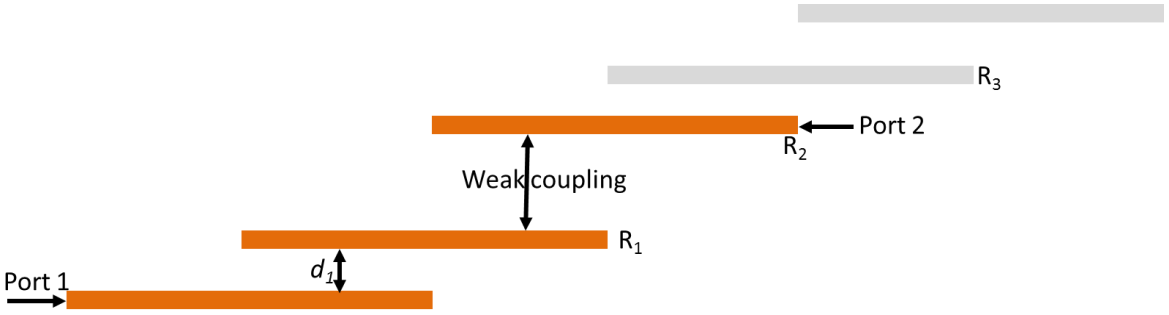

Figure 5.2 - Circuit configuration to measure external *Q*

The gap d_1 is swept through values starting from the narrowest gap that can be fabricated, to a value of Q that is beyond the application bandwidth requirement for the final filter. The plot in Figure 5.3 was obtained, which shows the S_{21} profile for each of the d_1 steps. For each curve in Figure 5.3 the Q can be obtained using the method outlined in chapter 3, and these values are shown in Figure 5.4.

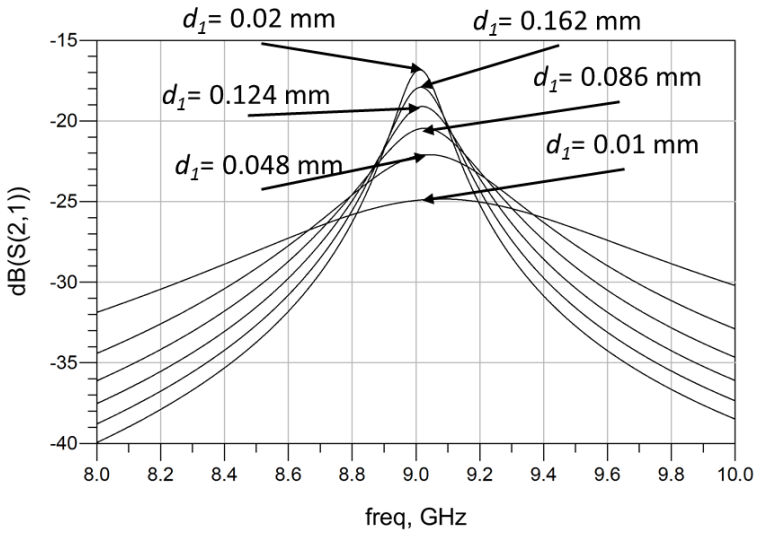

Figure 5.3 - Set of Curve produced by sweeping external gap width

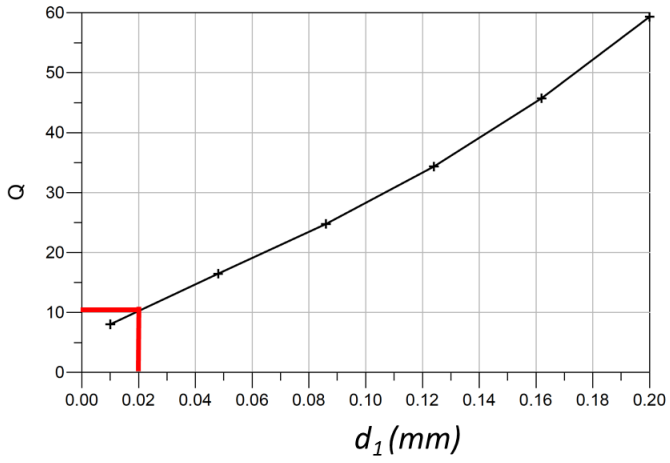

Figure 5.4 - Range of Q values from sweep of gaps. Chosen solution marked in red.

The next step is to profile the internal couplings, *k*. The circuit configuration in Figure 5.5 was constructed for this purpose and the *k* parameter was swept through a range of gap sizes.

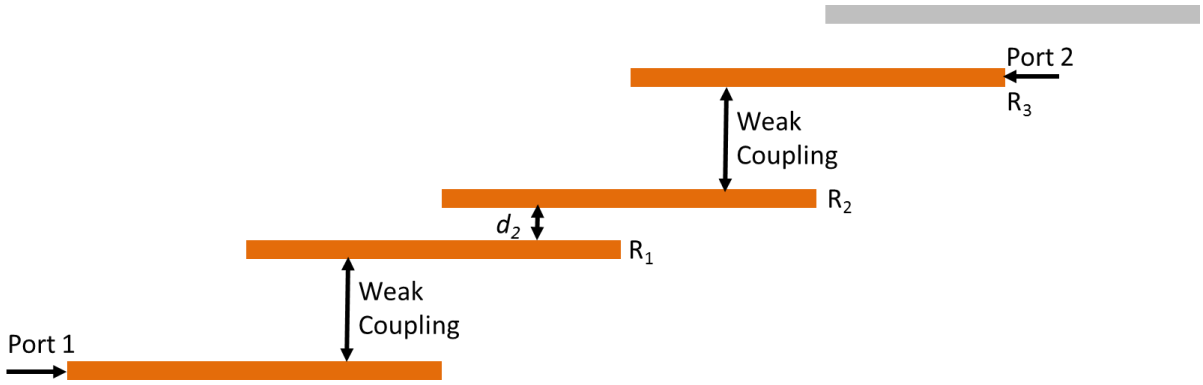

Figure 5.5 - Circuit setup for measuring internal coupling *k*

Figure 5.6 shows the set of two peak curves obtained during the d_2 sweep, and Figure 5.7 shows the resultant *k* values calculated from each curve shown, as described in chapter 3.

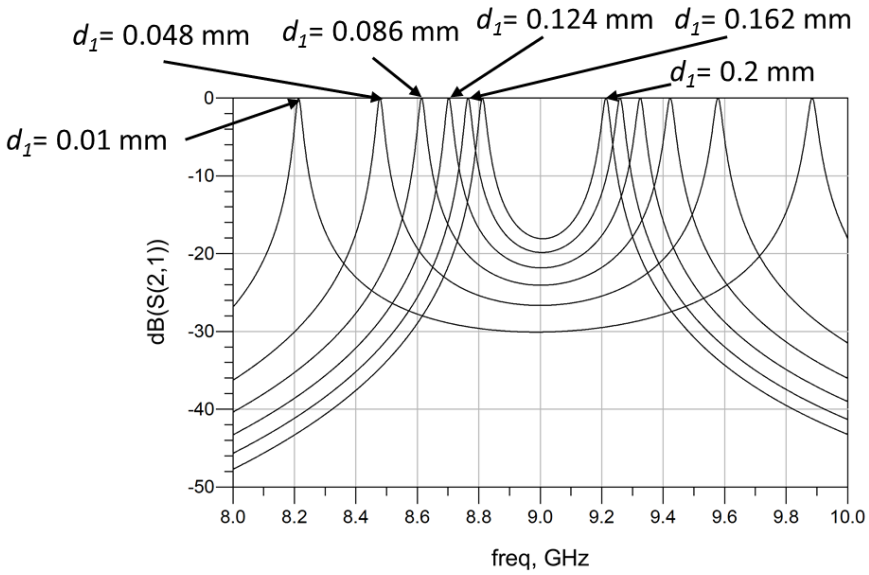

Figure 5.6 - Range of two peak curve obtained from sweeping internal gap *k*

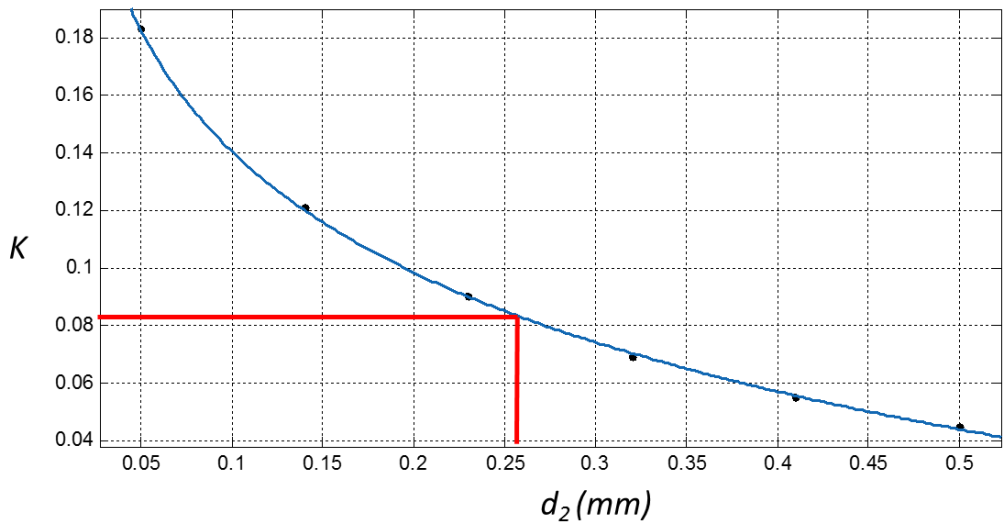

Figure 5.7 - *k* values obtained from internal gap sweep. Chosen solution marked in red.

With the *Q* and *k*'s profiled, a filter solution can be sought using the coupling matrix method. The solution is obtained using a mathematical computer aided design package, which can calculate a filter solution for whatever design parameters are chosen.

Figure 5.8 shows the response for a three pole / resonator filter, with a return loss of -20 dB, bandwidth of 0.75 GHz and a centre frequency of 9 GHz, with Q = 10.22 and k = 0.086 for a filter bandwidth of 0.75 GHz.

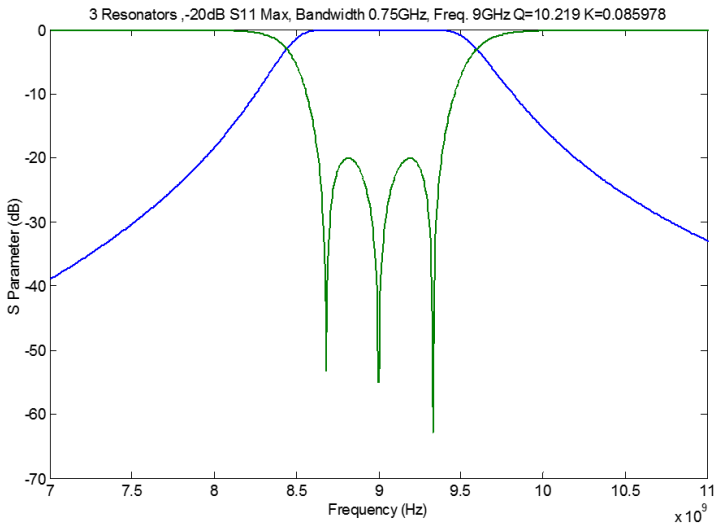

Figure 5.8 – Filter response from Coupling Matrix

Figure 5.8 is created using a coupling matrix with the g values in table 5.1 as detailed in chapter 2.

Table 5.1: g values for Chebyshev filter specification

g_0	g_1	g_2	g_3	g_4
1	0.8516	1.1032	0.8516	1

So the external quality factor matrix *[Q]* is:

$$[Q] = \begin{bmatrix} 0.0979 & 0 & 0 \\ 0 & 0 & 0 \\ 0 & 0 & 0.0979 \end{bmatrix} \qquad 5.1$$

And the normalised coupling matrix *[m]* can be given as:

$$[m] = \begin{bmatrix} 0 & 1.0317 & 0 \\ 1.0317 & 0 & 1.0317 \\ 0 & 1.0317 & 0 \end{bmatrix} \quad 5.2$$

The *Q* and *k* values that are required for the filter solution have been obtained, as have the curves to be used to determine the physical gaps required in the filter structure to meet these values. The three resonator filter can now be constructed using a gap of *Q* gap of 0.02mm and a *k* gap of 0.26mm. Figure 5.9 shows the 'first attempt' simulation plot of this filter solution, and a good filter result can be seen with three poles in the S_{11} response and a reasonably flat passband with sharp rejection over the approximately correct bandwidth.

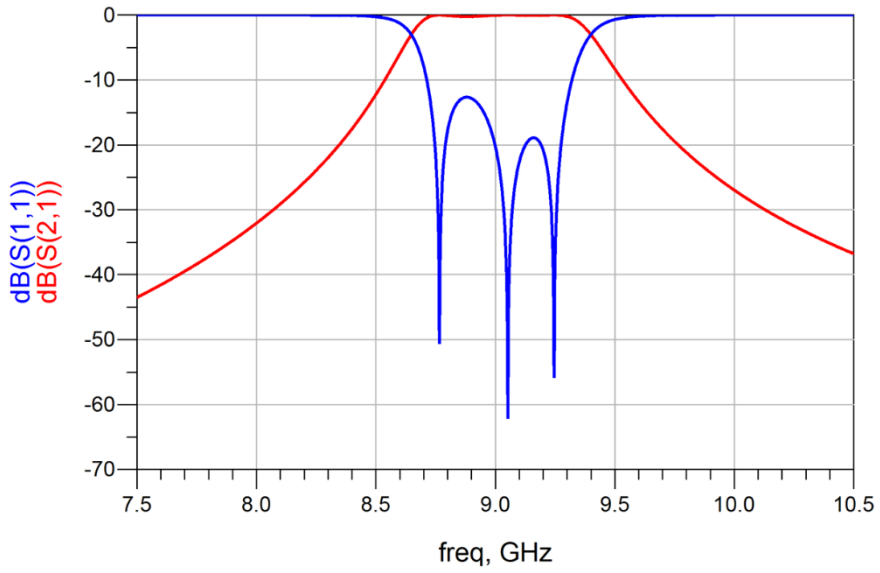

Figure 5.9 - First attempt filter simulation

The response can be improved as shown in Figure 5.10, by running a simulation optimisation to fine tune the parameters.

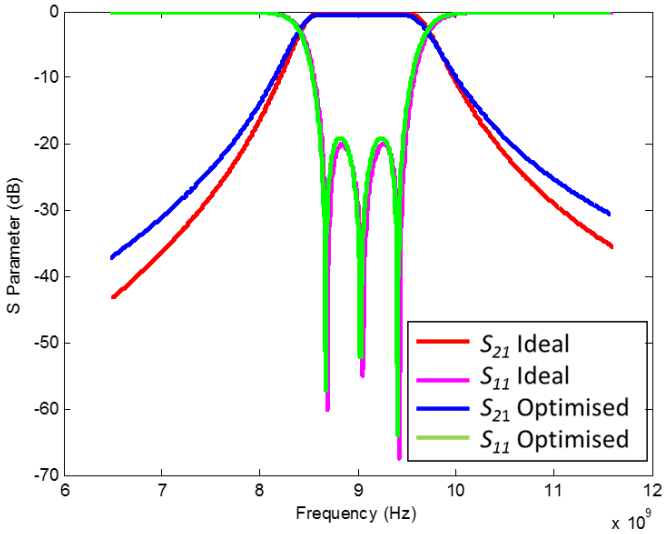

Figure 5.10 - Optimised filter solution with calculated ideal response for comparison

Filter gradient optimised for S_{11} goal of -20 dB at 8.9 GHz and 9.1 GHz

Now that the simulated filter response meets the specification, the filter is ready for fabrication, and the final dimensions are shown in Figure 5.11 and table 5.2.

Table 5.2 – Filter parameters required for fabrication

Parameter	Initial Values (mm)	Post Optimisation Values (mm)
l_q	0.	0.02
l_k	0.26	0.33
l_t	0.183	0.183
l_l	12.0	11.912

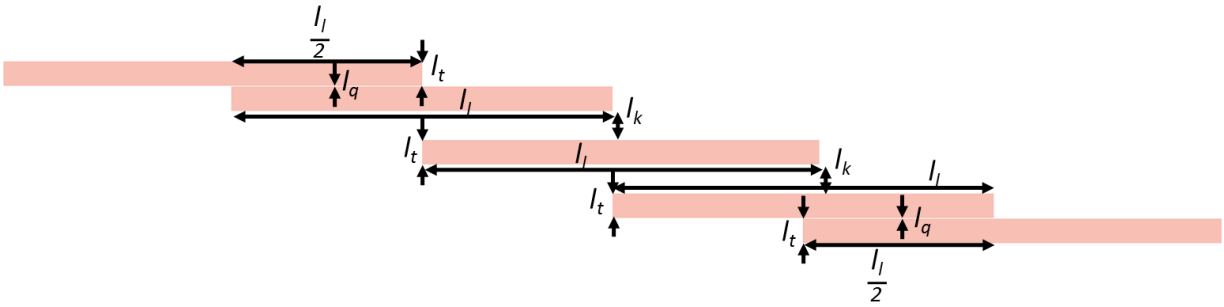

Figure 5.11 - Dimensions for filter fabrication

5.2.2 Microstrip filter experimental results

Figure 5.12 shows the fabricated filter, which has been fitted with connectors for attaching to a network analyser. The resultant response of the circuit is shown in Figure 5.13.

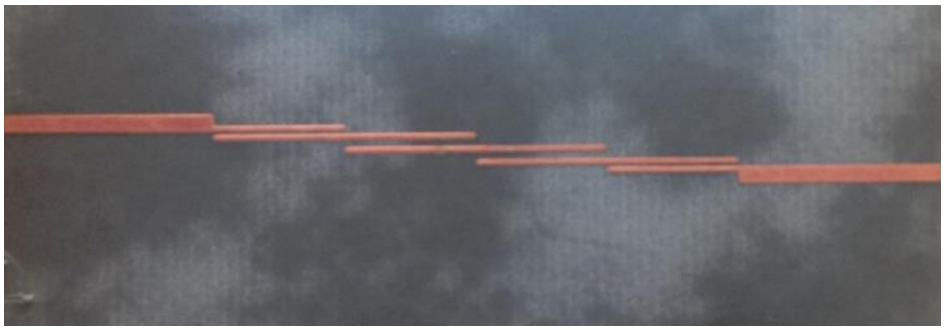

Figure 5.12 - Fabricated 9 GHz microstrip filter

The measured results show an insertion loss of about 0.8 dB, a return loss of -15 dB, and a 0.75 GHz bandwidth with a centre frequency of 9.1 GHz. On inspecting with a microscope, the fabricated tracks revealed the gaps to be larger than anticipated. The gap d_2 in Figure 5.*1* was

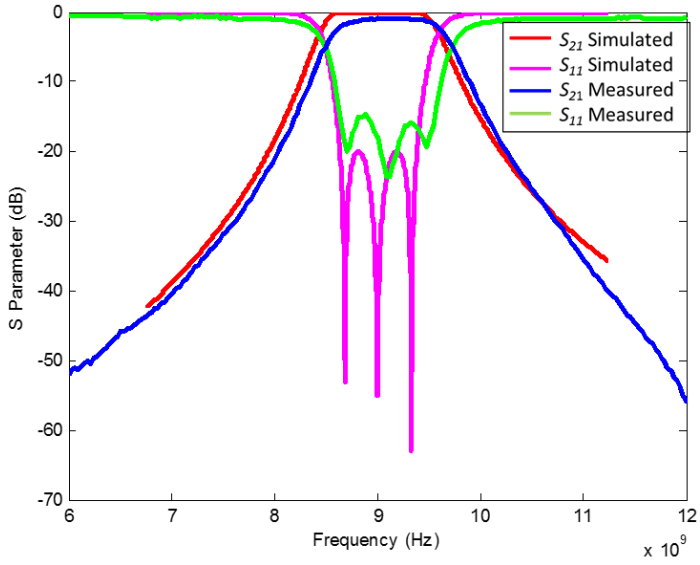

Figure 5.13 - Measured result of fabricated 9 GHz microstrip filter
With the optimised simulation result for comparison

measured to be 0.36 mm and the d_1 gap was 0.04 mm. Substituting these values back into the simulation gives the result in Figure 5.14, which gives a very similar S_{11} and bandwidth response to that of the measured circuit.

The 0.8 dB insertion loss was investigated and partly accounted for (0.2dB extra loss) when the simulation was performed using copper as the conductive material, rather than perfect electrical conductor (P.E.C.). Finally, the filter was not packaged into a conductive box and radiation losses can contribute in part also, as well as a 0.1dB contribution from the connectors and input and output track lengths.

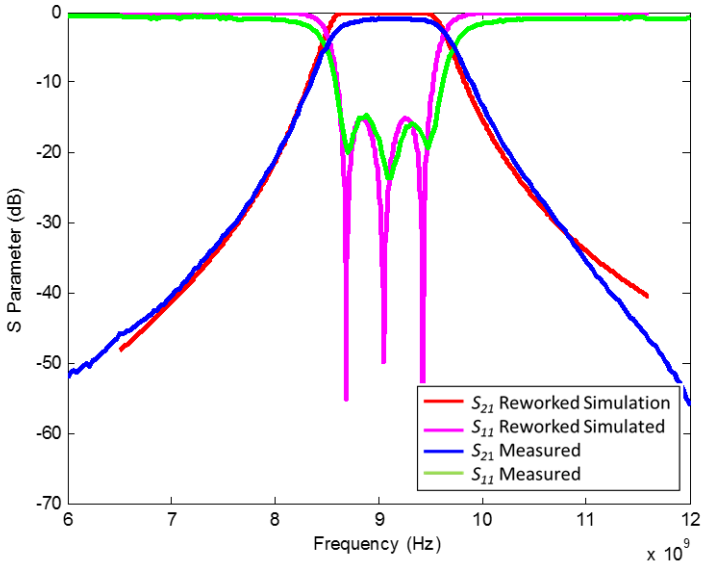

Figure 5.14 - Reworked simulated result with larger gaps

5.3 Waveguide Filter Design Using Coupling Matrix

The same operation in the previous section can be performed using waveguide resonators to create filter using the structure shown in Figure 5.15. The *Q*'s and *k*'s are this time set by adjusting a gap in the waveguide set by the height of some conducting irises marked d_1 and d_4 for the external couplings, and d_2 and d_3 for the internal couplings. The *d* values are the gaps between the waveguide and the top is the irises.

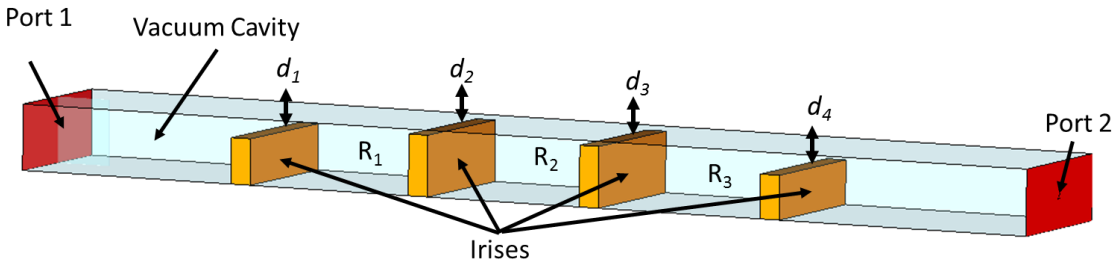

Figure 5.15 - Setup for waveguide filter

The first task is to profile the external coupling by varying the iris gap d_1. This is done using the setup show in Figure 5.16 where the left most iris is weakly coupled so the Q of the iris on the right iris dominates.

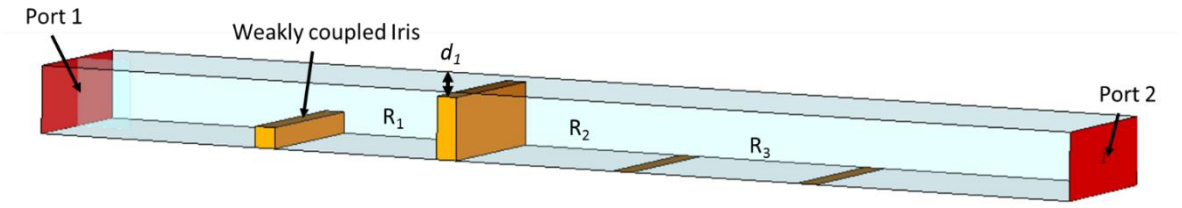

Figure 5.16 - Setup for profiling the external coupling Q

With the setup in Figure 5.16, the height of the iris was swept through a range of values and the resulting S_{21} plots are recorded in Figure 5.17. The Q of each of these plots can be calculated as shown in chapter 3, and these are plotted in Figure 5.18 which has the model adjusted for each point to account for the frequency shift shown in Figure 5.17.

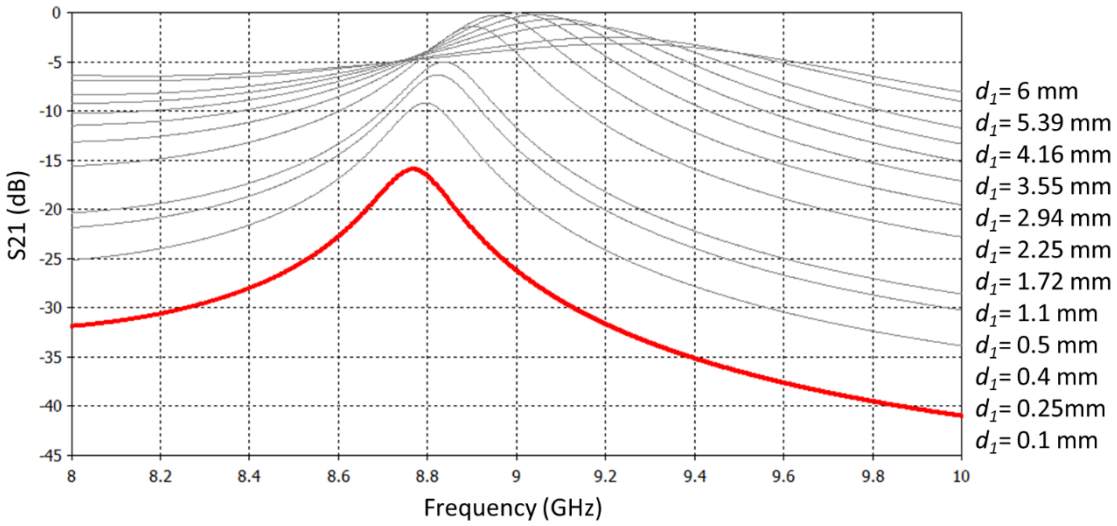

Figure 5.17 - Set of Curves obtained by sweeping iris gap d_1

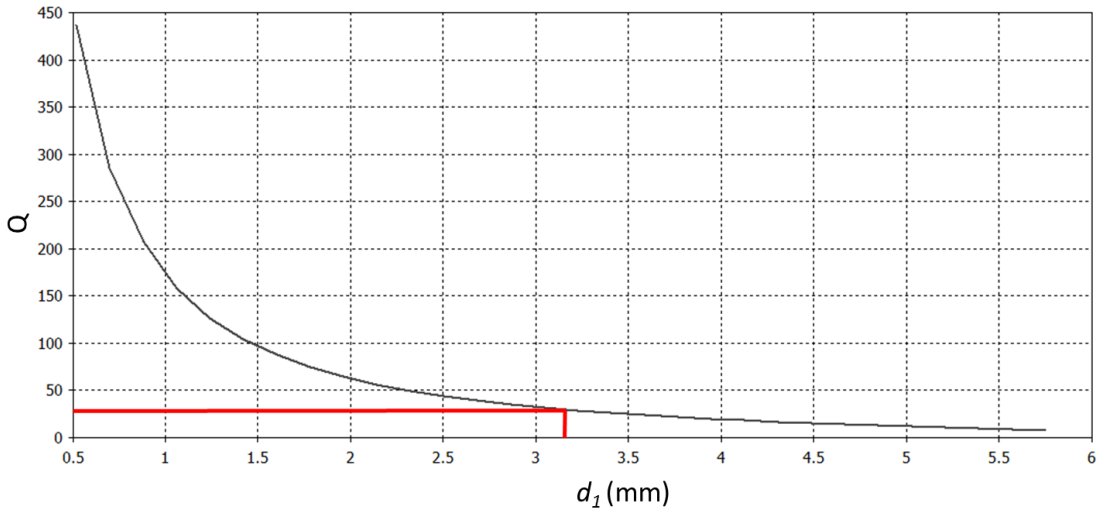

Figure 5.18 - *Q* values found from sweep of iris gap. Chosen solution marked in red.

Next the *k* values are profiled using the setup in Figure 5.19. The two irises to the left and right of the middle iris should be set to the distances which gives the sharpest double peaks for ease of measurement.

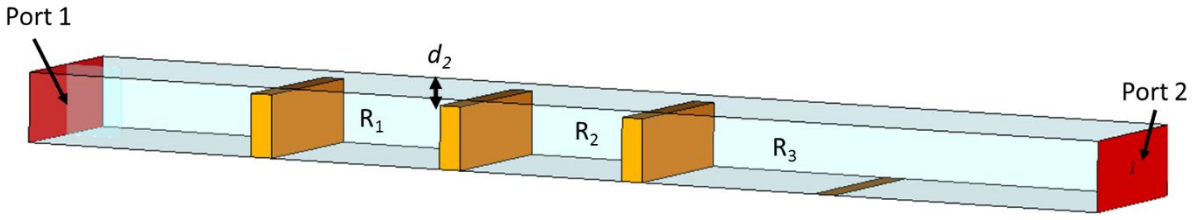

Figure 5.19 - Setup for profiling the internal k coupling

The *k* gap is then swept and the resultant peaks are shown in Figure 5.20.

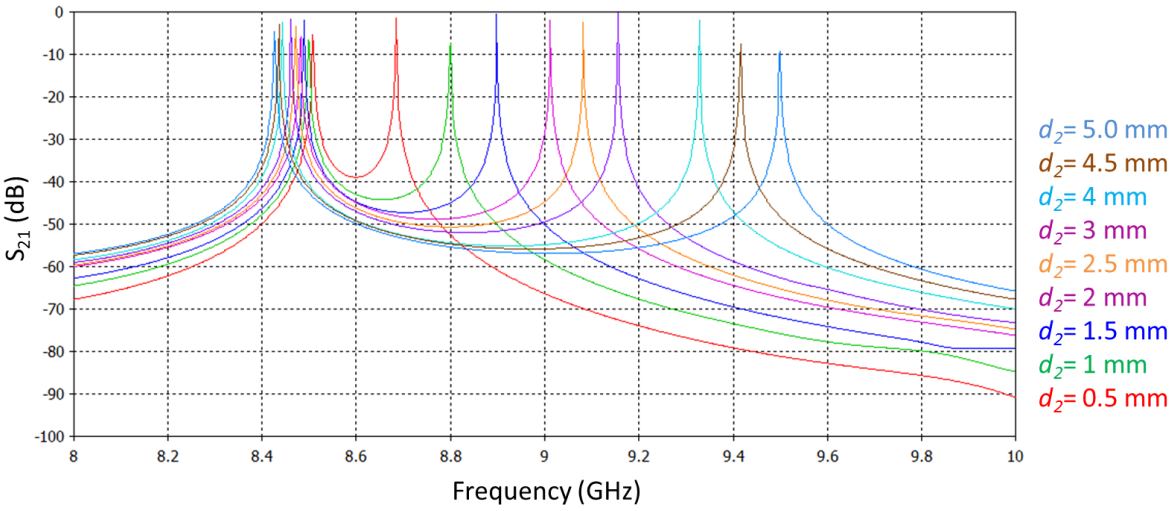

Figure 5.20 - Two peak curves generated by sweeping iris gap *k*

The *k* values can then be calculated from these peaks, and the resultant profile is shown in Figure 5.21, which again has the model adjusted by a fraction of a mm at each point to account for any frequency shift.

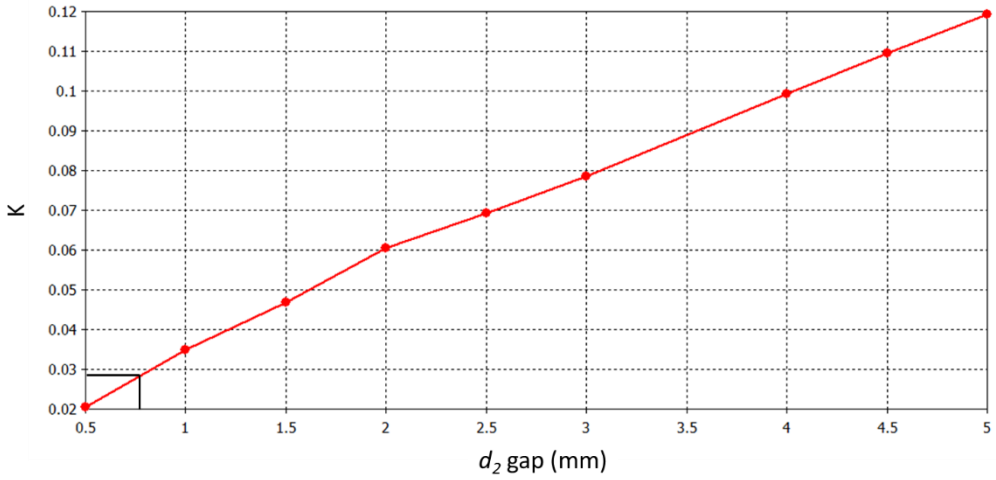

Figure 5.21 - *k* profile from sweeping internal coupling gap. Chosen solution marked in black.

Using the matrix *Q* and *k* values can be determined for a particular filter specification. This time a three pole, 9 GHz centre frequency filter, with a target return loss of -20 dB and bandwidth of 0.25 GHz is specified. The calculation result is shown in Figure 5.22.

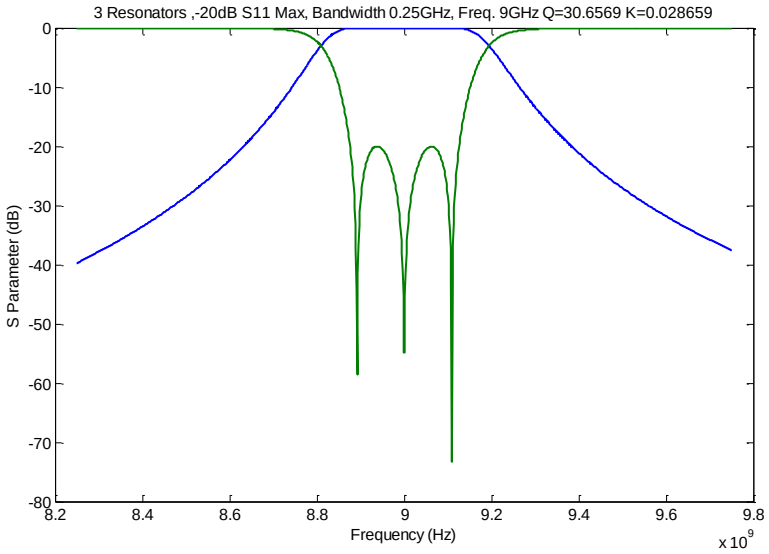

Figure 5.22 - 9 GHz filter response from coupling matrix

It can be seen that a *Q* of 30.66 and *k* of 0.0287 is required. From the profiles in Figure 5.18 and Figure 5.21, it can be determined that for a Q of 30.66 a gap of 3.2 mm is required, and for a *k* of 0.0287 a gap of 0.75 mm. The final filter configuration is shown in Figure 5.23 with the parameter settings (post optimisation) shown in table 5.3.

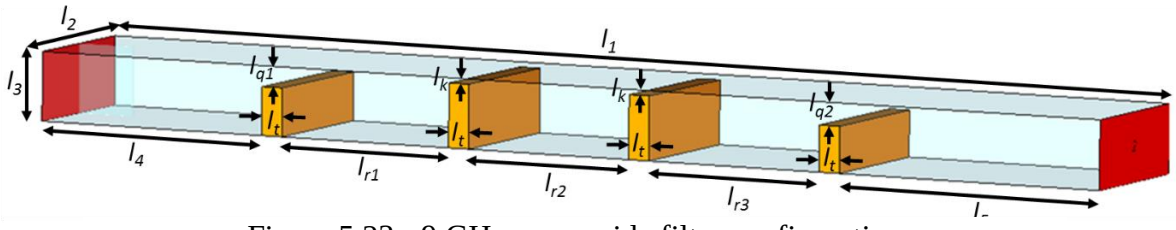

Figure 5.23 - 9 GHz waveguide filter configuration

Table 5.3 – parameter table for 9 GHz waveguide filter

Param.	Value (mm)	Post Opt, Value (mm)		Param.	Value (mm)	Post Opt, Value (mm)		Param.	Value (mm)	Post Opt, Value (mm)
l_1	175	175		l_{q1}	3.0	3.057		l_{r2}	27.0	25.744
l_2	22.86	22.86		l_{q2}	3.0	3.368		l_{r3}	27.0	27.175
l_3	10.16	10.16		l_{k1}	0.750	0.750		l_t	3.250	3.250
l_4	39.5	37.75		l_{k2}	0.750	0.770				
l_5	39.5	42.27		l_{r1}	27.0	26.984				

The ‘first attempt’, pre optimisation result is shown in Figure 5.24, which shows a very reasonable filter response that required minimal optimising. The optimised result is shown in Figure 5.25.

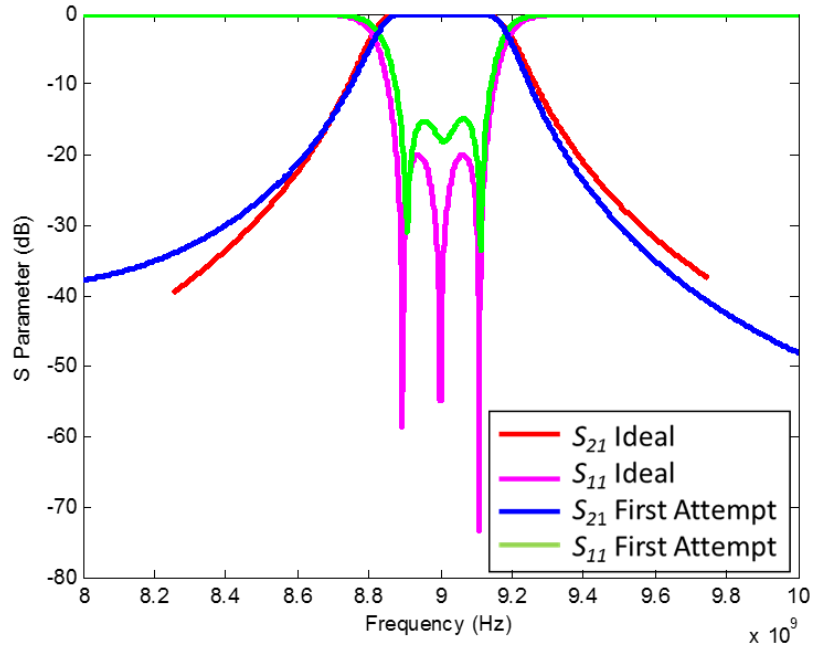

Figure 5.24 - "First attempt" filter simulation with the ideal filter response for comparison

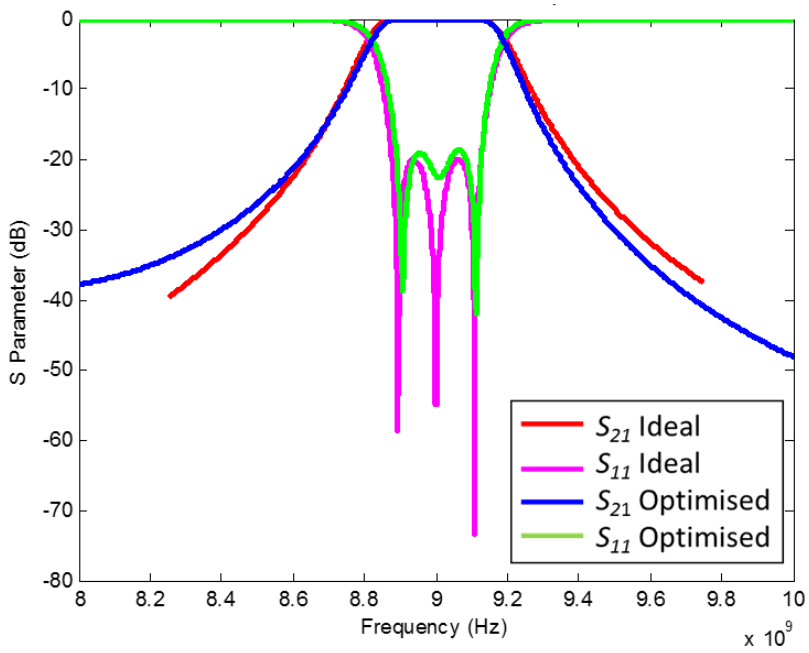

Figure 5.25 - Optimised filter simulation with ideal response for comparison

Filter gradient optimised for S_{11} goal of -20 dB at 8.875 GHz and 9.025 GHz

5.4 Conclusion

It has been shown that with coupling matrix theory that it is possible to design and fabricate filters to a specification using two different methods of implementation; microstrip and waveguide. The techniques demonstrated here are to be used in the next chapters where filters are to be integrated with active circuits.

Chapter 6

Diode Frequency Multipliers

6.1 Overview of frequency multipliers

With the desire for circuits to operate at higher and higher frequencies, the demand on local oscillators has exceeded what fundamental frequency generation can practically provide. Engineers have therefore sought to solve this issue by instead multiplying a more easily generated lower frequency to produce the required higher frequency, and the state of the art methods to do this are reviewed in Chapter 2. This chapter shows in detail that using a nonlinear device such as a diode, harmonics are generated when a pure sine wave is applied, and this situation can be exploited for frequency multiplication and carrier generation.

This thesis is concerned with the reactive diode method of frequency multiplication, in particular using the varactor diode. Varactor diodes are suited to low multiplication factor applications, such as frequency doublers or triplers, as more power is delivered into the lower harmonics. For more efficient higher harmonic reactive diode generation, the step recovery diode method is better suited. There are two other common types of harmonic multiplication methods that will be briefly mentioned; resistive diode multipliers and transistor multipliers. A discussion of the pros and cons of each type of multiplier follows.

6.1.1 Step Recovery Diode Multiplication

Step recovery diodes [2] are manufactured with the emphasis of producing very short pulses, which is ideal for producing higher orders of harmonics. The desired harmonic is then selected with a tuneable filter. These diodes are often used for very high frequency generation, however the investment in the tuneable filter, operating complexity and bulk, means this is a costly method of frequency multiplication.

6.1.2 Resistive diode Multiplication [1]

This uses a Schottky detector diode in forward bias, whose non-linear I-V response to the application of a fundamental wave generates harmonics. It can be shown from [2] that conversion efficiencies decrease as the square of the harmonic number generated, so they are limited to low multiplication applications, but have the advantage of large bandwidths. This is summarised in the equation:

$$\left|\frac{P_m}{P_1}\right| \leq \frac{1}{m^2} \qquad 6.1$$

Which shows the theoretical efficiency of a resistive diode multiplier, assuming all unwanted harmonics are terminated. P_1 is the power in the input sine wave, P_m is the power in the desired harmonic and m is the harmonic number.

6.1.3 Transistor multiplication [3].

Transistor, or active multipliers are able to provide gain to the conversion process and provide large bandwidth when compared to diode multipliers. They do however suffer from higher noise levels when compared to diode multipliers, and have the potential to perform erratically as they are conditionally stable only over a particular frequency range. They are also more costly, as well as more complex.

6.1.4 Varactor Diode Multiplication [2].

Reactive diodes are manufactured with an emphasis on providing a large variation in capacitance when the applied bias voltage is varied. One particular case of a varactor diode arrangement is the n and p regions setup shown in Figure 6.1. These regions are capable of conducting and therefore act like the plates on a capacitor. The region between them when reverse biased is in depletion and is considered as the insulating dielectric. This depletion region can be manipulated under reverse bias, and has a high capacitance from a near zero bias voltage and vice versa. It should also be noted that because reverse bias is used, no current will flow through the diode.

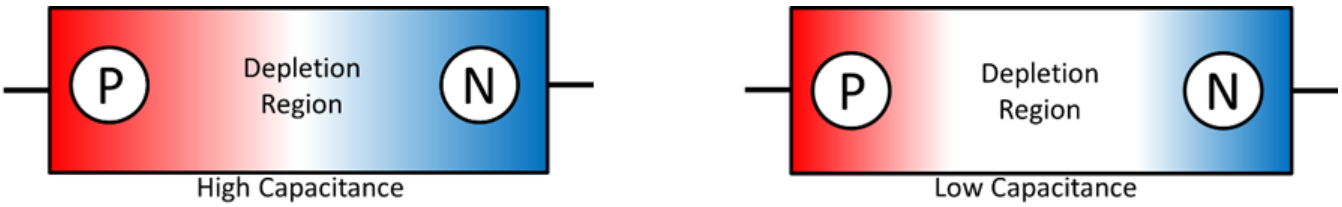

Figure 6.1- Illustration of varactor diode variable capacitance

It can be shown in [2] that the theoretical multiplication efficiency for reactive diode multipliers is 100%, as shown in the equation:

$$\sum_{n=2}^{\infty} P_{n0} = -P_{10} \tag{6.2}$$

This equation is derived from the Manley-Rowe relationship [2] which deals with the energy in a wave consisting of multiple frequencies. P_{n0} is the power in the nth harmonic and P_{10} is the source power.

If all harmonics apart from the nth is terminated with a lossless reactively matched load, equation 6.2 becomes

$$\left|\frac{P_{n0}}{P_{10}}\right| = 1 \tag{6.3}$$

This case assumes zero resistance of the diode, and that all unwanted harmonics are terminated to ground, as well as perfect reactive matching to the diode. In reality the diode will have some resistive loss and not be able to fully terminate all harmonics. Also, it is often required to confine the input signal with a filter and the desired output harmonic with an output filter, which adds matching complexity and increases potential for conversion losses.

6.2 Diode frequency cut-off

The multiplier's bandwidth is limited by the diode's own cut-off frequency. This can be determined by examining the series resistance of the diode, its dynamic junction capacitance and then using the equation:

$$f_c = \frac{1}{2\pi R_s C_j} \tag{6.4}$$

Where R_s is the series resistance and C_j the junction capacitance as shown in Figure 6.2. It can be seen from this why resistive diode multipliers have a much larger potential bandwidth compared to varactor diode multipliers as their capacitive element is much smaller.

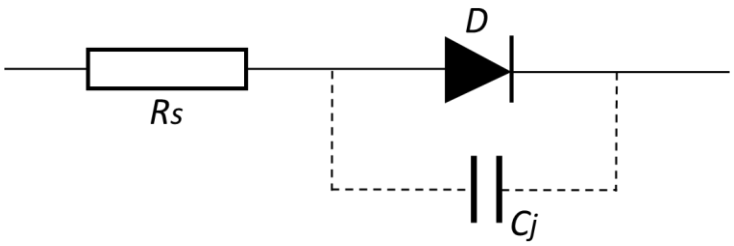

Figure 6.2 - Diode equivalent Circuit

6.3 Harmonic generation and bias determination

As mentioned in this chapter's introduction, the fundamental property being exploited to produce higher frequency harmonics is the nonlinear nature of a device. In the case of the varactor, the nonlinear capacitance versus applied signal voltage is exploited; a variation in capacitance due to the applied voltage will give rise to a non-linearity in the differential equations for the voltage and current. This leads to the generation of harmonics. To illustrate this further the capacitance versus bias voltage graph of a Macom [4] MA46H200 varactor diode is shown in Figure 6.3.

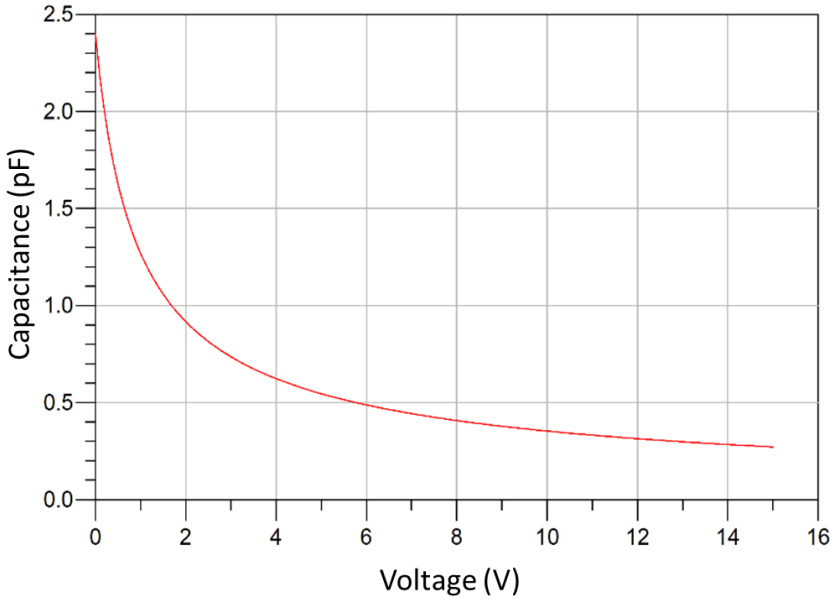

Figure 6.3 - C-V Curve for the Macom [4] MA46H200
Varactor diode

The curve in Figure 6.3 is extracted from an Advanced Design System [5] diode model created from data given by the diode manufacturer. The diode model used is shown in the equivalent circuit in Figure 6.4. Where C_{dj} is the linear junction capacitance, i_d is the dc current

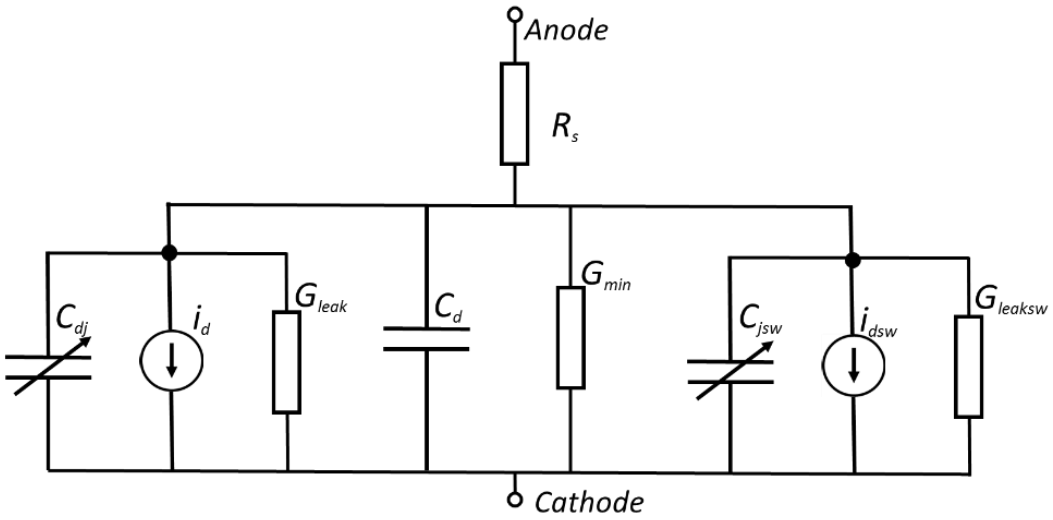

Figure 6.4 Varactor diode equivalent circuit model

G_{leak} is the junction leakage conductance, c_d is the linear capacitance, G_{min} is the minimum junction conductance, C_{jsw} is the Sidewall zero-bias capacitance, G_{leaksw} is the Sidewall junction leakage conductance and R_s is the series resistance, as detailed in the designer help notes for Agilent's Advanced Design System circuit simulator [5]. The values used for these parameters are the simulations defaults of zero, unless otherwise stated in Table 7.1.

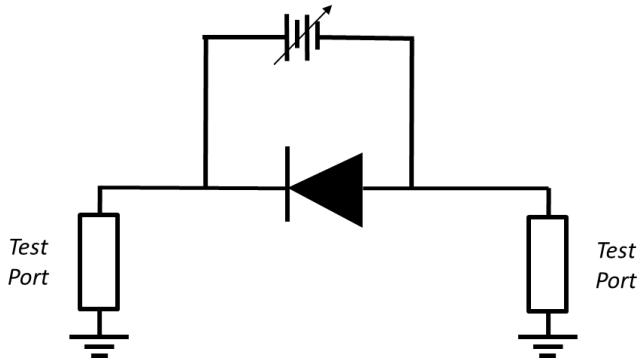

Figure 6.5 - S parameter test bench with bias sweep

The procedure to obtain the curve requires a simulation to sweep the bias voltage applied to the diode in Figure 6.5, and record the S parameter at each point.

The impedance *z* can be calculated using equation:

$$z = 50\left[(1 + S_{11})(1 + S_{22}) - \frac{S_{12}S_{21}}{2(S_{21})}\right] \quad 6.5$$

And then the capacitance can be simply derived from the imaginary component of *z*, depending on required frequency.

It is also possible to construct the curve from the datasheet [6] using the equation:

$$C = \frac{C_{jo}}{(1+\frac{V}{V_o})^n} \qquad 6.6$$

where C_{jo} is the zero bias junction capacitance, V is the bias voltage, V_o is the junction potential with zero bias and n is a value dependent on the diode doping profile.

This gives the graph in Figure 6.6 (which includes the previous simulated CV curve from Figure 6.3), with a 2.4 pF junction capacitance, a 0.65 V zero bias junction voltage and a doping profile n of 1.08, which are the same parameters as the commercial diode in Figure 6.3.

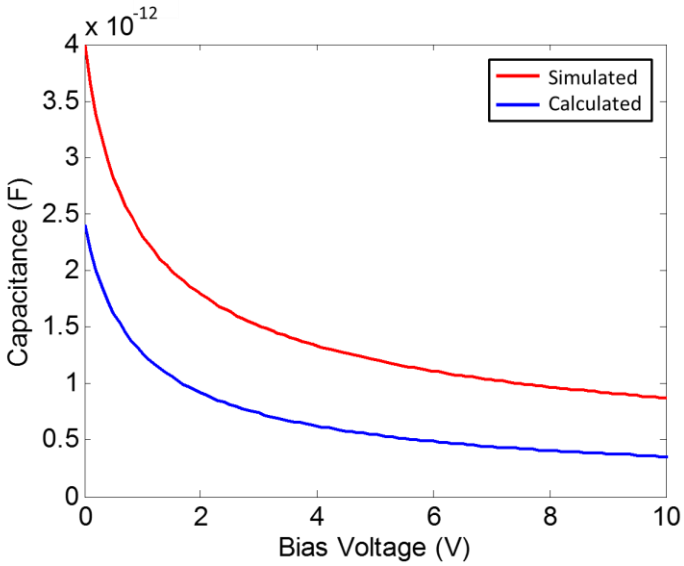

Figure 6.6 - Diode CV curve comparison of simulated device with calculation

While the plots are not in complete agreement, they are similar and the differences are anticipated when using the simplified equation 6.6 versus a circuit simulation extraction method. It can be seen that if the diode is biased at some point on this curve, and a pure sinusoidal signal is applied, that the resultant capacitance will vary in a non linear way, as illustrated in Figure 6.7.

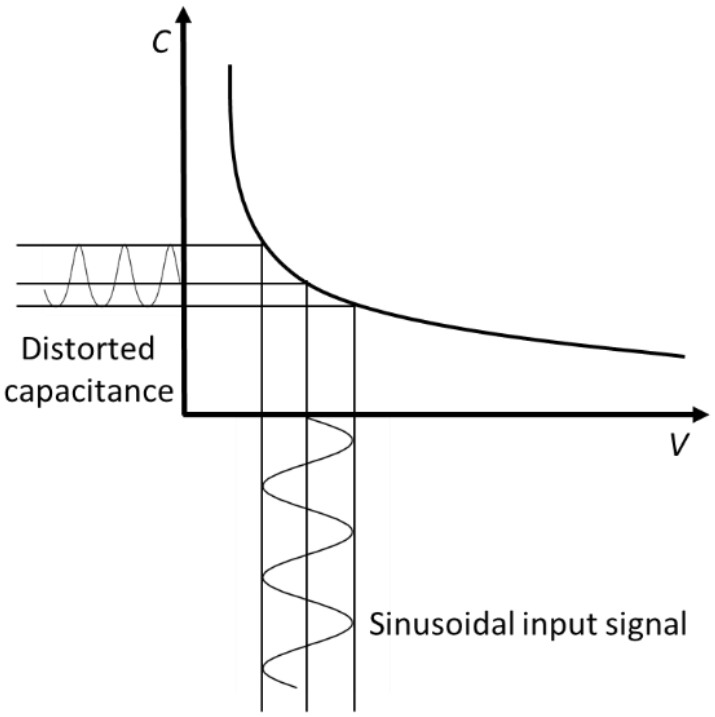

Figure 6.7 - Illustration of distortion of pure sine wave when applied to a reverse biased nonlinear varactor diode

This nonlinear variance will lead to the generation of harmonics, and the associated mathematics is dealt with in [2]. This details the Manley-Rowe relations and how they can be used to analyse power associated with frequency conversion in nonlinear devices.

6.4 The effect of package parasitics on diode performance

One important aspect to consider when designing diode doublers is the effect of circuit and package inductances and capacitances. Figure 6.8 shows the model for a diode D, with the unwanted parasitic package inductance L and capacitance C.

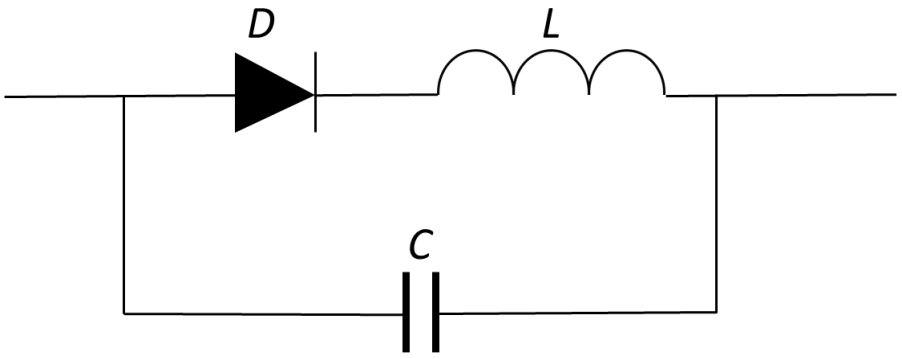

Figure 6.8 - Diode Circuit showing package parasitics C and L

The effect of typical values of L and C on the CV curve are considerable. Figure 6.9 shows two CV curves for a diode with and without package parasitics (L= 0.45nH, C= 0.15pF).

It is therefore clear how important it is to model the parasitics of the diode and package correctly to obtain a reliable result.

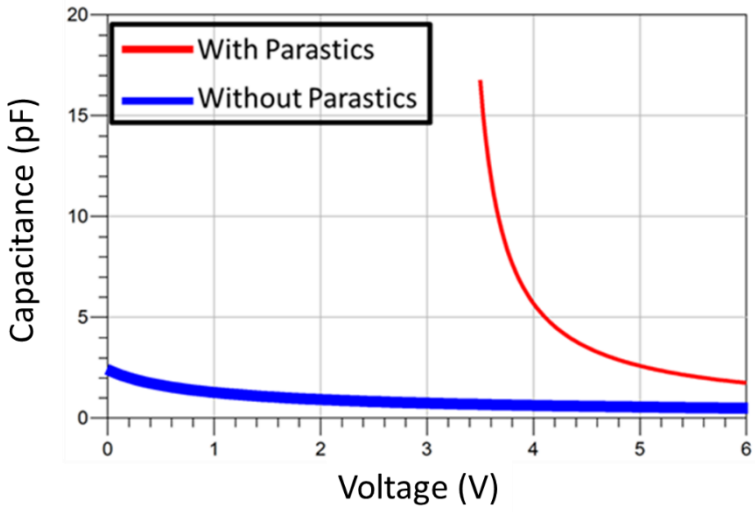

Figure 6.9 - Comparison of CV curve for diode with and without parasitics

6.5 Matching and Doubling Efficiency

The efficiency of a diode doubler circuit is defined as the ratio of the fundamental input power P_{in}, to the power of the second harmonic at the output P_{out}:

$$Efficiency\ (\%) = \frac{P_{in}}{P_{out}} \times 100 \qquad 6.7$$

One major factor when determining the conversion efficiency of a frequency doubler is the impedance matching of the diode to the external circuit. The matching of power to a frequency doubling diode is complex due to the requirement to match across a bandwidth and also at different frequency bands, for example for a diode frequency doubling circuit to double a 9 GHz fundamental to 18 GHz over a 1 GHz bandwidth will require matching from 8.5 GHz to 9.5 GHz at the input and 17 GHz to 19 GHz at the output. The diode impedance is best obtained by

measurement and if a suitable diode model exists then this can be done in a simulator, for example [5], using a setup shown in Figure 6.10.

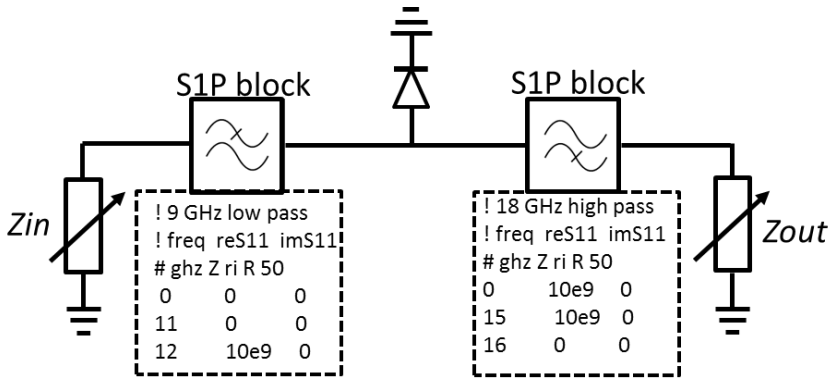

Figure 6.10 - Circuit setup to determine optimum input and output impedance for the diode. S1P block code for low and high pass filters shown.

The circuit in Figure 6.10 is used to determine the ideal matching impedances to the diode for the fundamental frequency, *Zin*, and also the ideal matching impedance for the second harmonic *Zout*. The S1P simulation blocks are needed to decouple the fundamental frequency from the output port and the second harmonic from the input port. The S1P blocks are required to

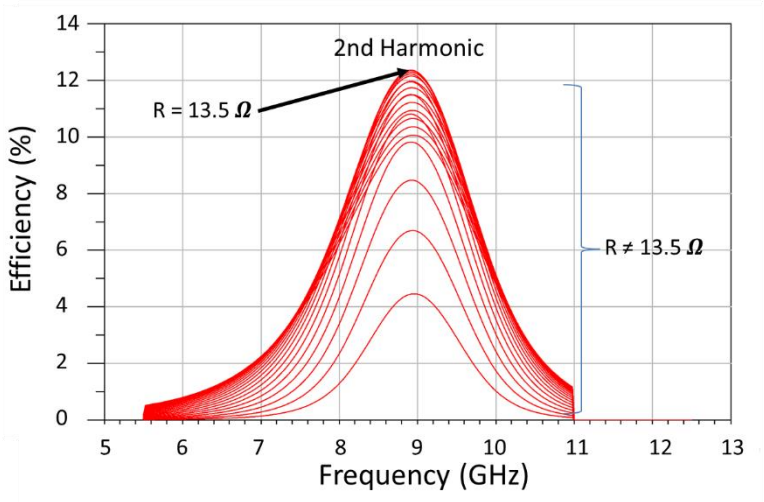

Figure 6.11 – Efficiency plot for input impedance sweep (real part). Diode biased at -4.4V.

have zero impedance over the pass band because the optimised *Zin* and *Zout* are the only relevant impedances to give the maximum circuit doubling efficiency. The S1P block at the input therefore acts as a perfect low pass filter cutting off somewhere between the fundamental and the second harmonic frequencies, and the S1P block at the output is a perfect high pass filter cutting off at the same frequency. After *Zin* and *Zout* are put through a sweep or optimisation process to obtain the greatest doubling efficiency, then the diode impedance at the fundamental will therefore be the conjugate of *Zin*, and the diode impedance at the second harmonic will be the conjugate of *Zout*. An example of an output of a parameter sweep of just the real part of *Zin* is shown in Figure 6.11.

Figure 6.12 shows a sweep of the reactive part of *Zin* which as well affecting the efficiency can also be seen altering the frequency of the second harmonic.

It can be seen that there is an optimum input and output impedance which are seen at the peak doubling efficiency at the desired centre frequency. As this is a simulation to determine the optimum efficiency, it is desirable to do an extra check to determine that the correct and only

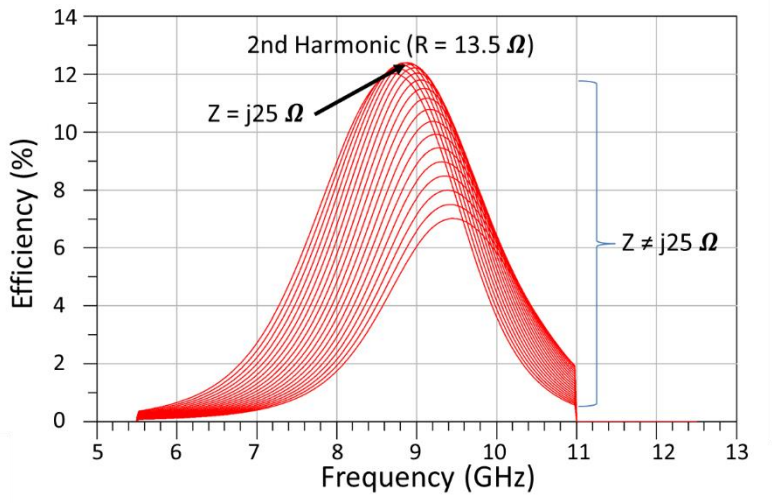

Figure 6.12 – Efficiency plot of input impedance sweep (imaginary part). Diode biased at -4.4V

peak efficiency has been found by this impedance optimisation. A technique that allows us to do this is the load pull [7]. The load pull is usually used in amplifier design to achieve a similar result of determining where the peak amplification efficiency is for all load conditions. The load impedance is swept through all values and the efficiency for each value setting is recorded. The data can then be plotted, ideally on a Smith chart, and efficiency contours can be examined.

The simulation setup in Figure 6.10 was used again, but instead of letting the optimiser adjust the impedance values at the input and output, this time the simulator was swept through all values of impedance, recording the efficiency at each step. However, unlike an amplifier load pull, there are two sets of impedance to vary (the input / source and output / load) so it is necessary to measure each in turn. This is also because a diode is non-unilateral and the input affects the output of the circuit. Therefore, the load pull was done by fixing the source impedance at the optimised values and varying the load impedance, measuring the efficiency at each step, as shown in Figure 6.13.

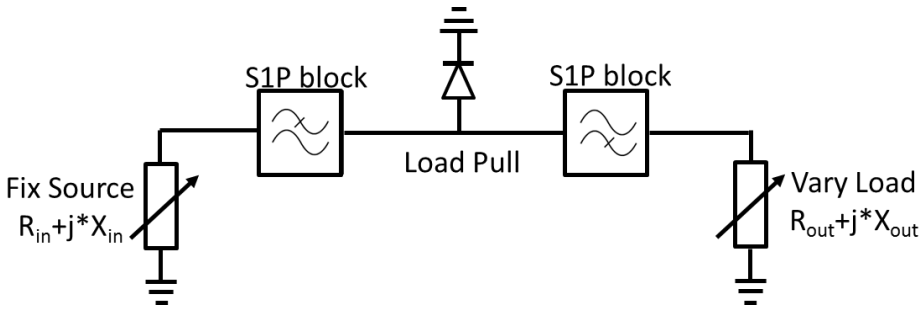

Figure 6.13 – Circuit for diode load pull

The source pull is the reverse of this, with the load impedance fixed at the optimised values and the source impedance varied, measuring the efficiency at each point, as shown in Figure 6.14.

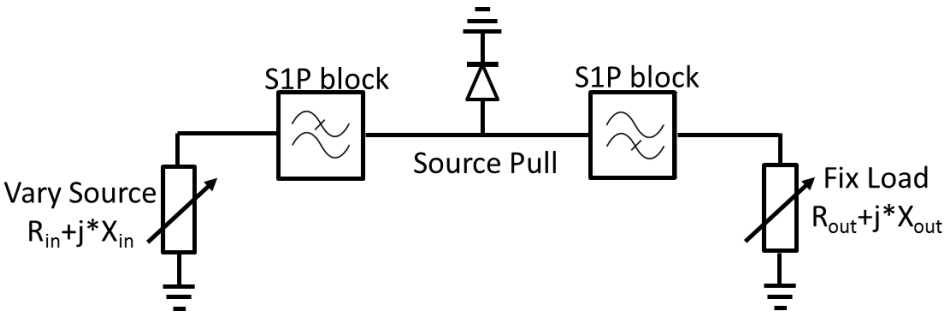

Figure 6.14 – Circuit for diode source pull

The resultant efficiency is plotted on a Smith chart, and the plot shown in Figure 6.15 is from the efficiency circuit in Figure 6.10. Figure 6.15 shows the efficiency contours for a fixed source impedance of $Z = 9+j10$, and a varying of the load impedance.

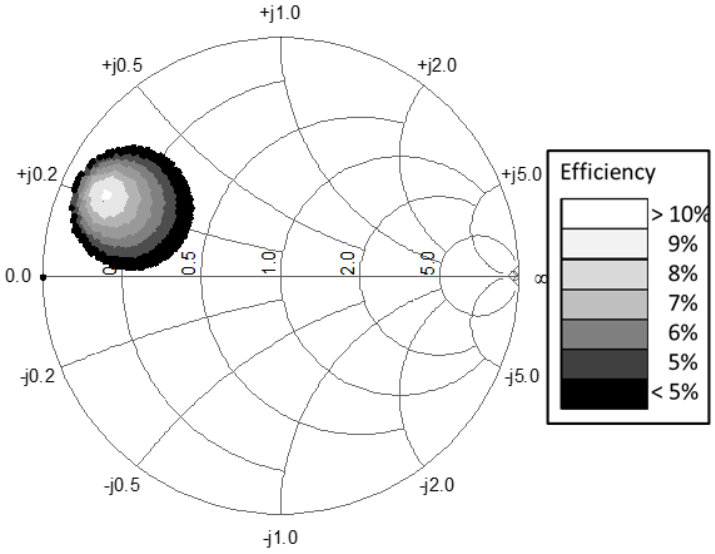

Figure 6.15 - Load pull efficiency contours.

6.6 Doubler Design by optimiser

This section details an exercise to see what results can be obtained by designing a diode frequency doubler using a circuit simulator to determine the lengths of tracks and gap spacing of the circuit using an optimisation routine targeting maximum power output of the doubled second harmonic.

6.6.1 The Diode doubler design and results

For the diode doubler circuit, a model was created with a simple coupled line filter and matching stubs. The lengths of the coupled line filters were initially set to half wavelength (at 9 GHz for the input and 18 GHz for the output) and the matching stubs set to half wavelength also. The diode used was again the MACOM MA46H200 with the CV curve given in Figure 6.3 All track lengths and widths were parameterised and an optimisation routine set up to adjust everything until a maximum doubling efficiency was obtained.

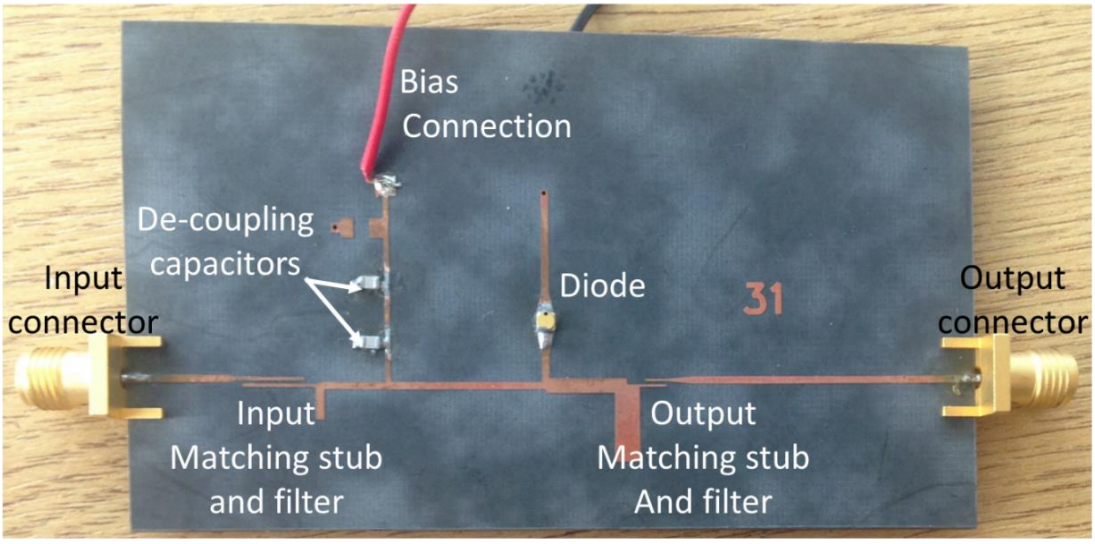

Figure 6.16 - Photograph of design by optimiser diode frequency doubler

The circuit was then built and a photograph and layout of this ‘designed by optimisation’ circuit can be seen in Figure 6.16 and Figure 6.17. The substrate used was Rogers [8] 5870 duroid, 0.254mm thick, 9 µm copper thickness, with a dielectric constant of 2.33 and decoupling capacitor values used are 1nF and 10nF 0604 surface mount footprint.

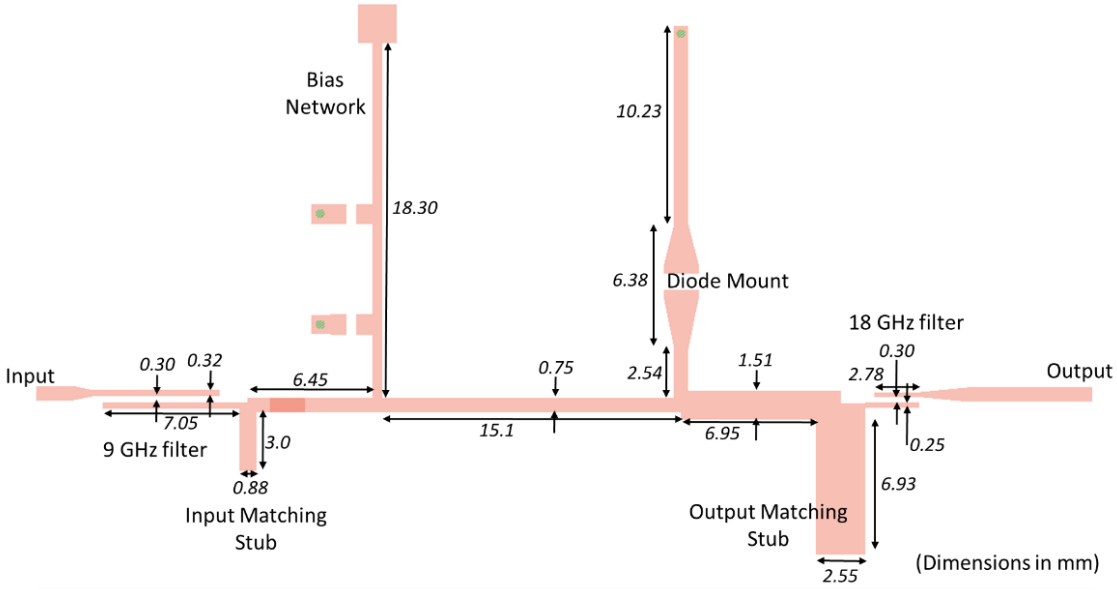

Figure 6.17 - Layout of design by optimiser diode frequency doubler

The circuit comprises of a simple 9 GHz coupled line bandpass filter to isolate the generated harmonics from the input, while allowing the fundamental to pass. A similar coupled line bandpass filter at 18 GHz is also included to isolate the fundamental input signal from the output, but to allow the generated second harmonic to pass. Input and output matching stubs are included to transform the impedance of the coupled lines to match that of the diode. The optimisation for the circuit adjusts the lengths and widths of coupled line resonators and gaps, as well as the lengths of the matching stubs and mounting tracks for the diode.

The results of this design method are shown in Figure 6.18 and Figure 6.19. It can be seen that an output band that has been optimised for a peak doubling power over a bandwidth of 1 GHz. The measured doubling efficiency is around 1.5%, which is less than the simulated 2.25% efficiency. It can be seen in Figure 6.18 and Figure 6.19 that there is a frequency shift which is due to fabrication errors of the micro strip circuit (the manufactured dimensions were measured to be fractionally smaller that required), causing a frequency shift and a detuning of the circuit and hence a drop in efficiency due to compounding incorrect coupling and matching values. To determine the frequency doubling efficiency, a fundamental frequency is generated at the input of the circuit and the doubled frequency is measured at the output. The frequency is swept across a range of values which will generate a doubled frequency band at the output.

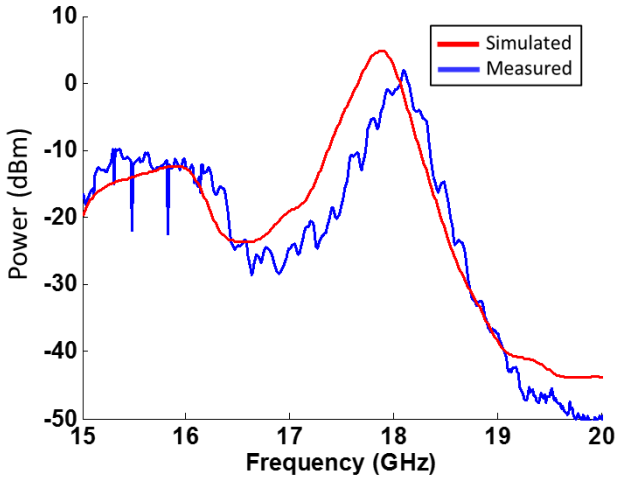

Figure 6.18 - Output band of second harmonic doubled frequency
(Input power = +16dBm, diode bias -4.4V)

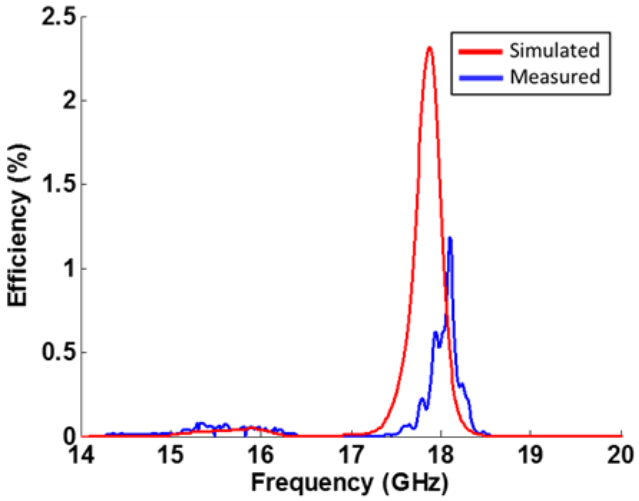

Figure 6.19 - Design by optimiser diode frequency doubler efficiency plot

6.7 Conclusion

The theory and criteria to be considered when choosing a frequency multiplier method have been discussed in this chapter. The design fundamentals for a varactor diode doubler have been shown, and a diode doubler design using a circuit simulation optimiser has been briefly presented. The measured doubling efficiency of 1.5% and resultant band shape are shown in the next chapter to be an inferior result compared to a more controlled design approach, and compares poorly with commercial and state of the art circuits which have conversion efficiencies of 30% or more. This further highlights that an informed and structured design process is required and that a brute force optimisation approach yields poor results.

The information from this chapter, along with the design techniques for coupling matrix filters can now be combined to design a diode doubler circuit, which shall be shown in the next chapter.

References

[1] F. Giannini and G. Leuzzi. **Nonlinear Microwave Circuit Design.** John Wiley and Sons, 2004.

[2] Pozar, D.M.. **Microwave Engineering**. John Wiley & Sons, 2005.

[3] Marek T Faber, Jerzy Chramiec, Miroslaw Adamski. **Microwave and Millimeter-Wave Diode Frequency Multipliers.** Artech House, 2001.

[4] MACOM Technology Solutions Inc

[5] Agilent Advanced Design System[tm]. Keysight Technologies. http://www.keysight.com/

[6] Stauffer, George. **Finding the Lumped Element Varactor Diode Model**. High frequency electronics, 2003. Pages 22-28.

[7] Arvind Raghavan, Nuttapog Srirattana, Joy Laskar. **Modelling and Design Techniques for RF power amplifiers**. Wiley Press, 2007.

[8] Rogers Corporation. http://www.rogerscorp.com/

Chapter 7

The Shared Resonator Frequency Doubler

7.1. Introduction

The traditional method for designing diode frequency doublers is to construct a circuit simulation using a blend of theory and experience, and then evoking an optimisation process to find an acceptable compromise of circuit responses. This chapter provides an alternative approach when initiating the design of such circuits, to find a solution to the problem of designing diode frequency doublers without a heavy reliance on experience and optimisation. It provides a method that allows the circuit to be analysed and understood throughout the design process and uses optimisation to fine tune the final solution, rather than to seek a set of working parameters using processor power, patience and luck. An additional advantage of the method demonstrated in this chapter, is that by removing the reliance on optimisation, circuit complexity can be scaled up and design innovation is increased. By finding integrated solutions combining passive and active circuits, some traditional circuit elements can be removed, such as impedance transformation structures and redundant resonators, which enables space and material savings. This method also allows the design of integrated coupled connections to other circuit elements, allowing a total integrated and controlled design.

7.1.1 Chapter Structure

This chapter details the design, manufacture, testing and discussion of the results of a microstrip diode frequency doubler. The coupling matrix method outlined in chapter 3, is used to integrate two bandpass filters into the diode doubler circuit. The first filter is used as an input bandpass filter to allow the fundamental frequency to pass, but to exclude the second and higher harmonics from coupling back to the input. The second filter is an output bandpass filter, whose purpose is to allow the doubled frequency to pass but prevent the fundamental and higher harmonics coupling to the output. The diode is mounted on a microstrip track that is used as a shared resonator for both filters. The benefit of this is to reduce circuit size and lower cost and manufacturing complexity. This chapter also demonstrates the versatility of the coupling matrix method to allow the construction of integrated passive and active circuits without a heavy reliance on circuit optimisation.

The first section of this chapter explains the design concept of the diode frequency doubler. The next section defines the diode characteristics and determines some of the settings to be used in the design, such as bias, input power and target frequency doubling efficiency, substrate choice and operating frequency. Because of the complexity of some of the circuit interactions, the next section contains a summary of the problems to be solved with the chosen diode doubler circuit structure, and outlines the solution which is dealt with in more detail in the next section. Next, the circuit elements being analysed are defined, and the design process explained, including results of a manufactured circuit. The last section introduces some work on how flexible the coupling matrix design approach can be for applications such as diode frequency doubler design.

7.2 Design Concept of the shared resonator diode doubler

Chapter 6 showed how a conventional frequency doubler can be crudely designed by parameterising the building blocks required (filters, matching stubs, diode circuit etc.) and running an optimisation simulation. That design is summarised in the block diagram in Figure 7.1, which shows the individual stages for the filters and the requirement for impedance transforming stubs to match the filter to the diode.

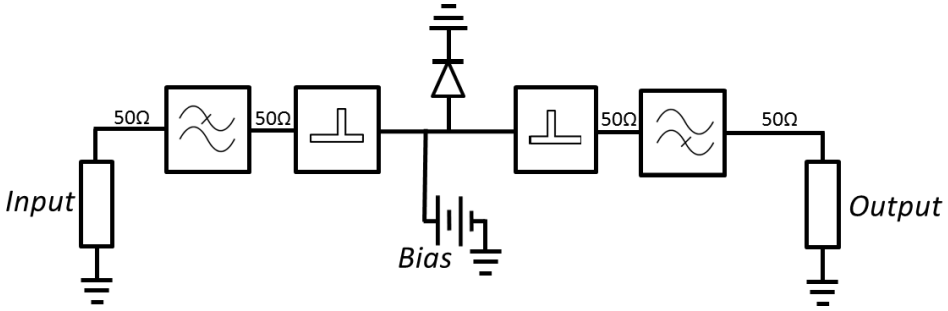

Figure 7.1 - Traditional diode doubler circuit block diagram

The impedance transforming stubs are required because a filter designed using conventional methods results in unmatched impedances between the filter and the diode. Usually the bandpass filter design techniques will create a symmetrical circuit with 50 Ω input and output impedances, and the matching impedance of the diode shown in chapter 6 shows it differs from 50 Ω.

However, in this chapter a design procedure is proposed for a structure that includes filters that sharply define a band of operation of the doubler circuit, which are integrated with the active part of the circuit, and match the impedance with no requirement for impedance transformation stages. The proposed structure is shown in Figure 7.2, with a summary of the resonator and couplings shown in Figure 7.3. Its design procedure is contained in the rest of this chapter.

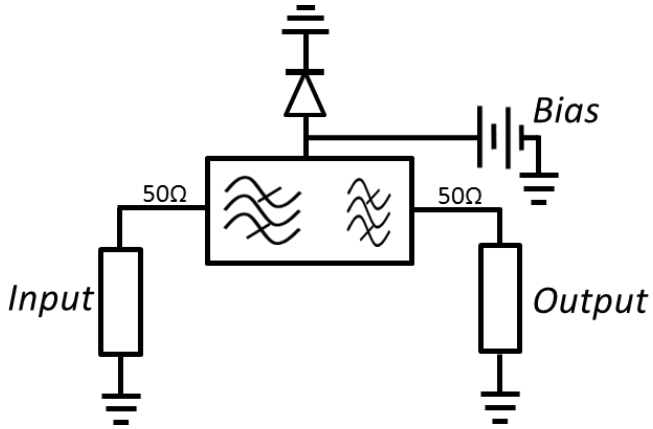

Figure 7.2 - Proposed integrated diode doubler design

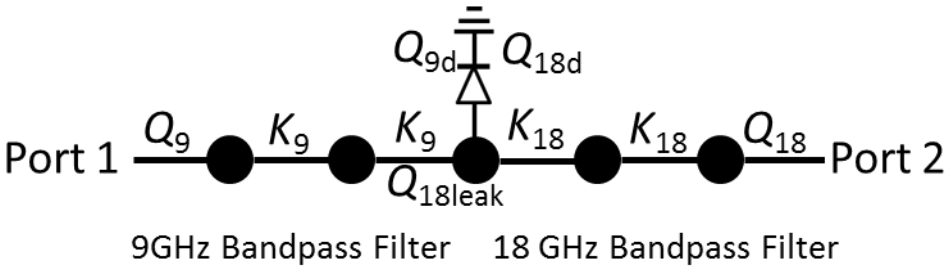

Figure 7.3 - Summary of resonators and couplings in the proposed diode doubler and filter structure

The couplings Q_9, K_9, K_{18} and Q_{18} are profiled using the same method as for to the filter analysis couplings in Chapters 3 and 5. The coupling Q_{9d} is the external coupling to the diode at 9 GHz and we require a situation where Q_{9d} is equal to Q_9 for our filter design to work. The value of this will be dependent on the diodes parameters and also bias, and is explained in more detail later in this chapter. The coupling Q_{18d} is the external coupling at 18 GHz into the diode and Q_{18leak} is the unwanted external coupling back through the 9 GHz filter to the input. The coupling Q_{18} will therefore be given by:

$$\frac{1}{Q_{18}} = \frac{1}{Q_{18d}} + \frac{1}{Q_{18leak}} \qquad 7.1$$

It will be shown later in this chapter that Q_{18leak} can be minimised to allow most of the doubled frequency energy to couple to the output, rather than back to the input.

7.3 Frequency of operation and substrate choice

The circuit is to be designed for an input frequency of 9 GHz, which when doubled will give a second harmonic output frequency of 18 GHz. The operating frequencies 9 GHz and 18 GHz were decided to be the best highest frequencies for use with microstrip after considering the information discussed in Chapter 3. It can be seen from that section 3.5 that higher frequencies could be used, however due to the physical size of the resonators and gap spacing, 9 / 18 GHz was deemed a practical frequency to design a diode doubler for manufacturing ease but to also demonstrate the coupling matrix integration theory adequately. It is also easier at lower frequencies to observe circuit and design traits more accurately. The substrate used was Rogers [1] 5870 duroid, 0.254mm thick, 9 µm copper thickness, with a dielectric constant of 2.33 and a dielectric loss tangent of 0.0012 at the frequencies we are simulating. The substrate model is shown in Figure 7.4. The model used is not enclosed in a box and is considered open.

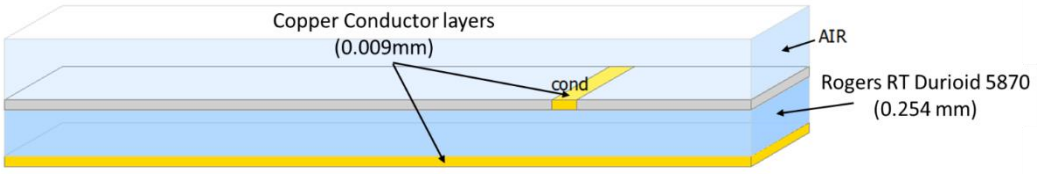

Figure 7.4 - Diode doubler substrate model

7.4 Diode Model

The diode chosen for the doubler design is the Macom [2] MA46H200 surface mount varactor diode, shown in Figure 7.5.

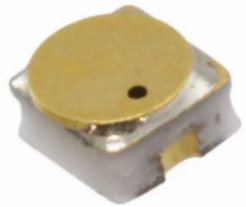

Figure 7.5 - Photograph of MACOM MA46H200 diode. Taken from [2]

This diode was chosen due to its low cost, and low junction capacitance. As stated in Chapter 6, varactor diodes have a relatively narrow bandwidth compared to most other doubling methods, so to capitalise on this feature a frequency doubler with a band of about a gigahertz with a sharp drop off shaped by the filters is produced. This will have advantage in applications where unwanted signals require a high rejection, which is ideal in a chain of frequency multipliers where unwanted harmonics from previous stages could cause unwanted mixing products that require high rejection.

The diode's parameters are taken from the manufacturer's data sheet [2] and entered into a model in Agilent's Advanced Design System simulator [3], and a circuit constructed to include the effect of the package parasitics (values taken from datasheet). The model of the diode is shown in Figure 7.6, and the diode parameters used are listed in table 7.1.

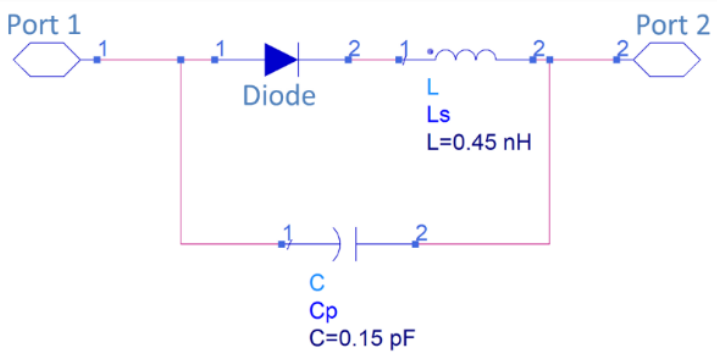

Figure 7.6 - Model of the diode including package parasitics

Table 7.1 – Diode model parameters

Diode Parameter	Value	unit
Is, Saturation current	5×10^{-8}	A
Rs, Ohmic Resistance	6	Ohm
N, Emission coefficient	1.08	-
Cjo, Zero bias junction capacitance	2.4	pF
Vj, Junction potential	0.65	V
M, grading Coefficient	0.685	-
Bv, Reverse breakdown voltage	12.72	V
Ibv, Current at reverse breakdown voltage	1×10^{-5}	A
Xti, Saturation current temperature exponent	2	-
Eg, Energy Gap	0.69	eV

7.4.1 Diode Bias Arrangement

The diode bias arrangement is shown in Figure 7.7, which shows a variable voltage source connected via a dc feed / RF choke to the diode model of Figure 7.6 and the rest of the circuit.

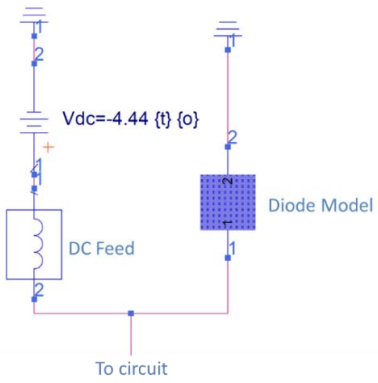

Figure 7.7 - Simulator diode bias arrangement

7.4.2 Optimum Doubling Efficiency of the MA46H200 diode

A method to determine the optimum doubling efficiency of a diode was introduced in chapter 6. This method used a simulation to optimise the input and output impedance applied to the diode in a circuit with S1P blocks to act as perfect low and high pass filters, as shown in Figure 7.8.

The S1P blocks are simulator components that allow the user to enter their own S parameters to suit their purposes, even if the values entered are not physically realisable. This is useful in this situation as we require perfect filters that have no effect on the impedance seen by the diode at the input and output of the circuit.

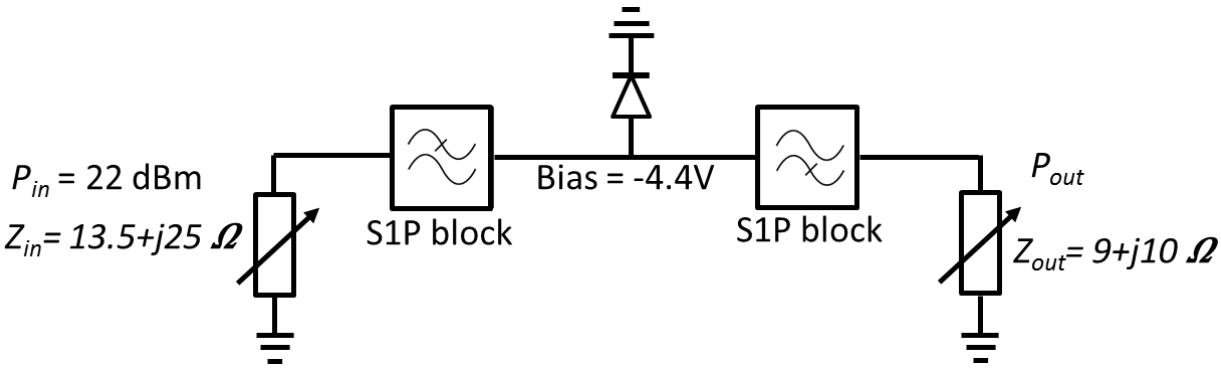

Figure 7.8 - Idealised circuit to determine optimum parameters

Figure 7.8 also shows the resultant optimised impedances, input power and bias determined using this method. The doubling efficiency of this ideal circuit is plotted in Figure 7.9. The efficiency is calculated from ratio of the second harmonic output power P_{out} to the input power $P_{in.}$

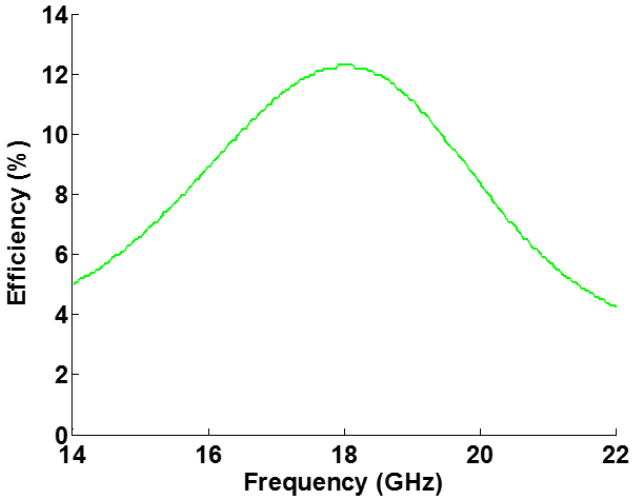

Figure 7.9 - Plot of optimum diode doubling efficiency of an ideal circuit (diode package parasitics included in model)

It can therefore be seen that under ideal conditions, that a doubling efficiency of around 12% can be expected with the diode model used (diode package parasitics included). While this

result is obtained with practically unachievable conditions, such as using filters that do not affect the impedance seen by the diode to the input and output, and a perfect input and output match, with no other circuit losses, it is a guide to compare the results of the following design process.

7.5 The Shared Resonator Diode Doubler design

This section contains the design method of the microstrip shared resonator varactor diode doubler. While each stage of the design uses knowledge from previous chapters of this thesis, the final implementation is complicated due to overlapping circuit elements between the input and output filters. Therefore an extra introduction to this section is included, that highlights the problems to be solved and summarises the design process used to solve them. The proceeding sections will contain the detail of this process.

7.5.1. Introduction to the problem of complex circuit interactions

The diode doubler structure to be analysed is shown in Figure 7.10. The whole structure will be defined in more detail later in this chapter, however what is illustrated in Figure 7.10 are the internal (K) and external (Q) coupling curves determined from varying the gaps d_1 to d_6. When values are selected from these curves using coupling matrix theory, an input bandpass filter at 9 GHz and an output bandpass filter at 18 GHz can be designed and will be integrated with the diode doubler circuit.

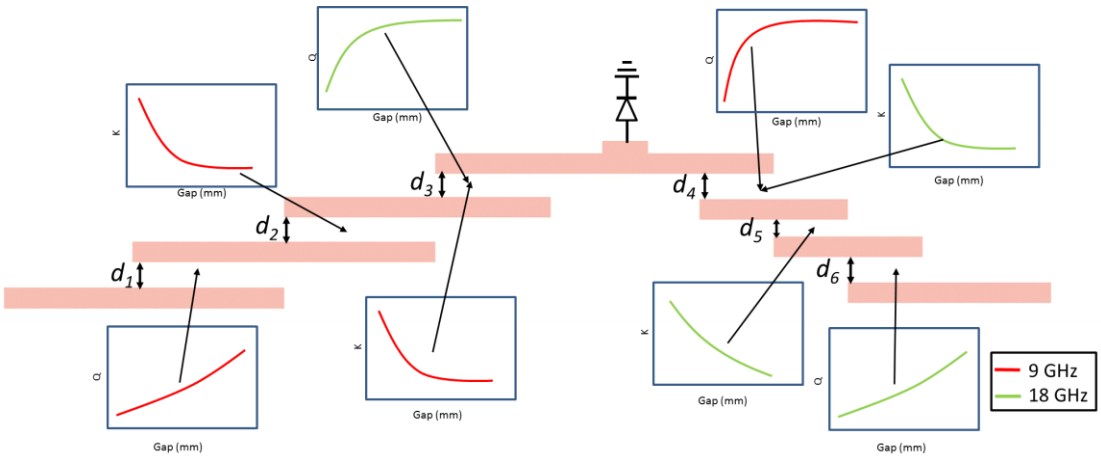

Figure 7.10 Diode doubler structure showing internal and external couplings for input and output bandpass filters.

The detail on how each curve is obtained is explained later in this chapter.

The design challenge is further illustrated in Figure 7.11, which shows that the resonator containing the diode is shared by both filters. It can also be seen that the couplings onto this resonator are also shared at the point indicated, by both filters, as there is an unwanted coupling at 18 GHz back through the 9 GHz filter to the input.

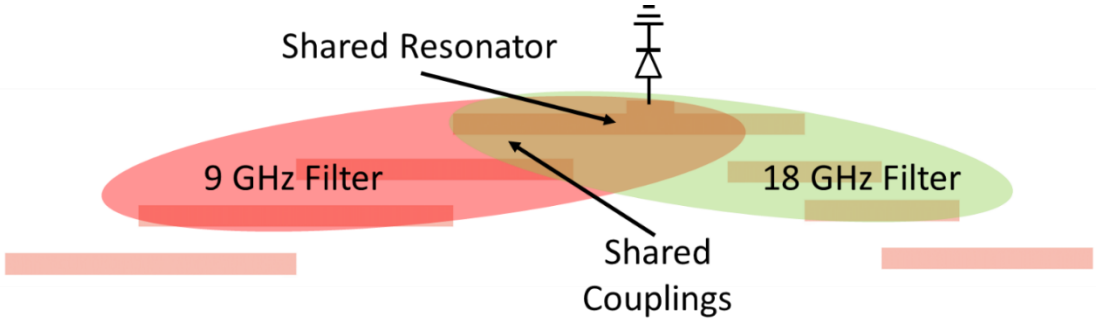

Figure 7.11 – Diode doubler structure highlighting filter positions and shared resonator and couplings.

The problem with this structure is that simultaneous filter solutions need to be found for both the 9 GHz and 18 GHz bandpass filters, that share the resonator used to mount the diode and also minimise the coupling at 18 GHz back to the input via the 9 GHz filter route.

Traditionally this structure would be designed approximately by optimisation, however it is shown in this chapter that with the use of coupling matrix theory, a solution can be found.

Before the resonator spacing and locations for this structure can be decided, it is important to realise a simple but not instantly obvious fact about coupling matrix theory. Figure 7.12 shows a plot of how the internal *K* and external *Q* couplings relate to each other for a set of filter solutions for a bandpass filter with a centre frequency of 9 GHz and where the other filter specifications remain fixed; S_{11} response = -20 dB, *n*=3 and centre frequency = 9 GHz.

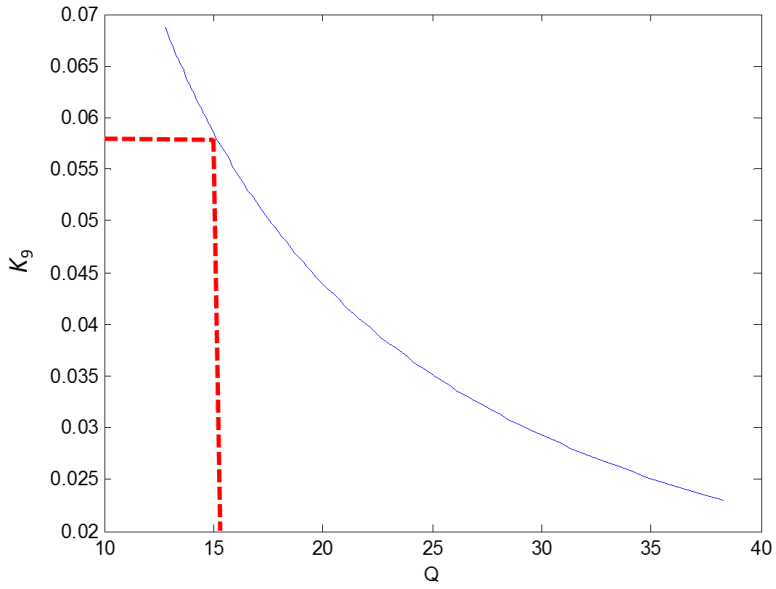

Figure 7.12 - How internal (*K*) and External (*Q*) coupling relate to each other at 9 GHz 0.5 GHz Bandwidth solution marked. (S_{11} fixed at -20dB, *n*=3)

Therefore each point on this plot will represent a filter solution with a unique bandwidth. A *Q* versus *K* plot for the 18 GHz bandpass filter is found in Figure 7.13, again with fixed S_{11} at -20dB and three resonators.

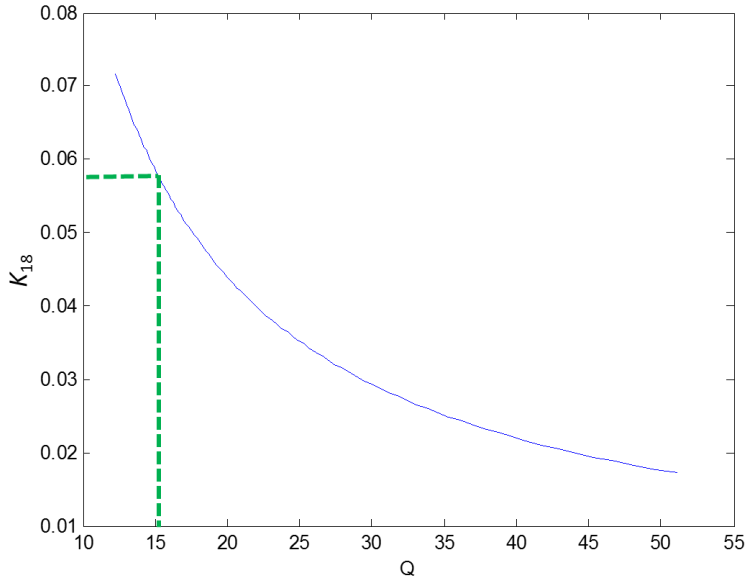

Figure 7.13 - How internal (*K*) and External (*Q*) coupling relate to each other at 18 GHz 1 GHz Bandwidth solution marked. (S_{11} fixed at -20dB, *n*=3)

It can be seen therefore that for any external coupling value *Q*, the bandwidth and the internal coupling value *K* are constrained for the filter. The vital thing to realise for the doubler structure design, is that not only does the external coupling value constrain the internal coupling for each filter, but because the couplings associated with gap d_3 overlap for both filters, then the couplings of the 18 GHz filter will also be affected by the value of Q_9. This situation is illustrated in Figure 7.14.

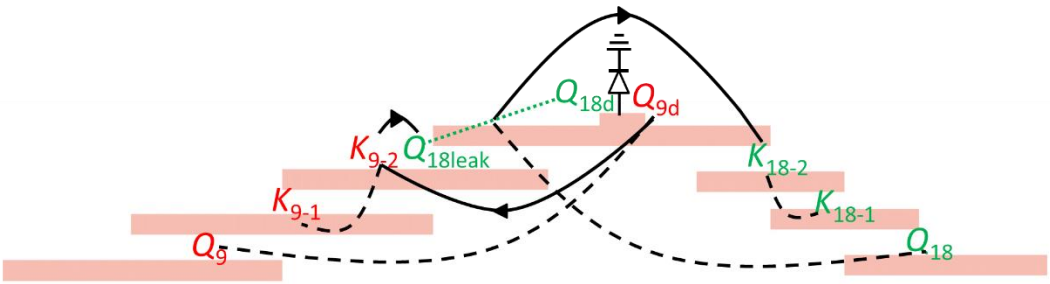

Figure 7.14 - Doubler structure showing the path of constraint of the internal and external couplings for both the 9 GHz and 18 GHz bandpass filters

Figure 7.14 shows a path of constraint starting from the value of the 9 GHz external coupling Q_{9d} to the diode. Q_{9d} is explained in more detail in the next section and its value is determined by the diode simulation parameters which are fixed from the data sheet values in Table 7.1, and the applied bias (not shown in Figure 7.14). This coupling will be considered the starting point that all other values will be determined from. The solid black lines show which couplings are then constrained by the Q_{9d} value. The 9 GHz internal coupling $K_{9\text{-}2}$ is constrained first, because of the relationship shown in the coupling matrix theory plot of Figure 7.12. The 18 GHz filters external coupling Q_{18} was shown in equation 7.1 to contain influence from Q_{18leak} and Q_{18d} (linked by a green dotted line). However the situation where Q_{18leak} is minimised so the coupling at 18 GHz goes to the diode and not the input, (i.e. when $Q_{18d}=Q_{18}$) is to be sought later in this chapter. The Q_{18leak} coupling is constrained to $K_{9\text{-}2}$, because it shares the same resonator gap as the $K_{9\text{-}2}$ coupling. These couplings are at different frequencies, and are not related in any other way other than by this sharing of the same gap. Therefore Q_{18leak} is physically related to the value of Q_{9d}. The final solid black line shows the constraint of $K_{18\text{-}2}$ by Q_{18} because of the coupling matrix relationship in Figure 7.13.

The dotted black lines in Figure 7.14 link to the other internal and external couplings within the circuit. Any couplings linked by a dotted black line must have identical coupling values if the coupling matrix theory design is to hold. Their physical gaps can be different, but their coupling values must be the same.

7.5.2 The solution

To solve this situation, the curves indicated in Figure 7.10 are to be obtained and fitted to equations, along with curve fit equations for the coupling matrix filter theory relationships of Figure 7.12 and Figure 7.13. Using these equations, a graphical analysis of the coupling gaps can be observed to see if there are any suitable solutions that allow 9 GHz and 18 GHz filters that minimise the coupling of the second harmonic at 18 GHz back to the input. It is shown in the detailed sections that follow that a solution is possible, and this solution is realised in a physical design which is also measured and reported at the end of this chapter.

7.5.3 Circuit Element Definitions

Figure 7.15 shows the microstrip doubler structure that will be analysed. The gaps between resonators are denoted by d_1 to d_6. It is externally connected via the input Port 1, which is connected to a 9 GHz frequency source with a 50 Ω impedance. Port 2 is the output connection, and is connected to a 50 Ω signal measurement system. The bias arrangement is omitted here for clarity, but can see seen later in the chapter.

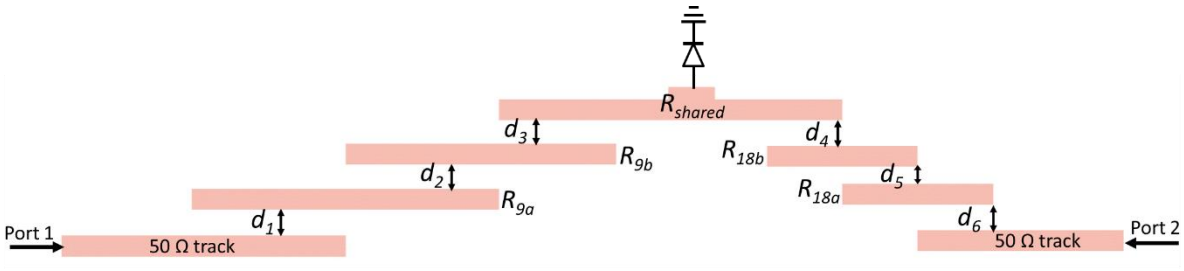

Figure 7.15 Microstrip diode doubler with integrated bandpass filters

A length of track with 50 Ω impedance connects from port 1, and by convention, is quarter wave coupled, as shown in Figure 7.16, to the first resonator, R_{9a} of the 9 GHz input bandpass filter. The external coupling is determined by the gap d_1.

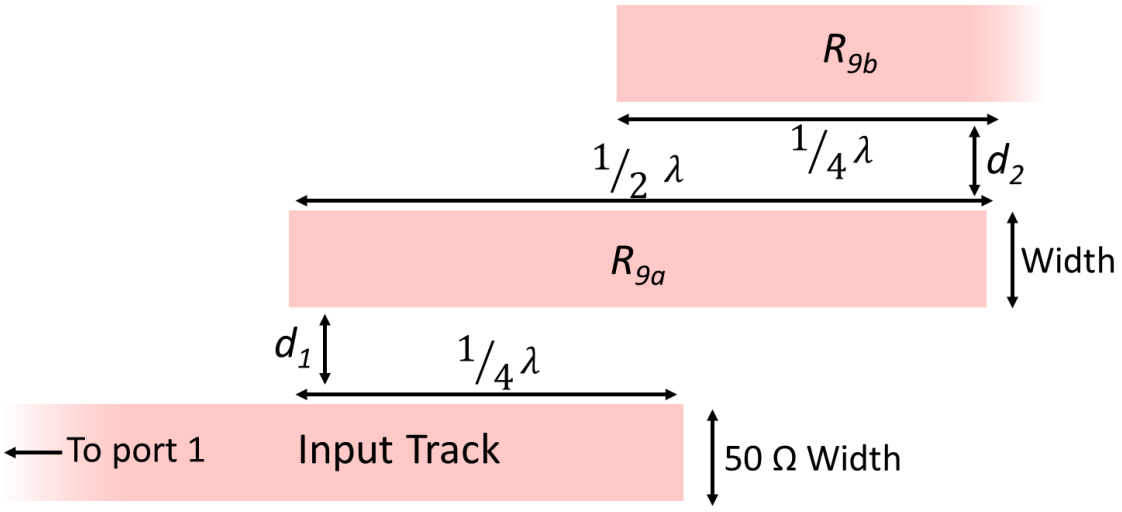

Figure 7.16- Detail of the 9 GHz input filter Resonator Configuration

The resonator R_{9a} is half a wavelength long at the input centre frequency. Its width is selected to set the external coupling $Q_{9\text{-}1}$ (how to measure this is shown later) to a value that can be same as

the other external coupling, Q_{9d}. Figure 7.17 and Figure 7.18 illustrate the effect of track width on the Q of the external coupling at 9 GHz.

Figure 7.17 shows that the Q is affected significantly by changing the width of the resonator as well as causing a frequency shift that will require correcting by changing the length of the resonator once the desired Q value is selected.

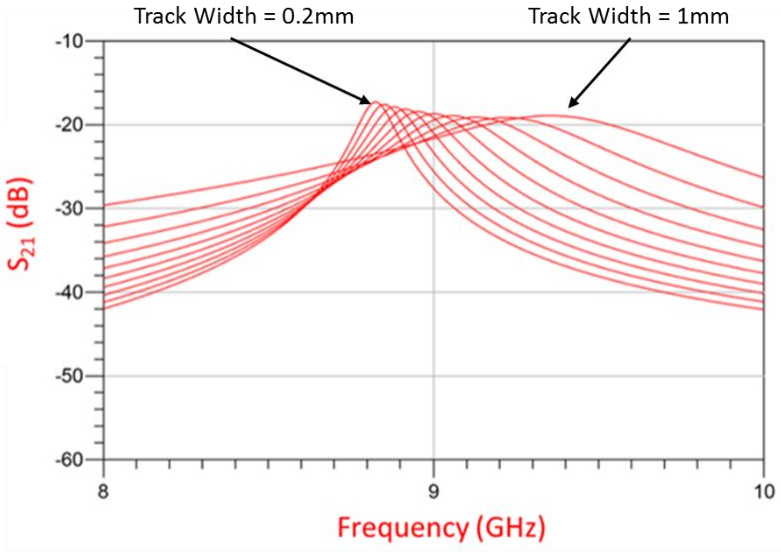

Figure 7.17 - Range of resonances formed by sweeping resonator track width (0.2mm to 1mm). The gap d_1 is constant during these measurements.

The range of Q's generated by sweeping the width of the resonator R_{9a} is shown in Figure 7.18, and the desired value can be selected from this graph. The track width determined for R_{9a} is used for the rest of the circuit for simplicity.

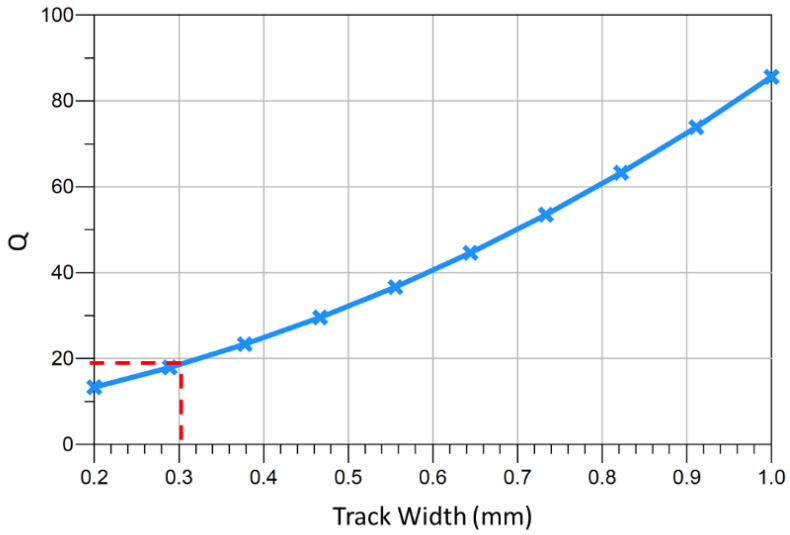

Figure 7.18 - Effect of resonator track width on *Q*. A resonator width of 0.3mm is used in the circuit, marked in red.

R_{9a} is coupled to R_{9b}, another half wave resonator element of the input filter, by the internal coupling coefficient $K_{9\text{-}1}$ determined by gap d_2. R_{9b} is coupled to the centre structure (R_{shared}), by the couplings Q_{18leak} at 18 GHz and $K_{9\text{-}2}$ at 9 GHz. Q_{18leak} is an external coupling at 18 GHz, and $K_{9\text{-}2}$ is an internal coupling at 9 GHz. Both of these couplings use the **same gap d_3**, but will have different values at their respective frequencies. Each of the couplings therefore require determining independently, as explained later in this chapter.

The centre structure, (R_{shared}) is a shared resonator with the doubling diode mounted initially half a wavelength at the input frequency from the left, and half a wavelength at doubled output frequency from the right to allow quarter wave coupling to the input and output filters and to setup a response similar to that of Figure 7.21. The exact positioning of this diode is described in the next section. The end of the shared resonator R_{shared} is coupled to the doubled frequency

output bandpass filter resonator R_{18b} with the coupling coefficient $K_{18\text{-}2}$ at 18 GHz using the gap d_4. R_{18b} is a half wavelength at the doubled frequency. This resonator is coupled to resonator R_{18a} with an internal coupling coefficient $K_{18\text{-}1}$ determined by the gap d_5. This final resonator of the output filter is coupled with an external coupling coefficient Q_{18} determined by gap d_6, to the 50 Ω output track. This track then connects to the 50 Ω port 2. The couplings defined above have their locations shown in Figure 7.19.

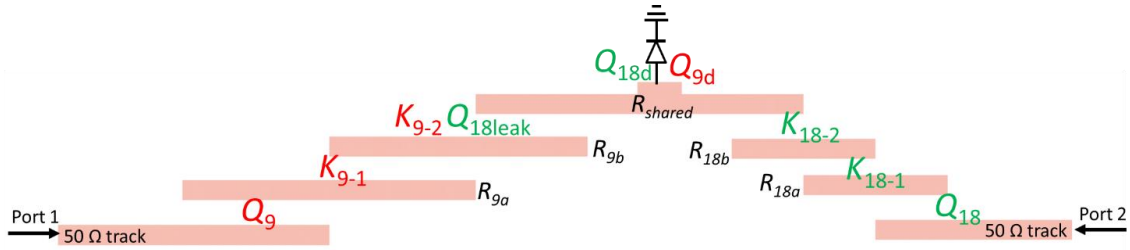

Figure 7.19 - Circuit structure showing defined coupling locations

7.5.4 Setting up the Circuit

A description of how to setup and analyse the circuit follows. The internal and external couplings introduced in the previous section are to be determined in the same way as for the coupling matrix method for filter design found in Chapter 3. The diagrams that follow show the sections of the circuit being analysed for either the fundamental input frequency of 9 GHz, or the doubled output frequency of 18 GHz. Where a port is shown connecting to a resonator for measurement purposes, that resonator is considered an input / output track and not part of the resonating mechanism. The greyed out sections are removed completely during the analysis, to eliminate spurious couplings, but are left in the diagrams to aid the reader to orient themselves within the circuit. The diode is biased during the analysis, with the value determined by ideal circuit optimisation in the previous section. It is also necessary to perform the following analysis using a

large signal analysis S parameter simulator configuration. Large signal analysis is done with AC simulation signals large enough so that devices with nonlinear effects are driven at a level where these effects become significant. This is to ensure the analysis is performed with the diode at its most efficient operating point, which will be dependent on the input power level as well as bias. The optimum input power and bias are determined as described in section 7.4.2 and shown in Figure 7.8.

7.5.4.1 Setting up the Shared Resonator (R_{shared})

The shared resonator is set up using the analysis structure shown in Figure 7.20. The measurement ports 1 and 2 are connected to the resonators R_{9b} and R_{18b} respectively as shown; it should be noted that R_{9b} and R_{18b} behave as feed lines in this case, not resonators.

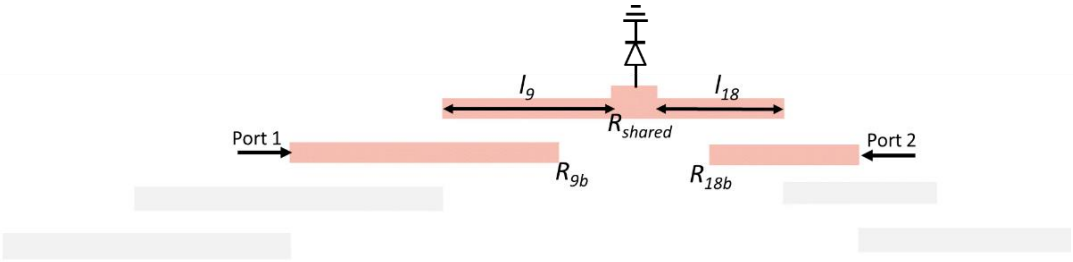

Figure 7.20 Circuit setup for determining length of resonator R_{shared}

Using a S_{21} simulation setup, and adjusting the length of the track section $l_{9,}$ a resonance can be set to 9 GHz. By adjusting the track section $l_{18,}$ an 18 GHz resonance can also be set, as shown in Figure 7.21.

Once these resonances are set, the measurement of the external couplings can then be made.

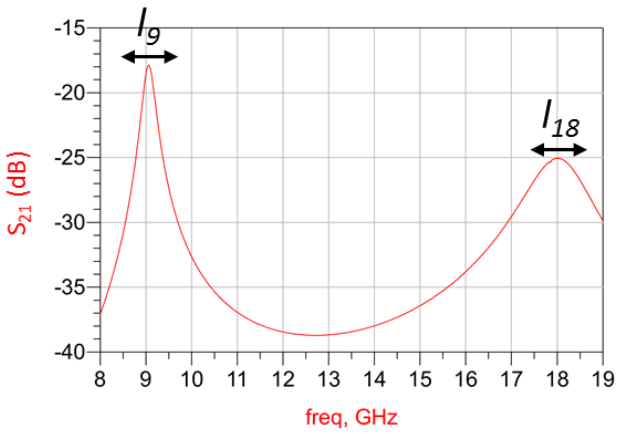

Figure 7.21 - The two resonances of the shared resonator.

(Values used can be found in table 7.2, diode bias -4.4V).

7.5.4.2 Measuring external coupling Q_{9d}

Q_{9d} can be determined using the measurement setup in

Figure *7.22*. Port 1 and Port 2 are again connected to R_{9b} and R_{18b} as shown (again, these

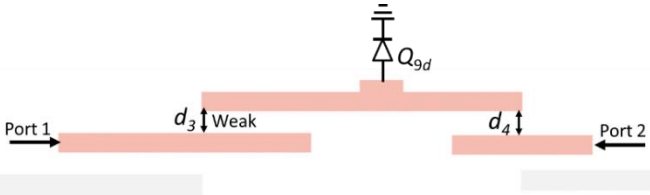

resonators are used as feed lines for this measurement).

Figure 7.22 – Setup for measuring Q_{9d} by sweeping gap d_4

The gap d_3 should be weakly coupled so only the d_4 gap is influencing the 9 GHz resonance shape. The d_4 gap is then swept through a range of values and the resultant resonances are recorded and Q's calculated, as shown in Figure 7.23 and Figure 7.24 .

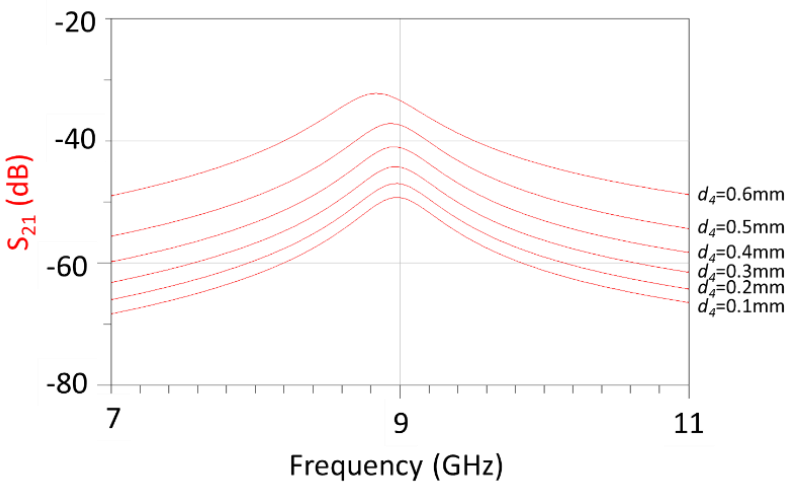

Figure 7.23 - The range of resonances obtained by varying the gap d_4

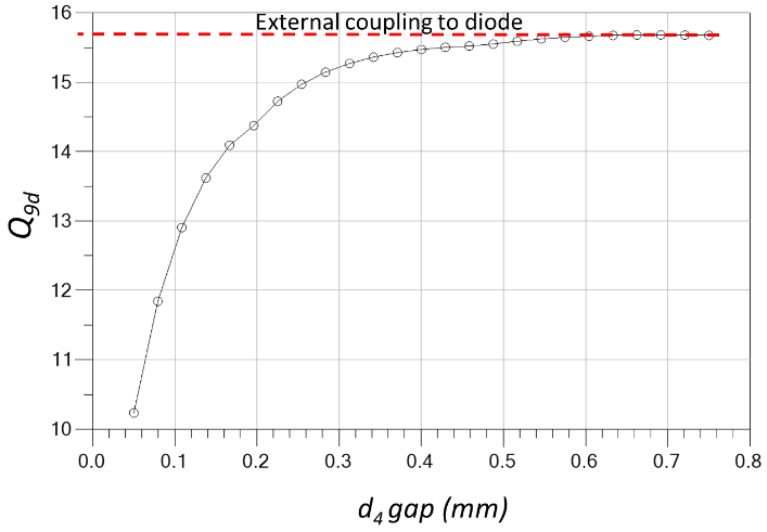

Figure 7.24 – Plot of the calculated Q's versus d_4 gap

(diode bias -4.4V)

However, as there will be no coupling at 9 GHz to the output through the 18 GHz resonators in the full circuit, only the steady state value in Figure 7.24 is of interest as this will be the value of the external coupling to the diode. Q_{9d} as previously stated is affected by the diodes parameters which are fixed from the datasheet, and the bias voltage, as shown in Figure 7.25. The effect on the external coupling Q_{18d} is also shown in Figure 7.25. The Q_{18d} coupling is explained in more detail later in this section.

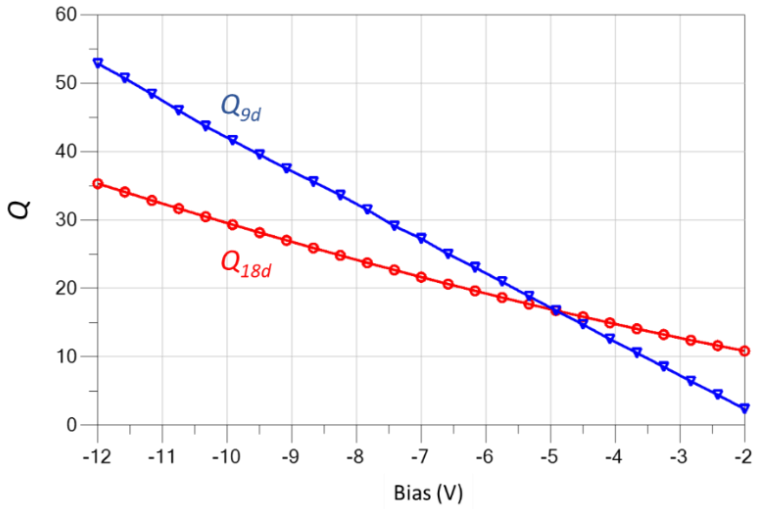

Figure 7.25 - Effect of change in diode bias voltage to the external couplings Q_{9d} and Q_{18d}

7.5.4.3 Measuring external coupling Q_9

The external coupling Q_9 can be determined using the setup shown in Figure 7.26. Port 1 is connected to the 50 Ω input track and port 2 is connected to R_{9b} as shown (R_{9b} acting as a feed line in this case). The gap d_2 between R_{9a} and R_{9b} should be large enough so that those resonators are weakly coupled and the curve shape measured is influenced by the d_1 gap only.

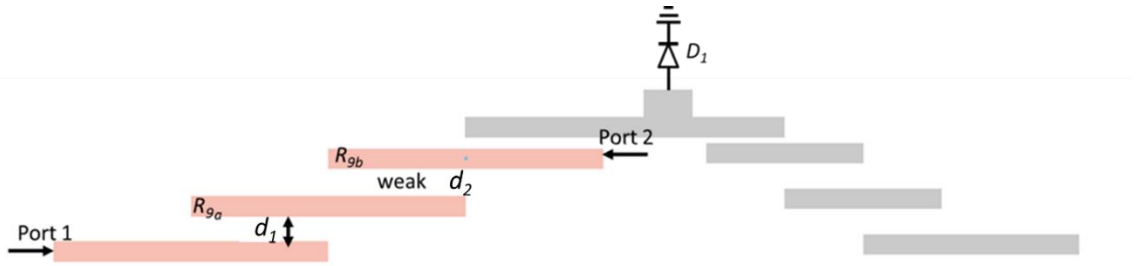

Figure 7.26 – Circuit setup for measuring Q_9

d_1 is then swept through a range of values and the resultant Q's are calculated from the curves obtained, and are plotted in Figure 7.27. The dimensions not shown are found in Table 7.2.

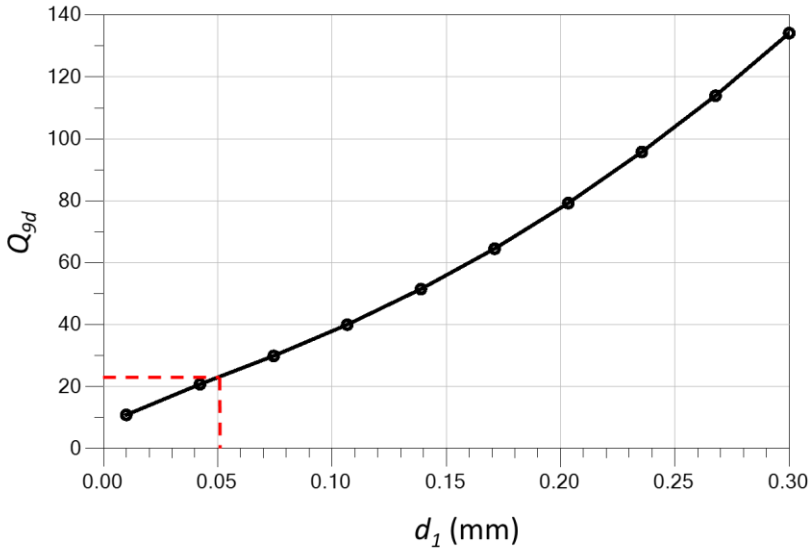

Figure 7.27 – Plot of Q_{9d} versus physical gap d_1. Gap used in circuit design marked in red.

7.5.4.4 Measuring internal coupling $K_{9\text{-}1}$

The internal coupling of the 9 GHz input filter is profiled with the configuration shown in Figure 7.28.

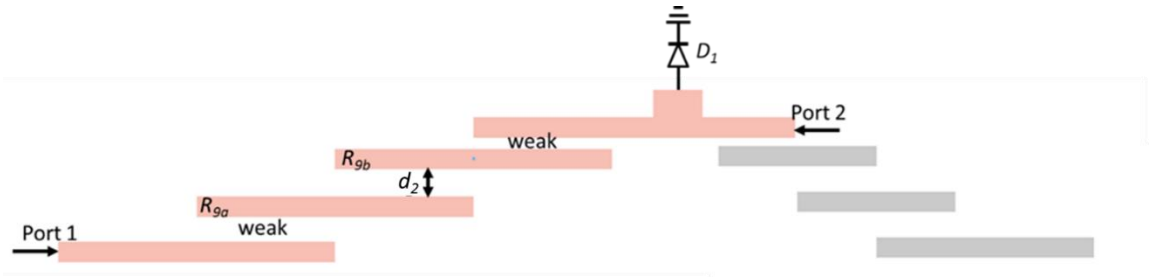

Figure 7.28 – Measurement setup for finding internal coupling $K_{9\text{-}1}$

Port 1 is again connected to the 50 Ω input track, and port 2 to the 18 GHz side of the shared centre resonator as shown. The gap between the input track and R_{9a}, and the gap between the shared resonator and R_{9b} should be chosen to so that the twin peaks are clearly seen and the frequency of each peak can be easily recorded. The gap d_2 is swept through a range of values, resulting in a set of double peaks, as shown in Figure 7.29. The internal K coefficient can be determined as described in Chapter 3, and is plotted in Figure 7.30.

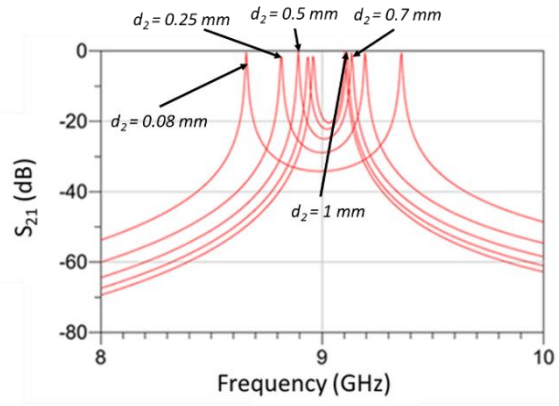

Figure 7.29 - The double peaks of the internal coupling gap sweep

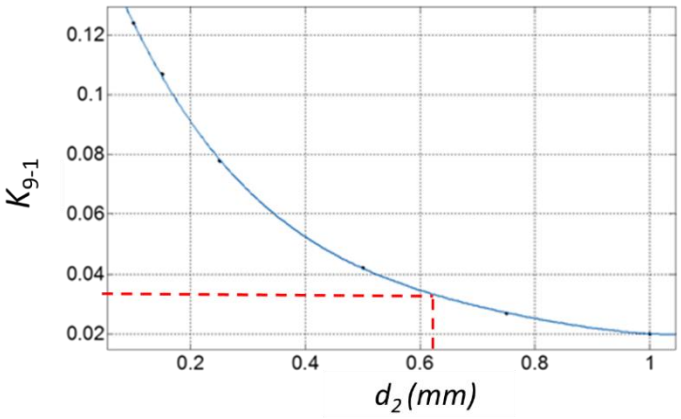

Figure 7.30 - The resultant $K_{9\text{-}1}$ values versus gap d_2. Design value shown in red.

7.5.4.5 Measuring Internal coupling $K_{9\text{-}2}$

The circuit configuration to profile the internal coupling $K_{9\text{-}2}$ is shown in Figure 7.31, with port 1 connected to R_{9a} and port 2 connected to R_{18b}. Again the resonators are used as feed lines in this circuit.

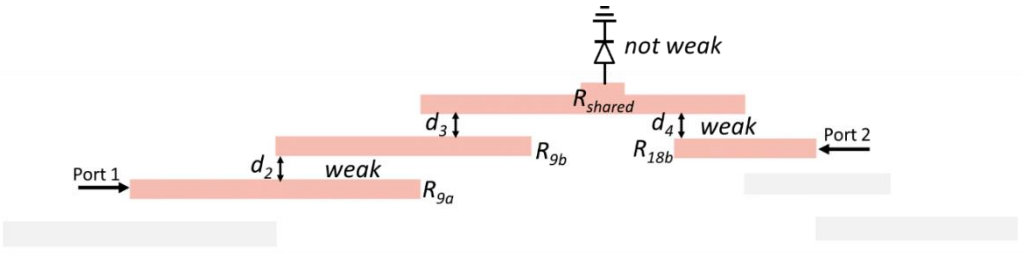

Figure 7.31 - The setup for measuring the internal coupling K_{92}

The gaps d_2, and d_4 should be set so the double peaks are most easily recorded for their respective frequencies. The gap d_3 is swept through a range of values, resulting in a set of double peaks, and the K coupling coefficient can be determined as shown in chapter 3. The resultant $K_{9\text{-}2}$ profile is shown in Figure 7.32. However, it should be noted that because the external coupling to the diode in this setup is not weak (as indicated in Figure 7.31), this time the double peaks will not be as

sharp and some care is needed when recording the values. An example of some of the double peaks obtained is shown in Figure 7.33.

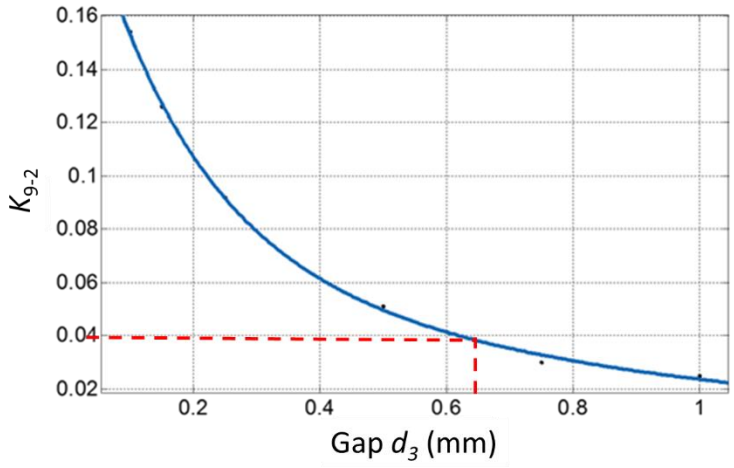

Figure 7.32 - Plot of internal coupling $K_{9\text{-}2}$ versus gap d_3. Design value shown in red.

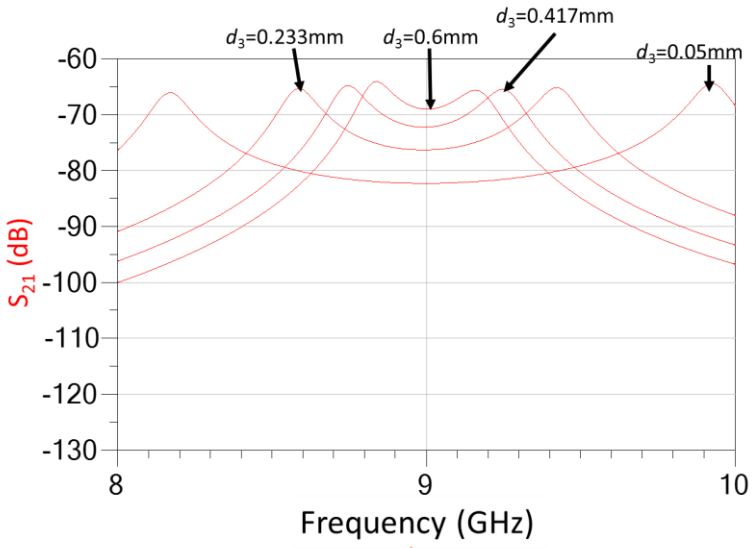

Figure 7.33 - Example of the "rounded" double peaks due to the strong coupling to the diode (Q_{9d})

7.5.4.6 Measuring External coupling Q_{18d}

Q_{18d} can be determined using the measurement setup in Figure 7.34. Port 1 and Port 2 are again connected to R_{9b} and R_{18b} as shown (these resonators are again used as feed lines only).

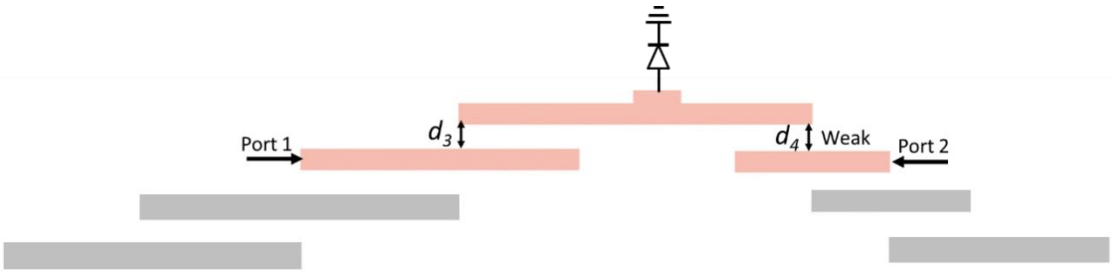

Figure 7.34 – Measuring Q_{18d} by sweeping gap d_3

The gap d_4 should be weakly coupled so only the d_3 gap is influencing the 18 GHz resonance shape. The d_3 gap is then swept through a range of values and the resultant resonances are recorded and Q's calculated, as shown in Figure 7.35.

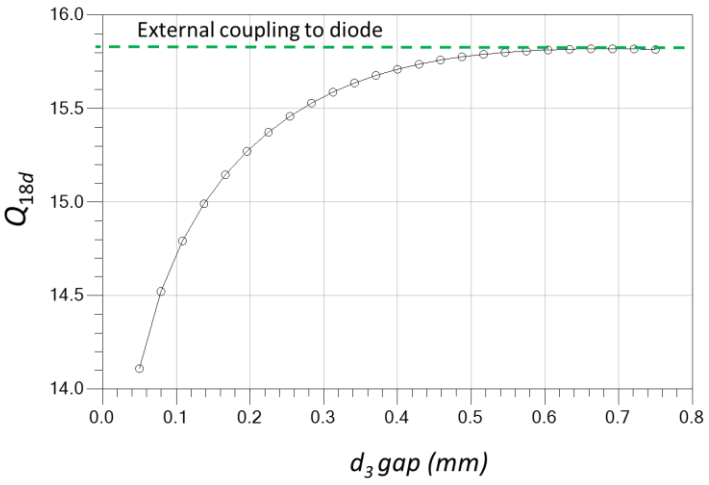

Figure 7.35 - Plot of the calculated Q's versus d_3 gap

It can be seen from Figure 7.35 that when the coupling gap d_3 is greater than around 0.6mm, then the coupling value levels off. This region is considered the Q value of the diode to which the gap d_3 no longer influencing the shape of the resonance. It is therefore desirable to find a filter solution for this gap that allows a good 9 GHz performance, but having a suitably large gap (> 0.6mm) so that the 18 GHz coupling is minimised. Using equation 7.1 and these findings, it can be suggested that with d_3 larger than 0.6mm then the coupling Q_{18leak} is no longer significant, and that $Q_{18d} = Q_{18}$ for the purposes of designing the circuit.

The four couplings $Q_{9\text{-}1}$, Q_{9d}, $K_{9\text{-}1}$ and $K_{9\text{-}2}$ are the complete set of 9 GHz couplings required, and the next step is to repeat the measurements at 18 GHz for the last three unknown couplings; Q_{18}, $K_{18\text{-}1}$ and $K_{18\text{-}2}$. Once this is complete, the set of profiled couplings as illustrated in Figure 7.36 can then be used to design the frequency doubler circuit.

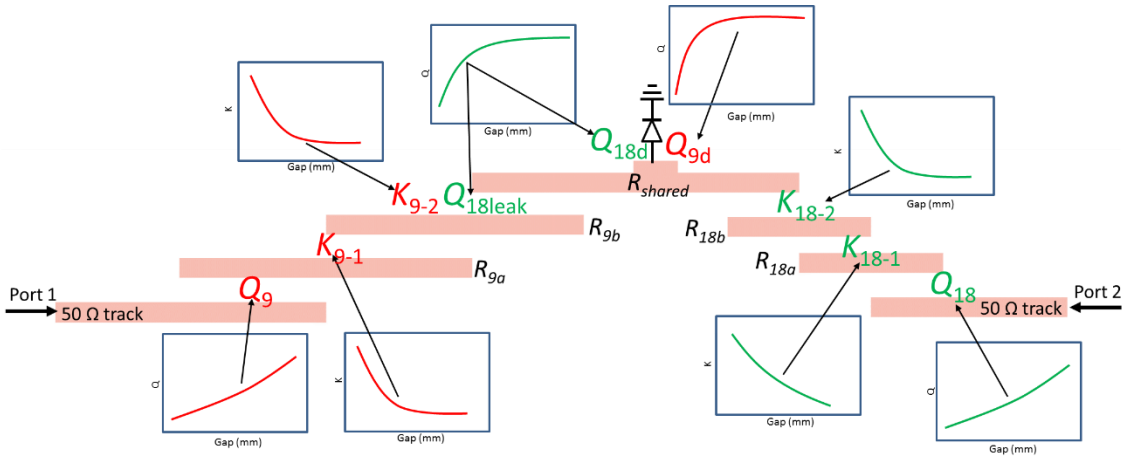

Figure 7.36 - Doubler Structure and summary of analysis curves obtained

These curves combined with the coupling matrix theory explained in chapter 3, can be used to determine a solution for the 9 GHz input and 18 GHz output bandpass filters.

7.5.5 Finding the Solution for the integrated filter diode doubler.

The two key couplings to consider when designing the diode frequency doubler circuit are the "steady state" values of couplings Q_{9d} and Q_{18d} shown in Figure 7.24 and Figure 7.35 respectively. These values are affected by the diode bias value (see Figure 7.25), which has been set at the optimum point of -4.4V as explained earlier in this chapter. However, it shall be shown in section 7.5.5 that deviating from the previously determined optimum bias point can be advantageous when considering the design of the diode resonator gaps and couplings.

To determine how to set the bias and resonator gaps it is required to fit the Q and K curves determined in section 7.5.4 to equations and plot these relative to the swept bias values.

The first step to doing this is to remember that the relationship between the external and internal coupling Q and K are related by the curves shown in Figure 7.12 and Figure 7.13 for 9 GHz and 18 GHz respectively. Each point on those curves corresponds to a filter solution with a different bandwidth. Those plots show how K varies against Q, and the curves can be fitted to the approximate power series K_9 and K_{18} below, where a_{9a}, b_{9a}, a_{18a} and b_{18a} are the fitting coefficients. Details on the curve fitting and the coefficient values are found in Appendix 3.

$$K_9 = a_{9a} Q_9^{b9a} \tag{7.2}$$

$$K_{18} = a_{18a} Q_{18}^{b18a} \tag{7.3}$$

So, as in the explanation at the start of this section, Q_{9d} is chosen as the starting point because it constrains the rest of the couplings in the design and is adjusted only by sweeping the bias. However, as we have seen there are two couplings associated with gap d_3 at different frequencies.

Therefore, the curve fit for Q_{9d} (Figure 7.25) where a_{9b}, b_{9b} and c_{9b} are the fit coefficients and v is the bias voltage, is given by:

$$Q_{9d}=a_{9b}\,v^2+b_{9b}\,v+c_{9b} \tag{7.4}$$

The Q_{9d} values are therefore obtained from equation (7.4). The equation for gap d_3 is shown in (7.5) where K_9 is from equation (7.2) using Q_{9d} as the Q term, and a_{9c}, b_{9c} and c_{9c} are the curve fit coefficients for $K_{9\text{-}2}$.

$$d_3 = \frac{K_9 - c_{9c}}{a_{9c}^{\frac{1}{b_{9c}}}} \tag{7.5}$$

Now that d_3 is determined, constrained by Q_{9d}, the range of Q_{18leak} values are constrained also as the d_3 is the same gap as that for $K_{9\text{-}2}$, i.e.:

$$d_{3(for\ Q18leak)} = d_{3(for\ K9\text{-}2)} \tag{7.6}$$

However, as shown in Figure 7.25, if the steady state case is relevant (i.e. $d_3 > 0.6$mm) then the Q_{18d} / Q_{18leak} coupling is dependent on the bias voltage and not the gap d_3 size any more.

$$Q_{18d}=a_{18b}\,v^2+b_{18b}\,v+c_{18b} \tag{7.7}$$

So the Q_{18} curve, will be the same as the Q_{18d} curve:

$$Q_{18} = Q_{18d} \tag{7.8}$$

And so now d_4 follows from (7.8) by using equation (7.9) where a_{18c}, b_{18c} and c_{18c} are the curve for coefficients for the $K_{18\text{-}2}$ curve, and K_{18} is from (7.3)

$$d_4 = \frac{K_{18} - c_{18c}}{a_{18d}^{\frac{1}{b_{18d}}}} \tag{7.9}$$

Equations for the remaining gaps can now be found, starting with d_5 using equation (7.9), K_{18} from (7.3) and where a_{18d}, b_{18d} and c_{18d} are the curve coefficients for $K_{18\text{-}1}$.

$$d_5 = \frac{K_{18} - c_{18d}}{a_{18d}^{\frac{1}{b_{18d}}}} \tag{7.10}$$

And then d_1 using the relationship that for a matched filter the external Q's must be equal, i.e. equation (7.11) and (7.12)

$$Q_9 = Q_{9d} \tag{7.11}$$

$$Q_{18} = Q_{18d} \tag{7.12}$$

For d_1 using the curve fit for Q_9 and the curve coefficients a_{9d}, b_{9d}, c_{9d} it can be determined:

$$d_1 = \frac{Q_{9d} - c_{9d}}{a_{9d}^{\frac{1}{b_{9d}}}} \tag{7.13}$$

And finally d_2 can be found from the $K_{9\text{-}1}$ curve fit with the curve coefficients a_{9e}, b_{9e} and c_{9e}, and using Q_{9d} in the relationship in (7.2), to form:

$$d_2 = \frac{K_9 - c_{9e}}{a_{9c}^{\frac{1}{b_{9e}}}} \tag{7.14}$$

It is now possible to plot all the gaps d_1 to d_6 relative to the bias voltage sweep (which determines the value of external coupling Q_{9d} and Q_{18d}), and this is shown in Figure 7.37.

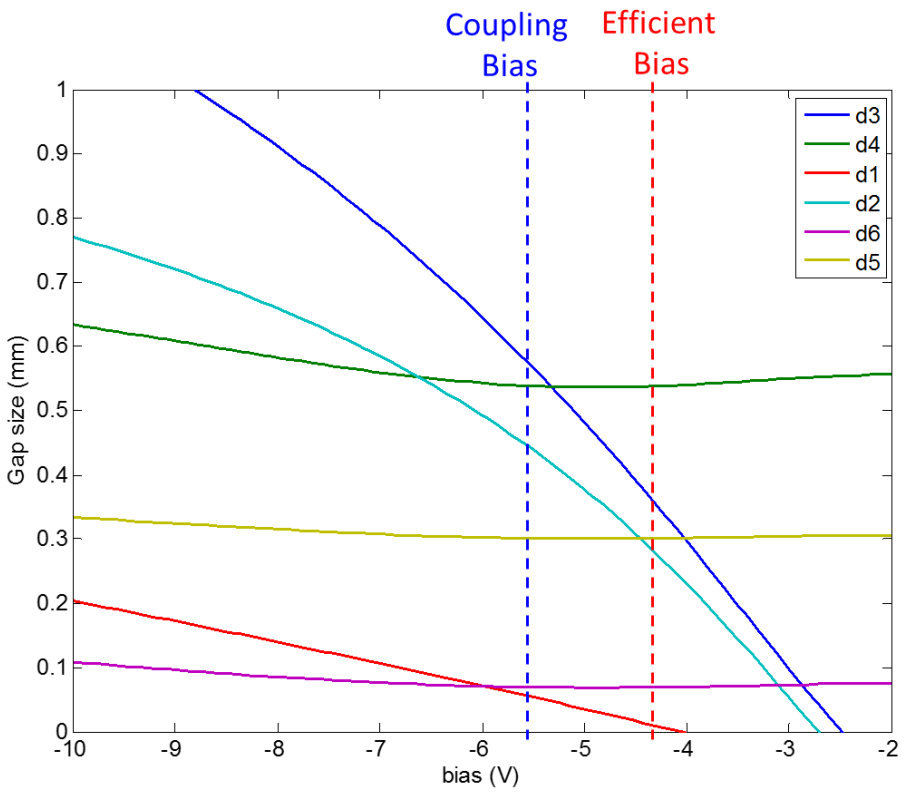

Figure 7.37 - Gap settings for filters relative to the bias voltage sweep

This plot is very useful as it shows how the bias voltage controls the Q_{9d} coupling, which determines the $K_{9\text{-}2}$, $K_{9\text{-}1}$ and Q_9 couplings, which sets the gaps d_1, d_2 and d_3 as shown. This is important because to minimise the coupling at 18 GHz back to the input, d_3 should be larger than 0.6mm. If this gap is larger than 0.6mm then the Q_{18d} coupling is influenced by the bias voltage only, and this determines couplings $K_{18\text{-}2}$, $K_{18\text{-}1}$ and $Q_{18,}$ and hence the gaps d_4, d_5 and d_6 as shown. It can be seen that this will be the case if the diode bias is less than -5V. It can be seen that if the bias is further reduced then the gap d_3 can be increased even more. However, this will reduce the bandwidth of the circuit and also move the diode's bias further away from its optimum

point of -4.4V (marked “efficient bias” in Figure 7.37). It was found by running a few simulations at different points along the bias curve (and adjusting the resonator gaps accordingly) that a bias value of -5.6V (marked “coupling bias” in Figure 7.37) was the best value, as it sets the gap d_3 greater than the required 0.6mm. There is an additional advantage of doing this which is the gap d_1 is increased from a distance of a few microns to 0.05mm, which is a physically realisable value now for a microstrip circuit.

The chosen filter responses are shown below in Figure 7.38 and Figure 7.39 which are obtained from coupling matrix simulation.

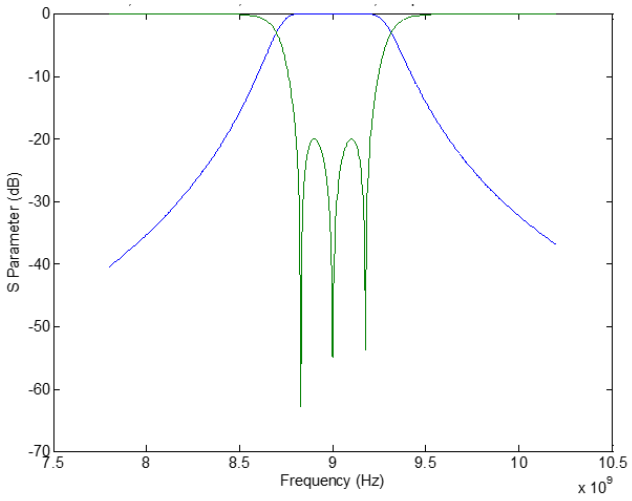

Figure 7.38 - 9 GHz input bandpass filter solution.

Bandwidth = 0.4 GHz, S_{11} max =-20 dB, n=3, Q=19.16, K = 0.045

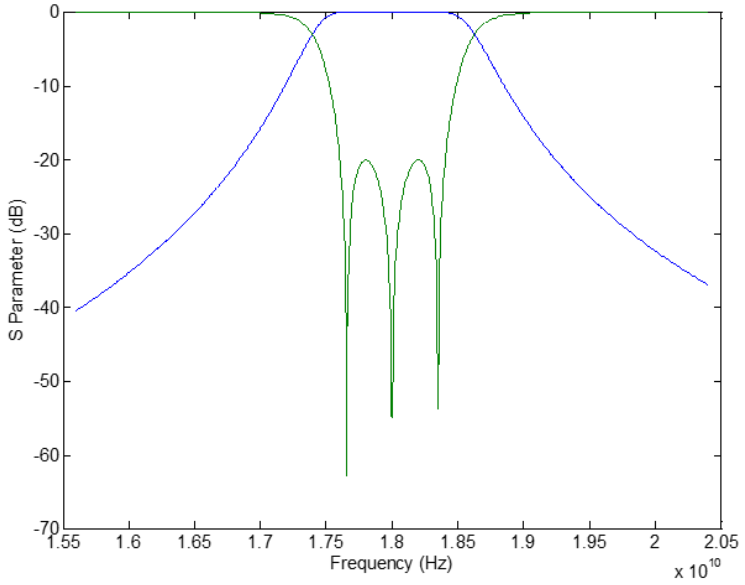

Figure 7.39 - 18 GHz bandpass output filter solution

Bandwidth = 0.8 GHz, S_{11} max =-20 dB, n=3, Q=19.16, K = 0.045

The gaps from Figure 7.37 can now be put into a circuit simulation [3]. The first attempt run is a good measure of the success of this method, and the results are shown in Figure 7.40, Figure 7.41, and Figure 7.42. It can be seen that the first attempt result is a reasonable solution. The values of the gaps were then optimised as shown in Figure 7.40, Figure 7.41 and Figure 7.42 also for comparison. The band is defined quite well already (Figure 7.40), the efficiency is already around half of the optimal value (Figure 7.41), and the input return loss of Figure 7.42 shows at least two of the three reflection zeros. Overall the first attempt is suitably close to the optimised result. The optimisation is done by manual tuning of the model parameters for peak conversion efficiency over the required band.

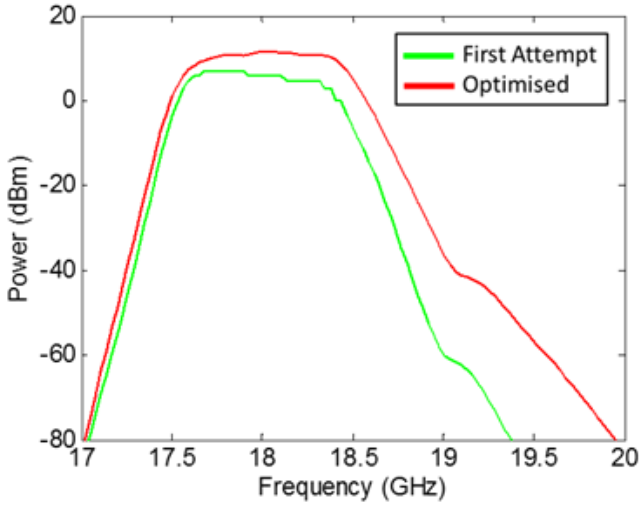

Figure 7.40 - Comparison of the first attempt and optimised second harmonic power output of the simulated diode doubler circuit (Diode bias = -4.4V)

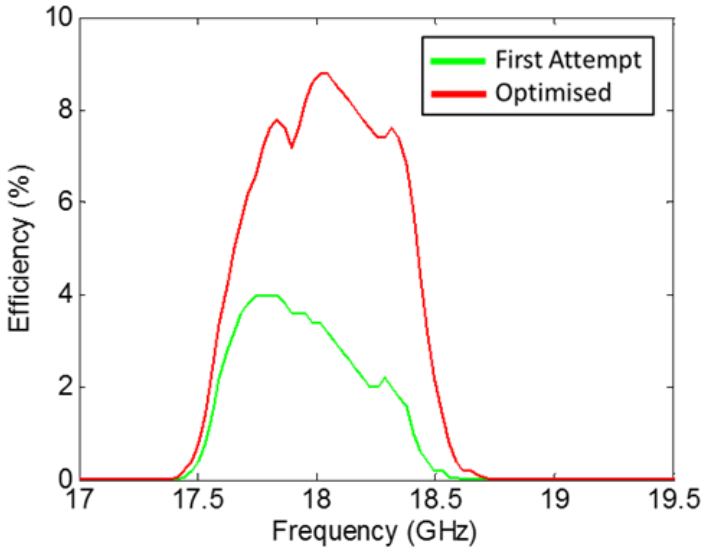

Figure 7.41 - Comparison of first attempt and optimised simulated diode doubler circuit efficiency

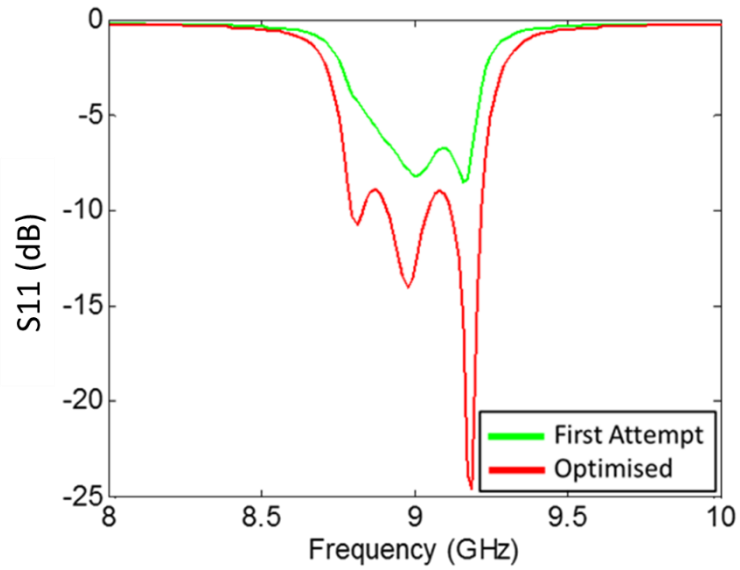

Figure 7.42 - Comparison of first attempt and optimised diode doubler circuit simulated S_{11} response

7.6 Diode doubler circuit manufacture and test

As with any design, there are a few additional steps required to take the simulated model to create a buildable solution. This section reveals the additional steps required to manufacture the circuit into a practical circuit that can have power applied and connections made to the test equipment.

7.6.1 Adding the bias Circuit

For the work described in the previous sections, the analysis was done with a full wave electromagnetic model simulator with the bias arrangement connected. Also, for clarity reasons some of the diagrams have the bias circuit omitted. Figure 7.43 shows the same doubler circuit model that has previously been analysed, but with the bias network now attached. Figure 7.44

shows a close up of just the bias network and all the design details are shown in Figure 7.45 and Table 7.2. The bias connection is required to connect to the diode, but must not affect the function and performance of the circuit. A thin track is used for the bias connection to create a high impedance path for the high frequencies, and for additional thoroughness, radial stubs are fitted to provide high frequency grounding for both the fundamental and doubled frequencies. The radial stubs are set up either using computer aided design tools or from the theory contained in [4] and [5]. Decoupling capacitors are added onto the bias line near to the external bias wire connection pad to provide a path to ground for a.c. interference that may source from the external bias connection.

A mounting pad for a wire to be soldered on for connection to the power supply is supplied and the ground wire to the power supply is soldered at any suitable point on the copper backplane on the reverse side of the board.

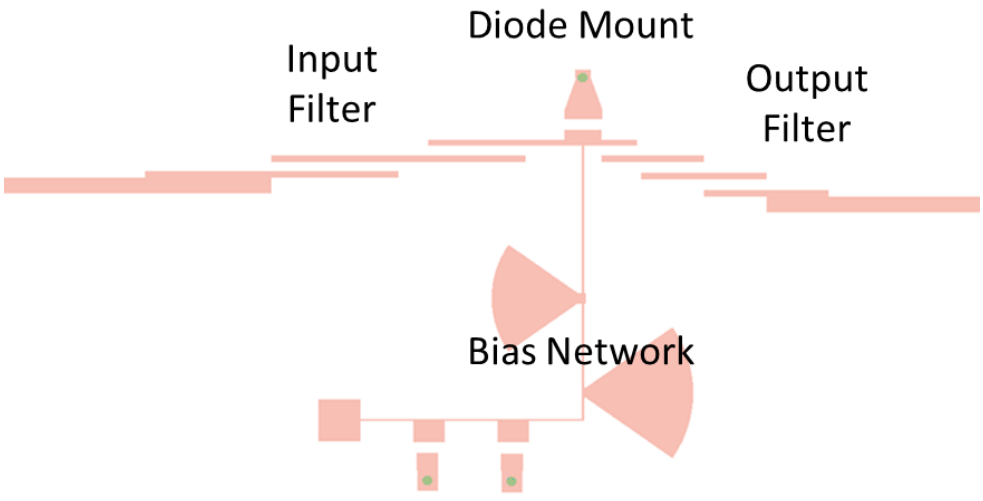

Figure 7.43 – Diode doubler circuit showing bias network

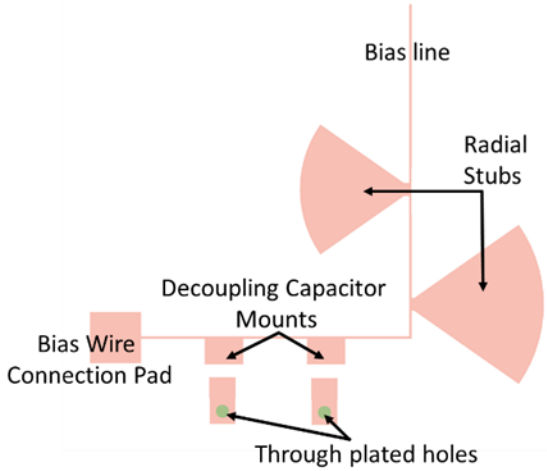

Figure 7.44 - Diode Doubler Bias Network

7.6.2 Manufacturing detail

The dimensions of the microstrip diode frequency doubler circuit are defined in Figure 7.45, and the parameter values are given in table 7.2.

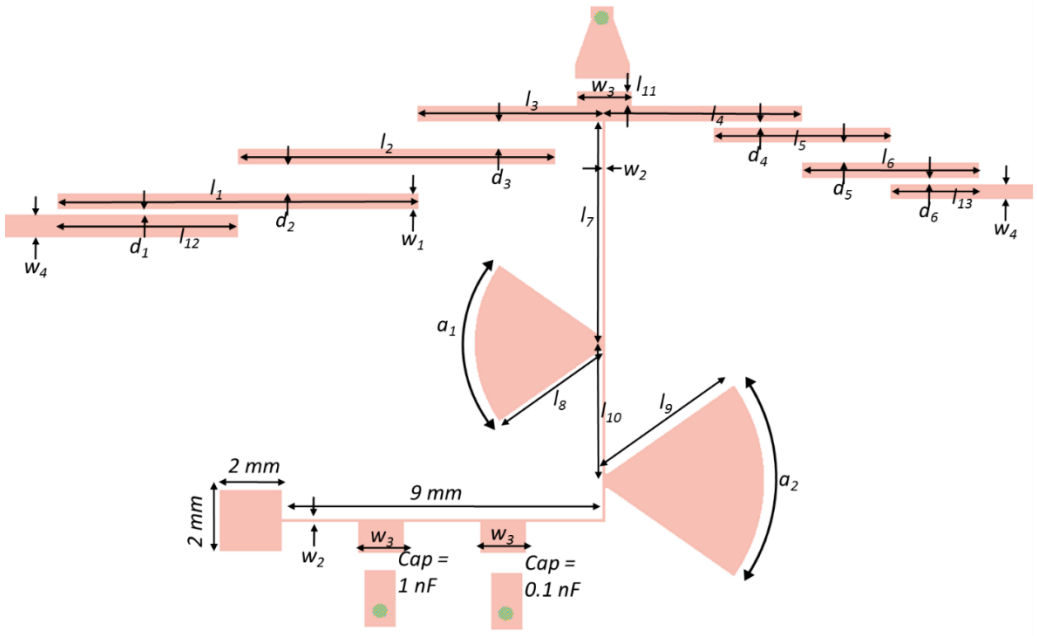

Figure 7.45 - Manufacturing dimensions of the microstrip diode doubler circuit

Table 7.2 - Diode doubler circuit dimensions. Pre and post optimisation results shown.

Circuit Parameter	Initial Value	Opt. Value	Unit		Circuit Parameter	Initial Value	Opt. Value	Unit
d_1	0.05	0.05	mm		l_1	11.8	11.82	mm
d_2	0.62	0.58	mm		l_2	11.8	11.77	mm
d_3	0.65	0.712	mm		l_3	5.489	5.473	mm
d_4	0.58	0.511	mm		l_4	5.315	5.305	mm
d_5	0.35	0.311	mm		l_5	5.78	5.78	mm
d_6	0.1	0.082	mm		l_6	5.78	5.78	mm
a_1	70	70	deg		l_7	7	7	mm
a_2	70	70	deg		l_8	4	4	mm
w_1	0.3	0.3	mm		l_9	5	5	mm
w_2	0.1	0.1	mm		l_{10}	4	4	mm
w_3	1.778	1.778	mm		l_{11}	0.47	0.47	mm
w_4	0.742	0.742	mm		l_{12}	2.95	2.95	mm
					l_{13}	1.445	1.445	mm

7.6.3 Testing the performance of the shared resonator doubler

A photograph of the manufactured board can be seen in Figure 7.46. Note that the circuit is small enough to fit into a universal test fixture (Anritsu model 3680K), due to the sharing of the third resonator and no requirement for tuning stubs. The universal test fixture is an adjustable jig that can clamp onto adjacent sides of a microstrip board with two precision k-connectors along each edge. The fixture ensures a good and repeatable connection to the board providing the board edges are cut parallel.

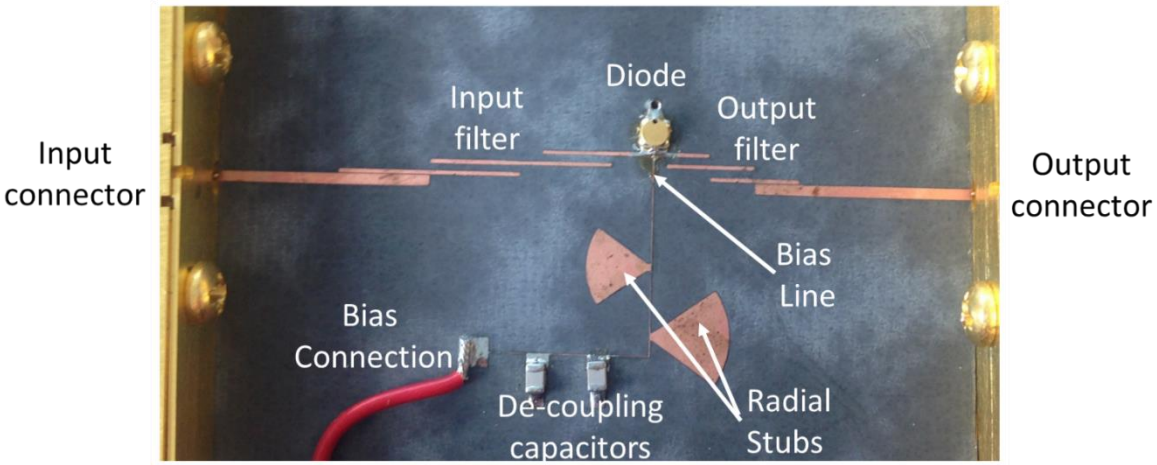

Figure 7.46 - Photograph of constructed circuit

To determine the circuit's frequency doubling efficiency, a fundamental frequency is generated at the input of the circuit and the doubled frequency is measured at the output with a spectrum analyser. The frequency is swept across a range of values which will generate a doubled frequency band at the output. The test configuration for this is shown in Figure 7.47.

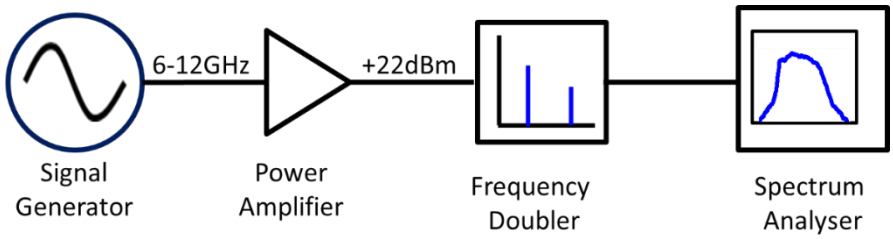

Figure 7.47 - Block diagram of Diode Doubler Test Setup

Initially the signal generator is set to a 9GHz fixed frequency and is amplified with a power amplifier (mini circuits model ZVA-183+). Power output is checked to ensure the level at the input of the frequency doubler is correct, and then the frequency swept to ensure the level remains constant across the sweep. The signal generator frequency output is swept from 6 to 12 GHz to check the power level remains constant. A spectrum analyser is connected to the output of the frequency doubler and the doubled frequency measured with the 'peak hold' function to build up an image of the band output while the input is swept. The resultant measurement is shown in Figure 7.48.

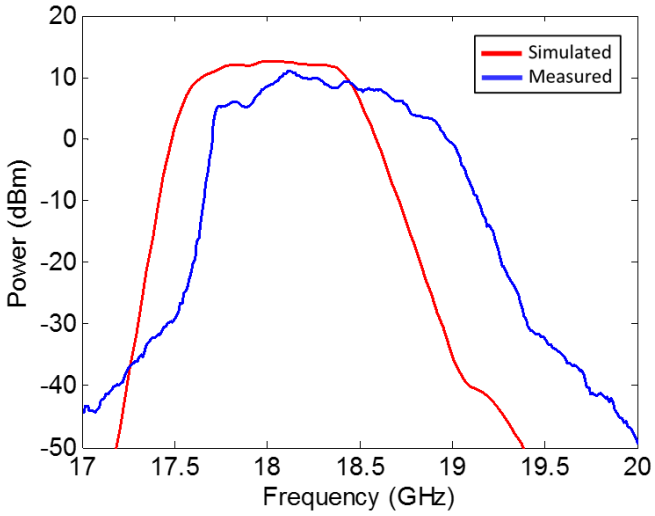

Figure 7.48 - Second Harmonic output of the diode doubler

The input power level P_{in} is known, and so is the doubled power level at the output (P_{out}) so the doubling efficiency *Eff* can be determined from

$$Eff(\%) = \frac{P_{out}}{P_{in}} \times 100 \qquad 7.15$$

The result of this calculation across the band is plotted in Figure 7.49.

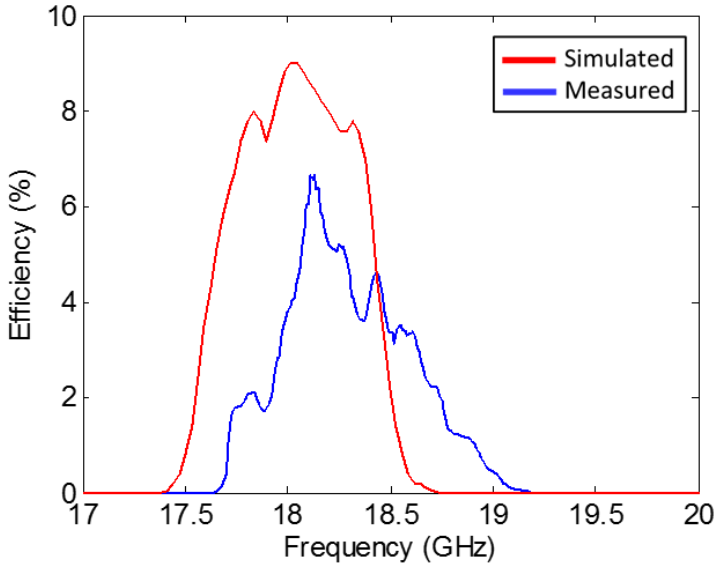

Figure 7.49 - Diode doubling circuit efficiency

The doubling conversion loss is plotted in Figure 7.50 for comparison with other doublers that do not have conversion efficiency figures.

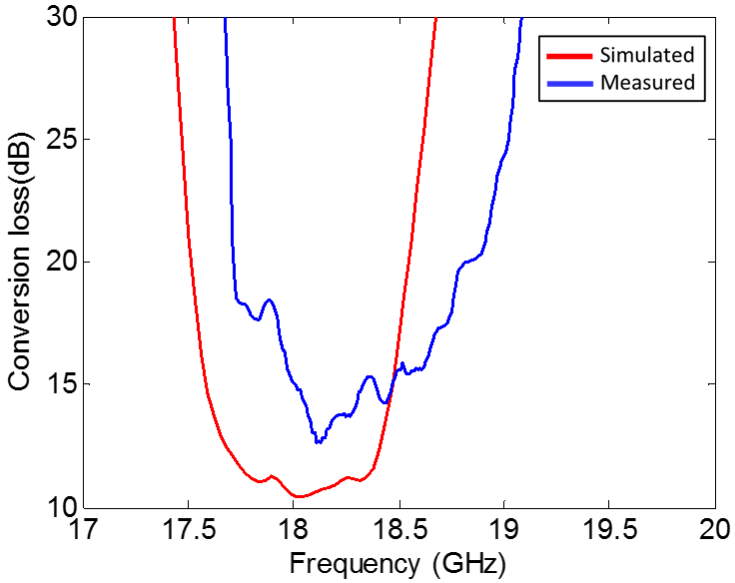

Figure 7.50 - Diode Doubler Conversion loss

The input return loss was also measured, using a network analyser (Agilent PNA network analyser E8362C). This was done with a single port calibration at a power level of 0 dBm. The circuit port not being measured was terminated with a 50 Ω load. The circuit was measured with the diode biased at -4.4V to ensure the correct circuit state is measured. The return loss for the output section of the circuit at 18 GHz is shown in Figure 7.52, the S_{11} return loss results are shown in Figure 7.51 and the doubled frequency power level versus the input power is shown in Figure 7.53.

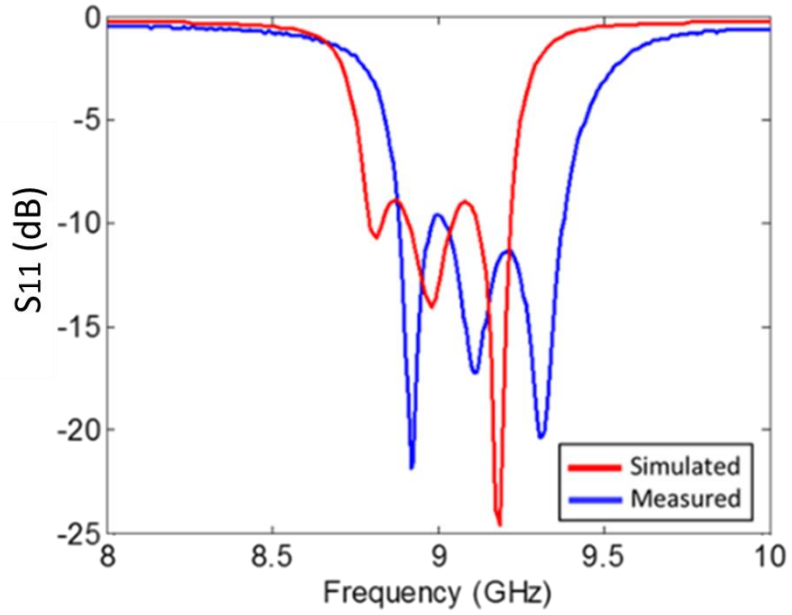

Figure 7.51 - Diode Doubler return loss, S_{11} at 9 GHz

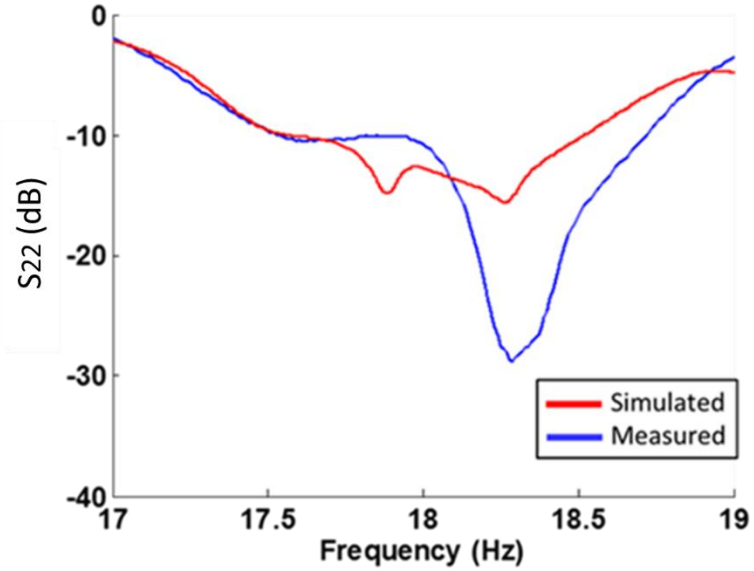

Figure 7.52 - S_{22} return loss at 18 GHz for the output section of the circuit

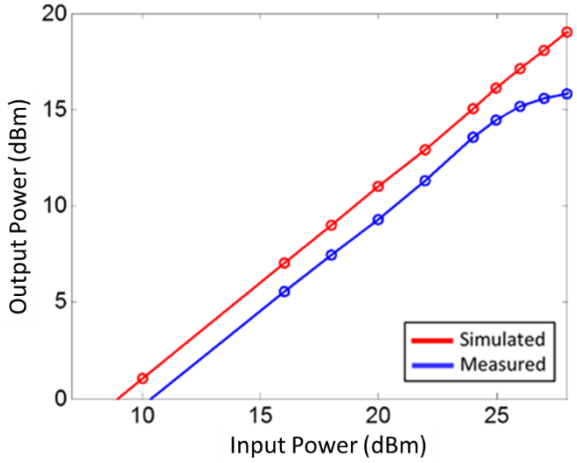

Figure 7.53 – Doubled frequency power level versus input power level

The compression in the measured result is due to the source amplifier reaching saturation.

7.6.4 Discussion of the performance of the shared resonator frequency doubler

It can be seen from Figure 7.48 that the power spectrum of the measured circuit closely matches the predicted band of the simulation. The measured spectrum shows a power level of around 3 dB lower than the simulation, a slightly larger bandwidth (approx 150 MHz), and a centre frequency shift upwards. This result is also mirrored in the conversion efficiency/insertion loss (Figure 7.49 and Figure 7.50), and the input return loss in Figure 7.52 shows the frequency shift also. The input power dependancy plot in Figure 7.53 shows that we are operating near the saturation limit of the output power of power amplifier, however that with an input power of +22 dBm we are still in its linear output region without a performance drop due to compression.

To explain this deviation from the simulated expectations, the manufactured circuit dimensions are examined. The design has a high demand on the tolerance for gaps between tracks and track widths. From Table 7.2 it can be seen that the smallest gap is only 50 μm wide, and this

is difficult to achieve with a printed circuit board manufacturing. A supplier was found that could meet this specification, but with a +/-25 µm tolerance.

Measuring the board with a powerful microscope it was found that the tracks on average were 55 µm narrower than specified, and the gaps were up to 20 µm wider than specified, as shown in Figure 7.54.

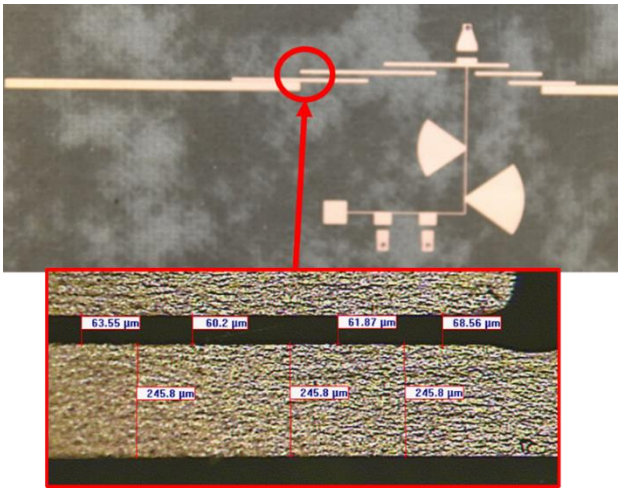

Figure 7.54 - Photo showing the manufactured track and gap size

However this error does not affect the circuit much as demonstrated below. Putting these measurements back into the model, the result in Figure 7.55 is obtained.

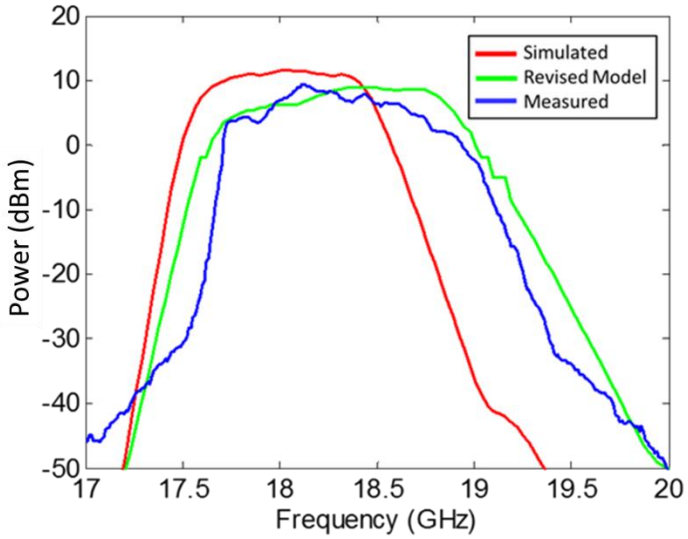

Figure 7.55 - Simulation results with manufactured circuit dimensions

Figure 7.55 shows that the revised model simulation has a similar shift in frequency, an increase in bandwidth, and a lowering of the output power and hence doubling efficiency. The upwards shift in frequency is what would be expected from a decrease in resonator length which has been measured in the manufactured circuit. Also the resonator width reduction has an effect which was illustrated in Figure 7.18. The effect on resonator width reduction also shifts the frequency upwards and alters the *Q* of the resonator, which in turn affects the bandwidth. The increases in gap widths are inconsitent with a bandwidth increase; increasing gaps between resonators generally lowers the filter passband performance while reducing the bandwidth. However, the revised model shows that the overall effect of the discrepancies in manufacturered dimensions explains the measured perfomance well.

7.6.5 Flexibility of the coupling matrix computed design

A major benefit of the coupling matrix approach to designing a diode frequency doubler is that once the work of profiling the couplings is done and the curve fits completed, there is a lot of flexibility in how the design is implemented. One example of this is that the number of resonators can be increased or decreased with no requirement for repeating any analysis work. Filter solutions can be obtained computationally for any number of resonators, as shown in Figure 7.56. It can be seen that to construct any of these solutions, only the *Q* and *K* computed requirements need to be met, and these have all been profiled already. It is just a simple matter of adding or removing resonators and reading the gap distances from the relevant graphs. If the new *Q*'s and *K*'s are difficult to obtain with the manufacturing process available, then the bandwidth can be adjusted to make the design easier to construct.

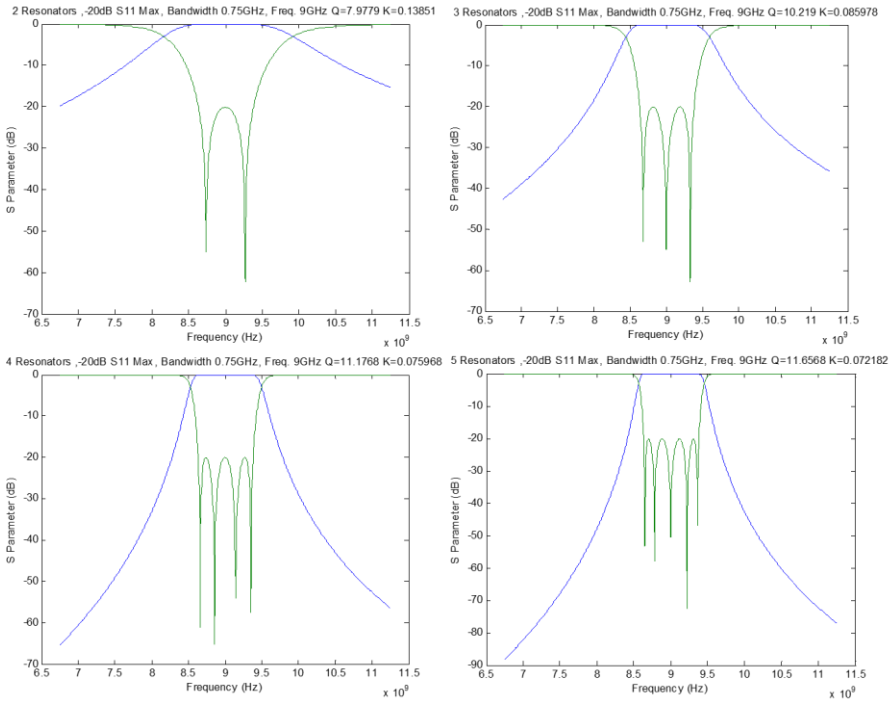

Figure 7.56 - 2,3,4 and 5 resonator coupling matrix responses, S_{11} *max* = -20 *dB.*

To demonstrate this two more circuits were constructed with just one and two resonators, as shown in the circuit layouts in Figure 7.57 and the one and two resonator circuits are shown in the photographs in Figure 7.62.

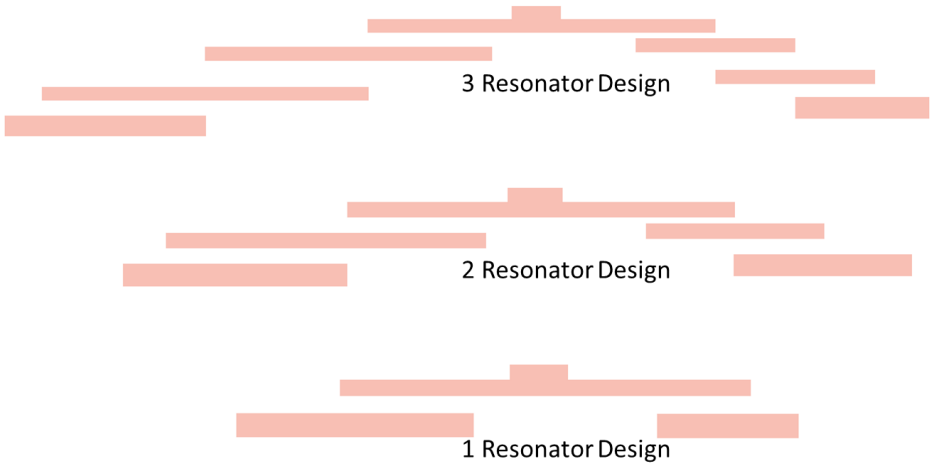

Figure 7.57 - Diode doubler circuits using 1, 2 and 3 resonators.
Bias circuit removed for clarity.

As an example, the design for the two resonator circuit will have the couplings shown in Figure 7.58, and the *Q* and *K* couplings can be computed from coupling matrix theory as shown in Figure 7.59 for the 9 GHz case.

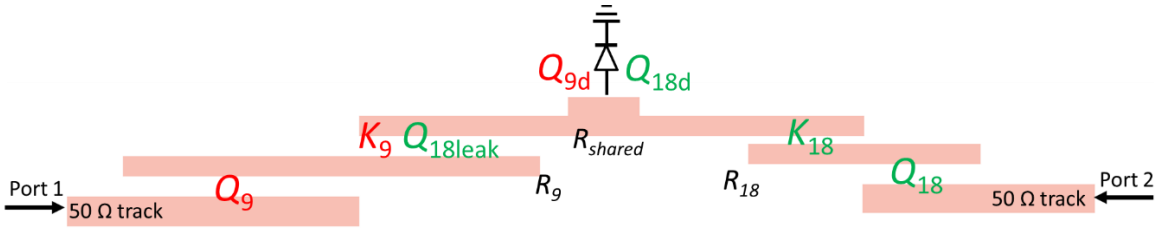

Figure 7.58 - Couplings for the two resonator circuit

It can be seen that the previous analysis helps in the design of this circuit as the coupling curves versus the gap widths are already known. As Q_{9d} was examined in the previous three resonator example, and the Q_9 gap to match this value is also known, all that is required is to calculate the coupling matrix for the internal coupling K_9.

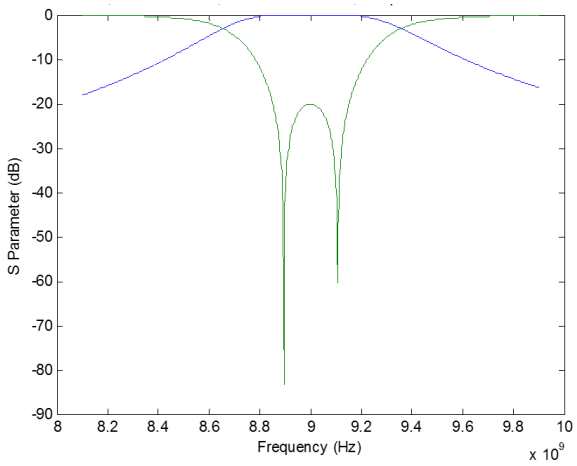

Figure 7.59 - Two resonator filter response. n=2, S_{11} max = -20 dB
Centre frequency = 9 GHz. Q = 19.94, K=0.055. BW = 0.3 GHz

It can be seen that the required K value is now 0.055. From the plot for $K_{9\text{-}2}$ in Figure 7.32 a gap of 0.5mm is required for the 9 GHz K coupling. To keep Q_{9d} at the previous value, the bandwidth is reduced to 0.3 GHz. The other couplings and gaps can be determined in a similar way.

The measured doubled power spectra of these three circuits are shown in Figure 7.60, which highlights the versatility in being able to trade off resonator number for sharpness of the frequency doubling band. The S_{11} responses of these circuits is shown in Figure 7.61.

It can be seen that by altering the number of resonators the drop off of the band is adjusted, as anticipated from the computed solutions. It should also be noted that due to the K_9 gap being less than 0.6 mm, there is an expected drop in frequency doubling performance of the two resonator circuit.

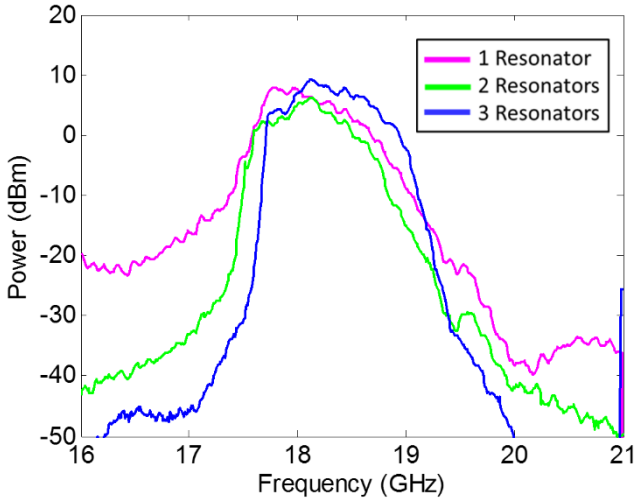

Figure 7.60 – Measured doubled frequency power spectrum of three circuits with different numbers of resonators.

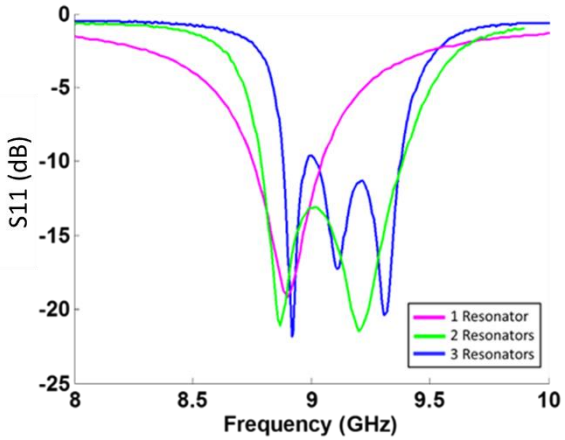

Figure 7.61 - Measured S_{11} performance of 1, 2 and 3 resonator circuits

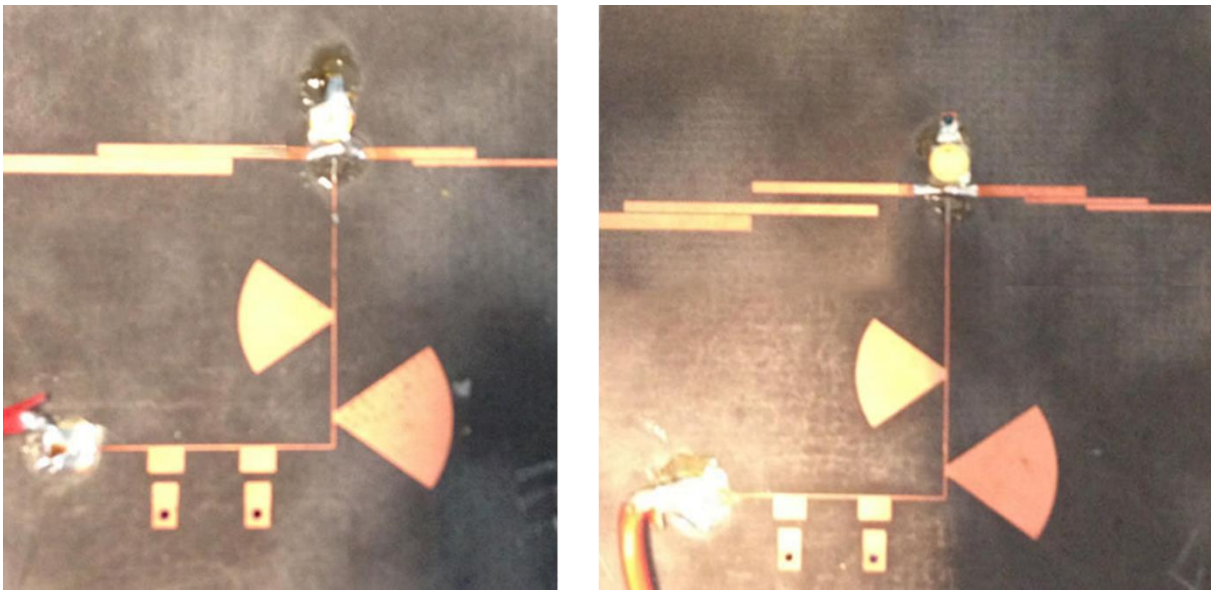

Figure 7.62- Photographs of the one and two resonator circuits

7.7 Conclusion

It has been shown that the coupling matrix method used for designing filters can be used with traditional techniques for diode frequency doubler design to produce an innovative, flexible, compact and integrated circuit solution. This method has been explained and demonstrated and the results meet expectations well. The problem of designing a circuit where there are complicated interactions between the input circuit, the active components, and the output circuit have been overcome with a controlled design process. The process that has been illustrated here, could be expanded to integrate other circuit types that are capable of being analysed by the coupling matrix design. It has been shown that the design can be modified easily by increasing or decreasing the number of resonators to vary the effect on the band drop off rate. This can be done with no need for further analysis as the resonator gaps can be set to values determined

computationally. The coupling matrix analysis also allows versatile control of the couplings and in the design in this chapter, it was used to great effect to select a value of bias that allowed a compromise between matched coupling, conversion efficiency and manufacturability as shown in section 7.5.5 and illustrated in Figure 7.37. A drawback of this design process is that choices of diode bias and resonator gaps will limit the bandwidth of the circuit which is effectively constrained by the best match filter configurations.

A comparison of the ‘design by optimiser’ shown in chapter 6 can be made with the design shown here, to see the benefits of the method in this chapter. The work contained in appendix 2 uses some of the analysis from this chapter to provide an alternative approach of diode doubler design using an impedance matching approach. This impedance matching approach is shown to be less accurate than the method shown in this chapter for reasons that the cross coupling between each half of the circuit is not taken into account. However, the impedance matching approach has the advantage that the impedances at the centre of the circuit are known, which is useful for many applications that require this information for matching purposes.

To compare the results of this chapter with commercial devices, we can see from Figure 7.50 that our frequency doubler circuit has a conversion loss of around 15 dB. Commercial devices typically quote conversion loss figures of 12 dB to 17 dB for a similar frequency of operation [6], showing that the work in this chapter, which was performed with a novel design process, is already competitive, and has the benefits of the flexibility of design of the input and output filters to suit a particular application.

A future step for this research, now that the design process and control of the couplings has been proven with microstrip, is to design a frequency doubling circuit using waveguide and waveguide resonators.

References

[1] Rogers Corporation. http://www.rogerscorp.com/

[2] MACOM Technology Solutions Inc. https://www.macom.com

[3] Agilent Advanced Design System[tm]. Keysight Technologies.

[4] J.B. Vinding, **Radial line Stubs as elements in strip line circuit**. NEREM record, 1967.

[5] R. Sorrentine and L Roselli, **A new simple and accurate formula for microstrip radial stub**. IEEE Microwave and Guided Wave Letters, 1992. Volume 2, issue 12, pages 480-482.

Chapter 8

Conclusions and Future Work

8.1 Conclusions

This thesis has shown that the terahertz region is ripe for exploitation and that technologies already exist to do this. However the costs and efforts required to employ existing techniques have meant the terahertz spectrum remains sparsely used. This thesis assists in the construction of terahertz circuit for communications in the following ways; (i) the demonstration of a low cost fabrication technique using SU-8 micromachining for the construction of terahertz circuits, and (ii) a versatile design method to handle communication circuit design which have complex interactions previously requiring optimisation techniques. This is demonstrated at a low frequency in a multiplier, but the concepts can be extended to waveguide circuits at terahertz frequencies.

This thesis has presented an example of a low cost construction method that could assist in manufacturing commercial quantities of practical terahertz devices. The 150 GHz SU-8 layered waveguide demonstrated in chapter 4 is an example of this. This waveguide will form a fundamental part of any terahertz system, and the measurements made with this waveguide section and E field plane bends shows that this method is acceptable for use in more complex designs.

The coupling matrix method has been shown here to be a very powerful and versatile tool for the radio frequency circuit designer. It has been shown that it provides a way for engineers to

match circuit stages without having to resort to impedance transformation methods, and allows complex analysis of multiple interacting stages within a circuit.

Techniques useful for diode doubler design, and the use of the coupling matrix method to integrate passive and active components have been developed and proven in chapters 5, 7 and appendix 2. Complex circuit interactions between the input and output have been analysed and controlled with a guided design process that can be applied to similar situations. The "good first attempt" result of these methods will reduce the simulation and optimisation effort required during the design process, and allows a more creative approach for engineers embarking on similar projects.

8.2 Future Work

The next step with the technologies and techniques developed in this thesis is to design a diode doubler circuit using waveguide resonators to construct integrated matched filters. This will further prove the methods of chapter 7. A future step would be to then design a terahertz frequency doubler circuit. SU-8 could be used for the circuit structure as resonating cavities can

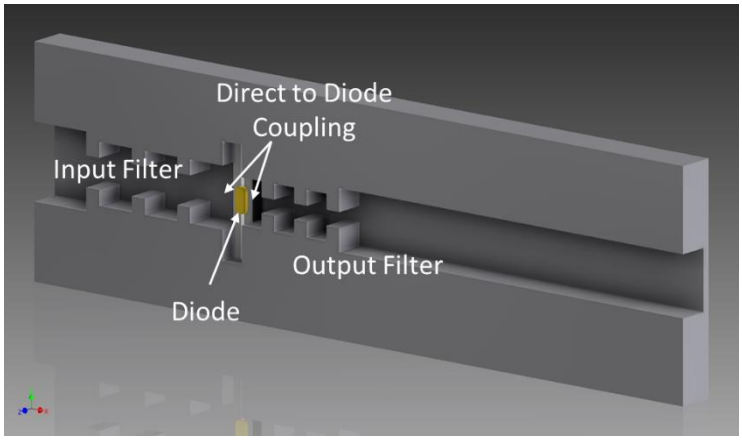

Figure 8.1 – Concept illustration highlighting the benefits of integrated filters, direct to device coupling and shared resonator cavities.

be precisely and easily fabricated to form the bandpass filters, and the active device can be coupled directly within the waveguide, potentially with no need for transition circuity, as shown in the concept illustration in Figure 8.1, which compared to a more conventional arrangement of Figure 8.2 highlights the benefits of using this design method.

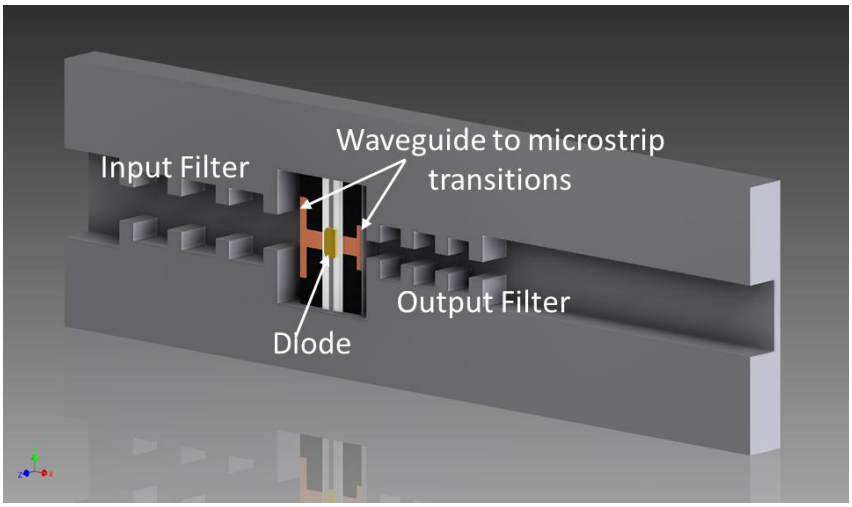

Figure 8.2 - Conventional waveguide mounted diode double with isolated filters and micro strip to waveguide transitions

This would produce a compact and potentially large scale / low cost solution to high frequency multiplication.

The terahertz receiver system concept illustrated in Figure 2.3 is therefore feasible, however experimentation is still required before the concept is proven to be satisfactory. Problems such as cross coupling between parts of the circuit due to gaps in the SU-8 layers in the system need to be addressed. The problem of how to mount active components and provide bias voltages to them within an SU-8 cavity would also benefit from further work. In the terahertz

context, the design principles should scale with frequency as long as substrates and waveguide manufacture can scale also. Terahertz non-linear devices however do not easily scale with frequency, and the new device technology breakthrough as shown in Chapter 2 are required to continue, especially as parasitic parameters quickly dominate as the frequency increases, and conversion efficiencies diminish.

There is still a lot of work to be done before terahertz applications are available at consumer prices, and components that operate in this region can be available off the shelf.

However, for the enterprising engineer, it is hoped that some of the work contained here can assist in the progress toward the use of terahertz frequencies, and inspire some creative minds to continue this work.

Appendix 1

Journal Paper:

Submillimetre Rectangular Waveguides based on SU-8 photoresist micromachining technology

Submillimetre Rectangular Waveguides based on SU-8 photoresist micromachining technology

David Glynn, Tianhao He, Jeff Powell, Yingtao Tian, Xiaobang Shang and Michael J. Lancaster
School of Electronic, Electrical and System Engineering
The University of Birmingham.

***Abstract*—Rectangular waveguides are fundamental structures for the transmission of signals at millimetre and submillimetre wavelengths. This paper describes the design and measured results for two rectangular waveguides based on layered SU-8 photoresist micromachining technology, with double-layer fabrication techniques to minimise the air gaps between layers. A brief description of the SU-8 photoresist micromachining procedure is given in the paper. One waveguide is demonstrated for the WR-3 band from 220 GHz to 325 GHz the other is for the WR-6 band 120 GHz to 170 GHz both are made of layered SU-8 with a 3 piece construction. Both waveguides have novel bends in order to connect to the measurement apparatus. The measured performance is presented and compared to conventional machined metal waveguide structures. The measured insertion loss for the SU-8 waveguides in both bands is better than 0.03 dB/mm.**

Keywords—waveguide; SU-8; micromachining

INTRODUCTION

The desire for ever higher frequency communication systems has made implementing even the simplest of components difficult as terahertz frequencies are approached. However, due to micromachining technologies, rectangular waveguide transmission lines and passive circuits are now accessible for frequencies at submillimetre wavelengths. Such micromachined circuits are also ideal conduits for integrating active components and with novel methods of matching, efficient high frequency systems can be constructed. One such circuit considered when initiating this research is the frequency multiplier. Multipliers are used as it is difficult to generate a local oscillator frequency high enough to mix with a high frequency target signal. Frequency multipliers typically utilise a nonlinear harmonic response to distort a lower frequency into a required harmonic multiple. The frequency spans of the two waveguides in this paper were chosen to coincide with an input and doubled output frequency range for such a multiplying circuit. Care was taken to design the waveguides using just five layers of SU-8 photo resist, so that the waveguides orientations would allow an input circuit of 150 GHz to connect to a future frequency doubler design, and the resultant 300 GHz frequency would utilise the second waveguide. Ninety degree E- plane or and H-plane bends were constructed to connect to test equipment, or potentially to other stages in a communication system.

I. WR-3 WAVEGUIDE DESIGN

The rectangular waveguide designed here is a standard WR-3 band waveguide with a cross-section size of a = 864 μm by b = 432 μm. The length of the waveguide is 15.95 mm to match previous waveguide circuits [1] and a novel bend is used to attach the waveguide to the measurement network analyser.

A device based on SU-8 pieces is easy to fabricate and is mechanically robust. It has a low insertion loss and good transmission coefficient for the specified operating frequency band. In this rectangular waveguide design, specifications for the transmission coefficient S_{21} are better than -20 dB for the whole WR-3 band. The WR-3 waveguide is built with 5 layers of SU-8 photoresist with each layer having a thickness of 288 μm. Three layers form the total thickness of 864 μm for the WR-3 waveguide internal dimensions with additional two layers for the top and bottom of the guide and to feed to the waveguide bends connecting the waveguide to the measurement apparatus as illustrated in Fig 1. The design of the waveguide bend is based on a similar previous structure in [1] and it is modified and configured to meet the dimension requirements of WR-3 waveguide. The waveguide bend is specified to be an H-plane.

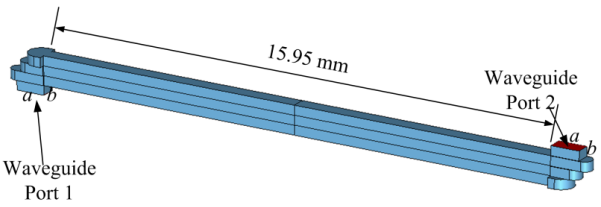

Fig. 1. 3D EM model for the WR-3 waveguide with bends. Here the inside of the metal waveguide is shown in blue and the layers are clearly seen.

II. WR-6 WAVEGUIDE DESIGN

The 150 GHz waveguide dimensions are derived from the WR-6 waveguide specification (a=1650 μm, b=830 μm), which covers the frequency range 110 GHz to 170 GHz. WR-6 was chosen for its centre frequency of 150 GHz, which would be useful in a 300 GHz communication system as part of the local oscillator multiplying circuit. However, because we are to construct the waveguide from layers of SU-8 photoresist which has a thickness of 288 μm per layer, we are restricted to using a multiple of 288 μm for one of its dimensions. The chosen implementation of the SU-8 photoresist layers is shown in Fig. 2, and we can see with just 5 layers that a close approximation to WR-6 can be made, where only the b dimension differs in our solution, with an increase of 34 μm (4%). A waveguide length of 15.95 mm was used.

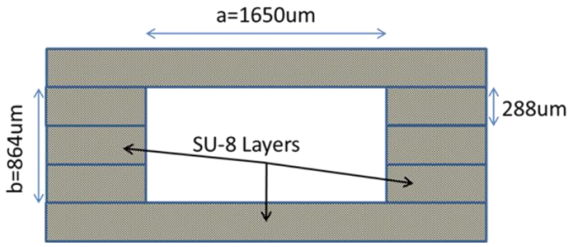

Fig. 2. Structure and Dimensions of 150 GHz waveguide.

The 150 GHz waveguide is to be constructed with 5 layers of SU-8 photoresist. Therefore the overall thickness of the device is 5 x 288 µm = 1440 µm. Two ninety degree E-plane bends are needed to allow the connection of test equipment. Fig. 3 shows the configuration of the bends and the waveguide test ports perpendicular to the waveguide. There was also an additional complication in that only WR-5 (a=1295.4 µm, b=677.7 µm) test heads were available for the Vector Network Analyser, so a conversion was required for this within the bend structure.

The bend was designed by constructing a simple parameterised staircase structure which widens slightly from the WR-5 test head orifice to that shown in Fig. 2. A simple optimisation software routine was used to adjust each step to find the best solution

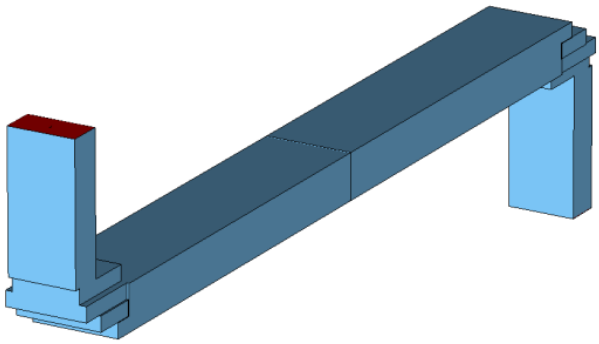

Fig. 3. 3D Model of 150 GHz Waveguide and bends.

III. Fabrication

Based on the CST waveguide bend model as shown in Fig. 1, the layout of the 5 SU-8 layers and their corresponding masks for micromachining photolithography are generated. There are five layers for the SU-8 waveguide and they are displayed in Fig. 4. As the whole structure is symmetrical to the centre point, the Layer 1 and Layer 5 are identical to the Layer 2 and Layer 4.

Both WR-3 and the WR-6 waveguides consist of 5 SU-8 layers, with each layer having a thickness of 288 µm. The fabrication integrates the top and bottom two layers with a joined double layer fabrication technique, thus making three standalone SU-8 pieces instead of 5 individual pieces. The top and bottom joined pieces are of same 576 µm thickness and the middle piece is 288 µm. Thick SU-8 photoresist can be used as the structural material for constructing waveguides and is very cost effective, having a good fabrication repeatability and requires low facility investment in comparison with the precision CNC milling. All the procedures are performed in the in-house clean room facilities and the metallisation stage is completed in-house also. The fabrication process for the SU-8 pieces is detailed in [2].

Two waveguide circuits for the WR-3 band and one for the WR-6 band are fabricated, and a photo of the WR-3 waveguide circuit is shown in Fig. 5. The SU-8 waveguide device is fully metallised with silver on the surface of the SU-8 pieces. Each of the fabricated SU-8 pieces are assembled together with clamping brass plates reducing possible losses due to the air gaps. The main part of the photograph in Fig. 5 is the device clamped by brass plates occupies a volume of 48 mm × 24 mm × 8 mm.

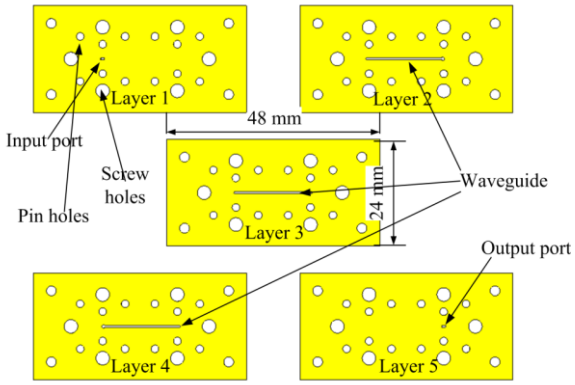

Fig. 4. The SU-8 layers for the WR-3 waveguide.

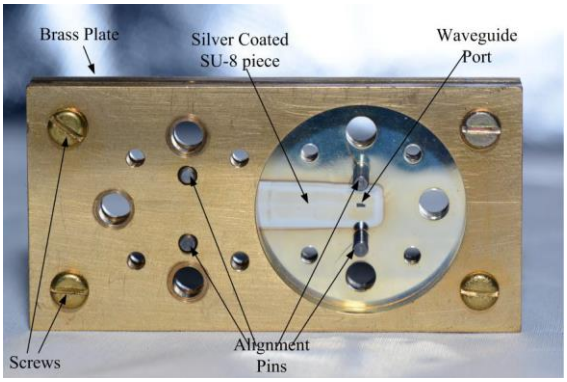

Fig. 5. The photograph shows a fabricated and assembled device WR-3 waveguide.

IV. Measurements

Fig. 6 shows the measurement configuration of the fabricated and assembled WR-3 band waveguide circuit carried out on the Agilent E8361A Vector Network Analyser with a WR-3 OML band extender T/R module at test port 1 and a receiving only T-module at port 2. Enhanced response calibrations are done before the measurements. Standard UG-387 waveguide flanges are used as the interfaces for the connection from WR-3 waveguide to the measurement ports.

Screws and alignment pins are fastened to minimise the reflection, leakage and loss from the flanges.

V. WR-3 Waveguide Results

Two WR-3 band waveguide circuits are made in the in-house clean room, and both have been tested and are illustrated in Fig. 7 for the insertion loss S_{21} and in Fig. 8 for input return loss S_{11}. One waveguide has the measured insertion loss of 2 dB to 1 dB over the tested frequency bandwidth from 220 GHz to 325 GHz and the other waveguide has the insertion loss of 0.5 dB over the main frequencies. Both measurements include the effect of the bends. In terms of the return loss, one waveguide is tested to have at least 15 dB over the frequency band from 220 GHz to 310 GHz and best of 20 dB at 300 GHz while the other waveguide is tested to have average loss of 10 dB over the whole bandwidth and has the best response of 20 dB at 230 GHz.

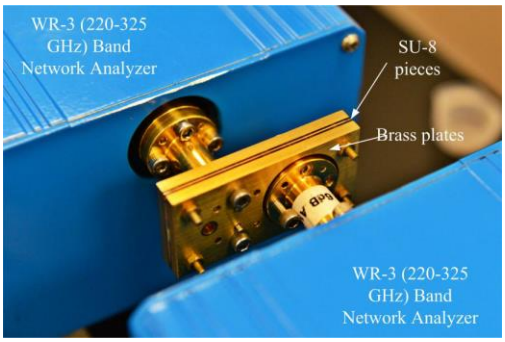

Fig. 6. The WR-3 waveguide under test with a Network Analyser.

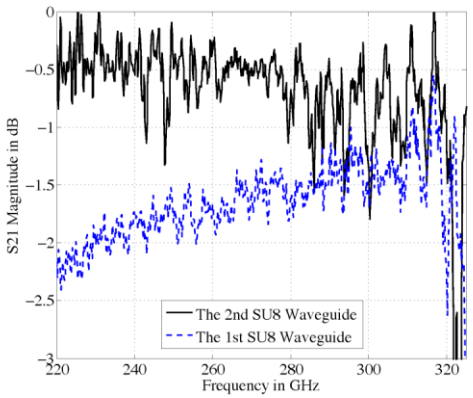

Fig. 7. The measurement results for the two fabricated results in S_{21}

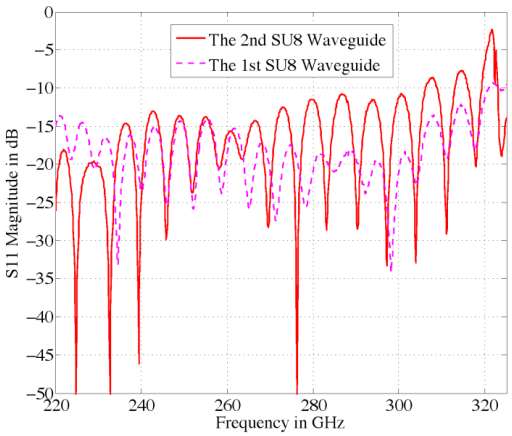

Fig. 8. The measurement results for the two fabricated results in S_{11}

VI. WR-6 Waveguide Results

The 150 GHz waveguide was tested using the Agilent E8361A Vector Network Analyser with a pair of OML WR-5 heads (T/R module at test port 1 and a receiving only T-module at port 2), covering the range from 140 GHz to 220 GHz. The designed range is from 120 GHz to 170 GHz, so we can only show measured results from 140 GHz upwards, as shown in Fig. 9 and 10. The loss per mm is in shown in Fig. 11. S_{11} follows the simulated results well with a return loss better than 12 dB across the measured band, and an average return loss of 24 dB. The S_{21} result shows that the losses are better than 0.034 dB/mm across the band, with an average loss of 0.011 dB/mm.

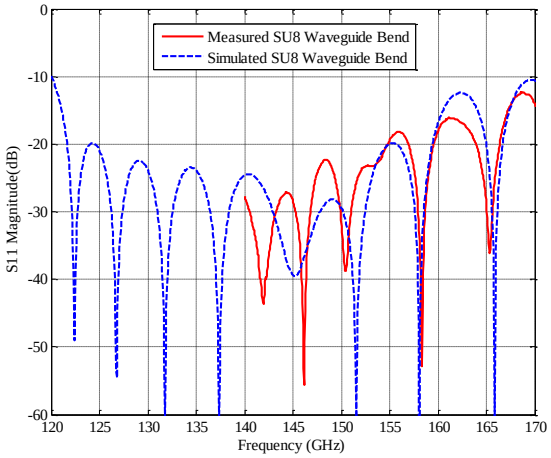

Fig. 9. S_{11} Results of 150 GHz waveguide

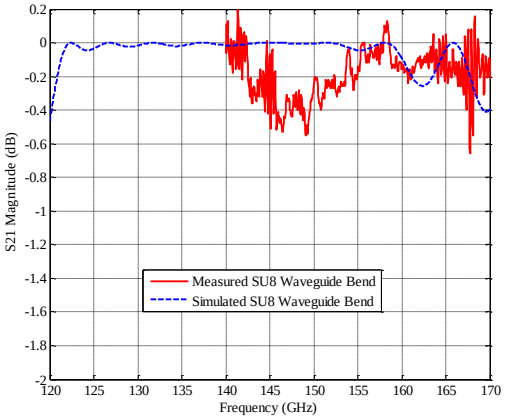

Fig. 10. S_{21} Results of 150 GHz waveguide

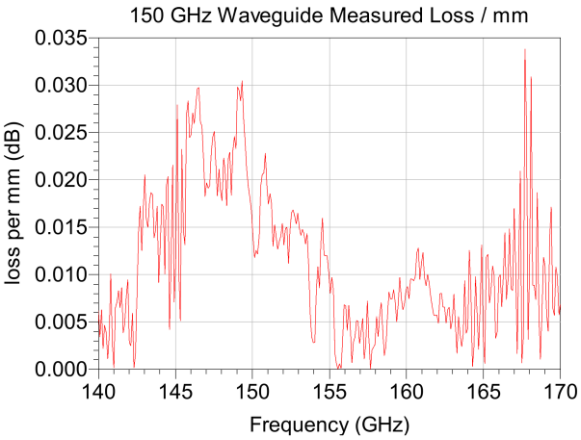

Fig. 11. Insertion Loss per mm for 150 GHz waveguide

CONCLUSION

We have shown it is possible to design and fabricate two fit for purpose waveguides from 5 layers of SU-8 photoresist to operate at the WR-3 and WR-6 frequency bands, and also have good ninety degree bends to allow connection to test fixtures or other circuit stages. These would be ideal conduits for a future communication system or its sub circuits, such as a frequency multiplier.

REFERENCES

[1] X. Shang, ML Ke, Y. Wang, and MJ Lancaster. Micromachined wr-3 waveguide filter with embedded bends. Electronics Letters, 47(9):545–547, 2011.

[2] Yingtao Tian, Xiaobang Shang, and Michael J. Lancaster. Fabrication of multi-layered su8 structure for terahertz waveguide with ultralow transmission loss. Journal of Micro/Nanolithography, MEMS, and MOEMS, 13(1):013002–013002, 2014.10.1117/1.JMM.13.1.013002.

Appendix 2

Coupling Matrix Impedance Matching Method

A2.1 Introduction

Chapter 7 showed the process of designing a diode doubler using the coupling matrix method. It showed how to match the external *Q* of a resonator with a diode mounted on it at both the fundamental and doubled frequencies, to the external *Q* of two filters. This created an integrated filter and diode doubler solution. In this appendix an alternative approach is proposed that also uses coupling matrix theory to design a diode doubler. It will be shown that a set of filter section solutions generated computationally can be characterised by their impedance. As there are two ideal matching impedances required by the diode for optimum power transfer at both the fundamental and second harmonic frequencies which can be determined as shown in chapter 5, the set of filter impedance solutions can be used to select a suitable one for best match.

It was shown in chapter 3 how to design coupled resonator filters using the coupling matrix method. That chapter showed that by profiling the internal and external coupling curves for a sweep of resonator couplings (physical gaps in the case of microstrip resonators), that a filter design can be determined. This is developed further in this section and also the fact that there is a **different filter solution for every bandwidth** with the S_{11} specification, number of resonators and centre frequency fixed. The practical limit on the number of filter solutions is the physical limitation of the dimensions of the coupling elements, which for microstrip circuits this is generally the minimum distance between tracks, track widths and the resonator *Q*'s limited by the substrate modes.

This is demonstrated by looking at the parameters that are required for the coupling matrix response. Figure A2.1 shows a typical three pole filter solution as determined in chapter 4. The design parameters are a S_{11} of -20dB, 9 GHz centre frequency and a bandwidth of 0.25GHz.

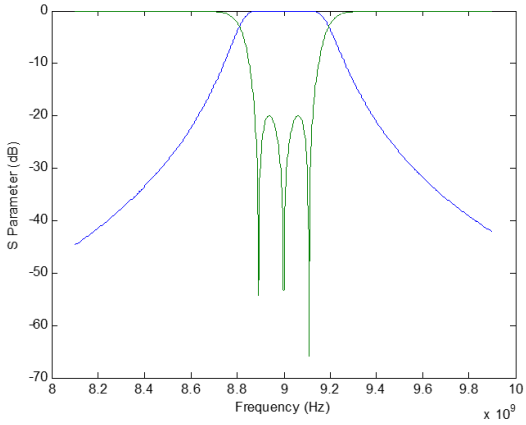

Figure A2.1 – Coupling matrix response for a 3 pole 0.25 GHz bandwidth filter, S_{11} max = -20 dB, K= 0.029, Q=30.65

The internal K and external Q couplings required in this example are 0.029 and 30.65 respectively, and as previously shown, these values are to be used to set resonator spacing to create the filter response shown. If the design parameters are kept the same, but the bandwidth is increased to 0.5GHz, the plot in Figure A2.2 is obtained.

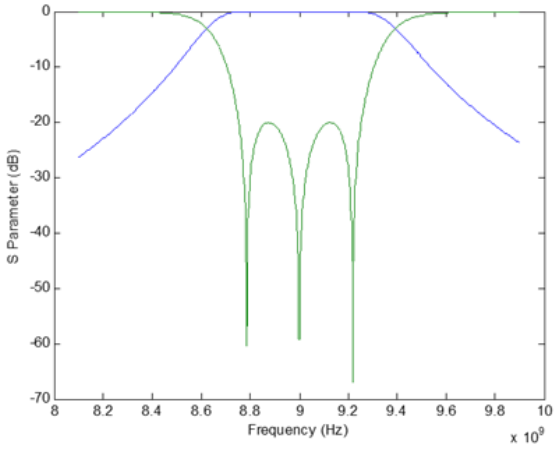

Figure A2.2 – Coupling matrix response for a 3 pole 0.5 GHz bandwidth filter, S_{11} max = -20 dB, K= 0.057, Q=15.33

From Figure A2.2, it can be seen that the internal K and external Q resonance requirements are 0.057 and 15.33 respectively, corresponding to a different filter gap configuration to meet the different bandwidth requirement.

If this exercise is repeated for a range of bandwidths, it can be seen that there will be a continuous set of filter solutions as shown in Figure A2.3.

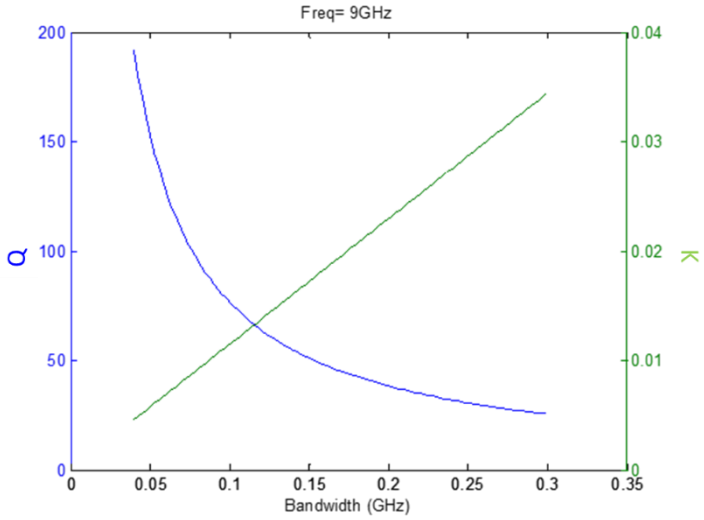

Figure A2.3 - Plot showing how Q and K varies for a range of filter bandwidths

In Figure A2.3, the blue curve shows the external coupling *Q* and the green line shows the internal coupling *K* for each bandwidth along the *x* axis.

To further illustrate this, a dynamic simulation (explained in more detail in the next section) can be created to construct a parameterised filter model where the internal and external coupling gaps can be set by values derived from the curves in Figure A2.3.

A2.2 Dynamic Bandwidth Varying Filter Simulation

A microstrip coupled parallel line bandpass filter simulation was constructed, as shown in igure A2.4. The gaps denoted d_1 to d_4 were parameterised within the simulation [1] and are to be driven by values determined by the computational method outlined above.

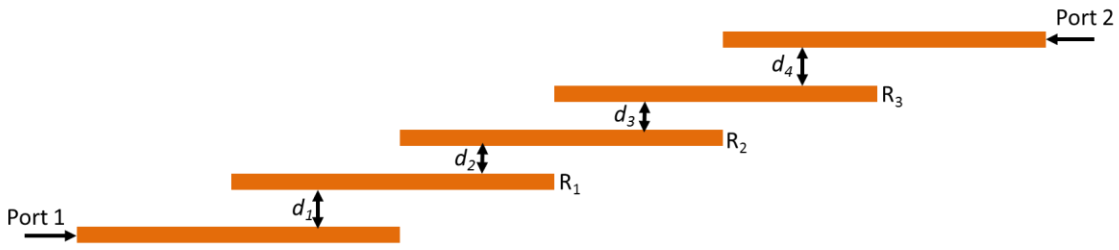

Figure A2.4 - Microstrip Coupled resonator bandpass filter

Internal and external couplings (*K* and *Q*) versus gap distance curves from the above circuit simulation are determined in the same way as described in chapter 3 and demonstrated in chapter 4. These two plots for *K* and *Q* are then curve fitted to obtain two equations that will be used by

the simulation to determine the physical gaps required for each filter solution, as detailed in the rest of this section. The curve fit plots for *K* and *Q* are shown in Figure A2.5.

It can be seen that a good fit for these curves is a power series, with the resultant curve fit equation is in the form:

$$f(x) = ax^b + c \qquad \text{A2.1}$$

Where *a, b* and *c* are the curve fit constants and *f(x)* is the physical gap and *x* is the computed internal or external coupling value.

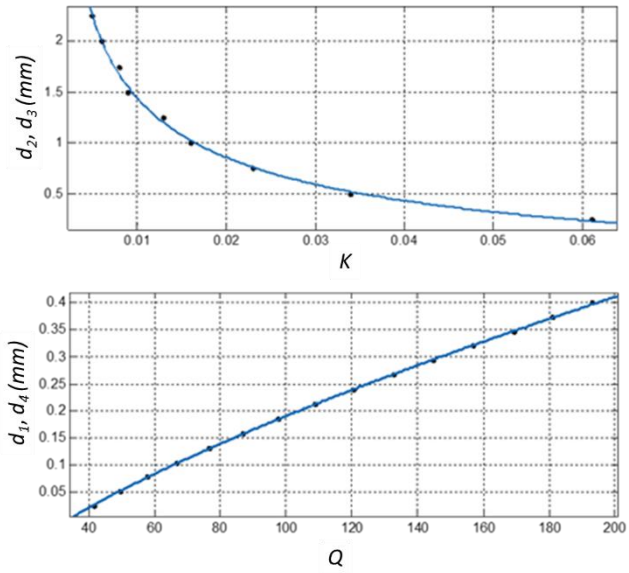

Figure A2.5 - Curve fitted plots showing how internal and external couplings vary with physical gap

The range of *Q* and *K* values depicted in the above figure along with the curve fit power series can be used to produce a filter solution for each bandwidth point. Table A2.1 shows a section of a

lookup table produced computationally, with each bandwidth value having an associated *Q* and *K* value. All of the other filter parameters (S_{11} response, poles and centre frequency) remain fixed,

Table A2.1 – Look up data for filter internal and external coupling values for each bandwidth.

(S_{11} max = -20 dB, *n*=3)

Index	*Q*	*K*	Bandwidth (GHz)
0	191.6	0.0046	0.0800
1	175.6	0.0050	0.0883
2	162.1	0.0054	0.0966
3	150.5	0.0058	0.1048
4	140.5	0.0063	0.1131
5	131.7	0.0067	0.1214
…	…	…	…

A simulation [1] can then be set up to sweep through this data list and the physical gaps determined using the following equations:

$$d_{1,}d_4 = a_q Q^{b_q} + c_q \qquad \text{A2.2}$$

$$d_{2,}d_3 = a_k K^{b_k} + c_k \qquad \text{A2.3}$$

Where d_1 and d_4 are the physical external coupling gaps in mm, *Q* is the computed *Q* value, a_q, b_q and c_q are the curve fit coefficients for the *Q* versus physical gap curve, and d_2 and d_3 are the physical external coupling gap in mm, *K* is the computed *K* value, a_k, b_k and c_k are the curve fit coefficients for the *K* versus physical gap curve.

Some results of this simulation are shown in Figure A2.*6* which shows the unoptimised filter s parameters S_{21} and S_{11} for 4 points from the bandwidth lookup table A2.1. It can already be seen that 4 reasonable filter solutions are produced with varying bandwidths as expected.

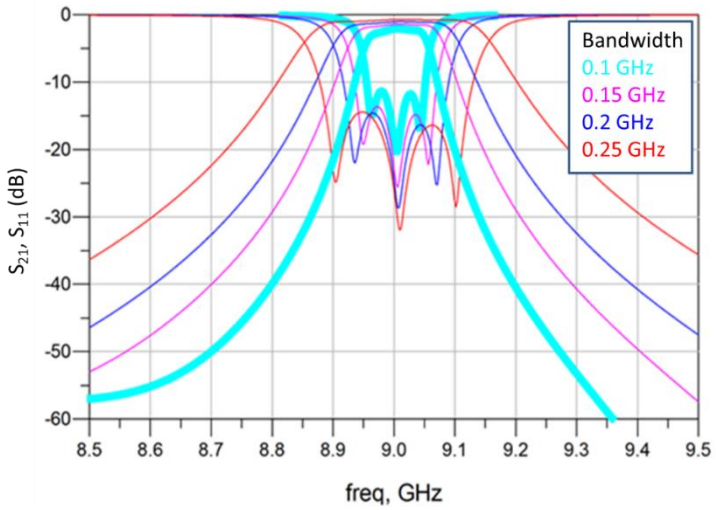

Figure A2.6 – Results of bandpass filter *Q* and *K* values in the dynamic simulation (solutions are unoptimised)

While only 4 solutions are shown here for clarity, it should be clear that many hundreds of solutions can be easily produced by this method.

The next step is to characterize all these solutions to observe how the impedance varies in a section of the filter. To do this the parts of the filter that will be used in the doubling circuit are analysed, as shown in Figure A2.7.

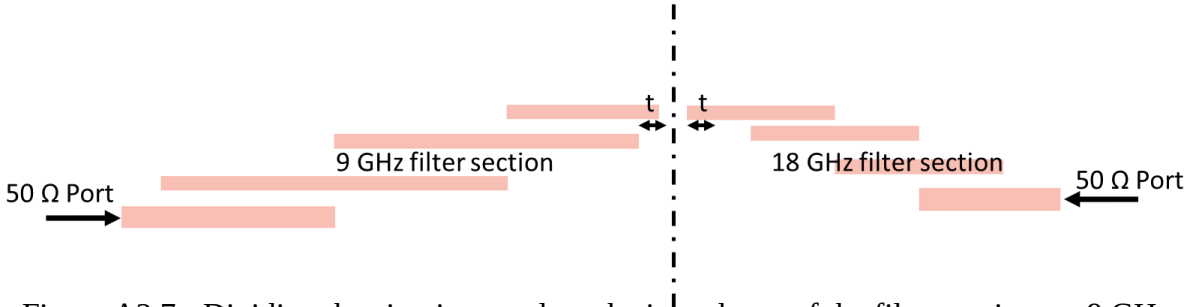

Figure A2.7 - Dividing the circuit to analyse the impedance of the filter sections at 9 GHz and 18 GHz

Figure A2.7 shows two simulation circuits, one for the 9 GHz filter section whose gaps were determined by the *Q* and *K* look up tables and curve fitting to the profiled *Q* versus gap, and *K* versus gap plots in Figure A2.5, and one for the 18 GHz filter section also. The impedances seen at the dotted line are to be manipulated to meet the impedances calculated by the load//source pull method outlined in chapter 6 so that the diode will be well matched to the filter sections.

To visualize this, the range of filter solutions versus bandwidth (*s*) can be plotted on a Smith chart to see how the impedance varies for each bandwidth solution, as shown in Figure A2.8. Here, *s* denotes the filter solutions versus bandwidth, and *t* is the effect of changing the length of the track *t* shown in Figure A2.7.

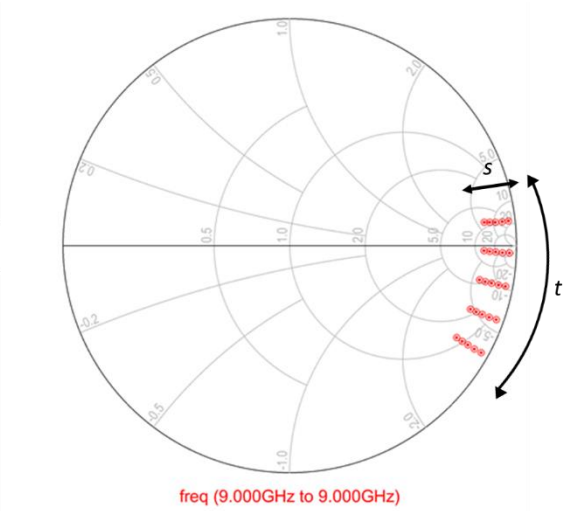

Figure A2.8 - Impedance plot of 9 GHz bandpass filter
solutions for each bandwidth point (*s*) and track length (*t*)

Considering each side of the circuit in turn, it can be seen that by changing the bandwidth of the filter solutions and the length of the track *t*, that the impedance applied to the diode can be adjusted. It was shown in chapter 6 how to obtain the optimum impedance value for matching to the diode, and the efficiency contours for the diode used for the doubler circuit is plotted in Figure A2.9.

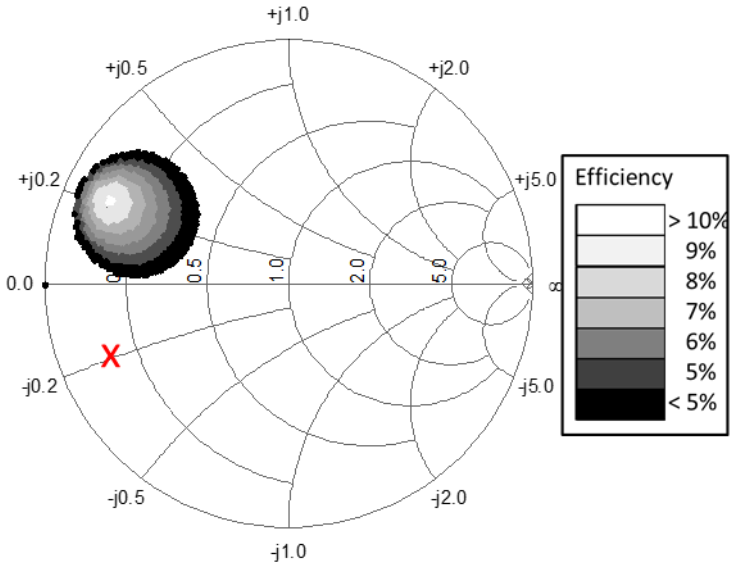

Figure A2.9 - Frequency doubling efficiency contours for diode source pull at 9 GHz. Red x marks the conjugate peak Z=9-j10**Ω**.

The conjugate of the impedance at the efficiency point has been marked with a red x in Figure A2.9 to denote the impedance the filter section should meet. It can be seen that for a solution in Figure A2.8 to reach the target point in Figure A2.9 the length of the track *t* will have to be adjusted, and then the correct bandwidth solution shall be selected to fine tune the matching.

The same can be done for the 18 GHz side of the circuit, with the solutions plotted in Figure A2.10 and the efficiency contours and target impedance in Figure A2.11. While considering the 18 GHz side of the circuit, the 9 GHz side has the optimum matching impedance applied to ensure the analysis is done at the peak frequency doubling efficiency.

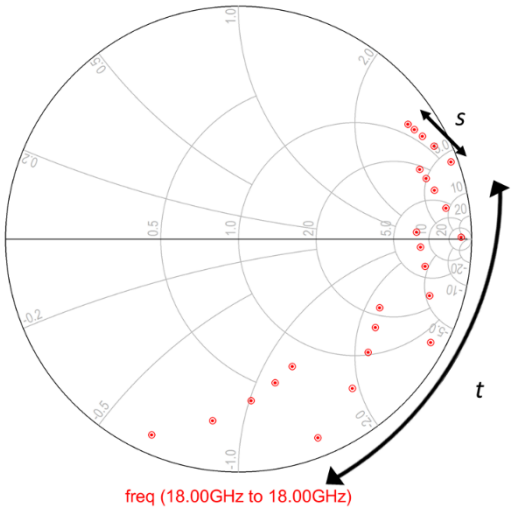

Figure A2.10 - Impedance plot of 18 GHz bandpass filter solutions *s*

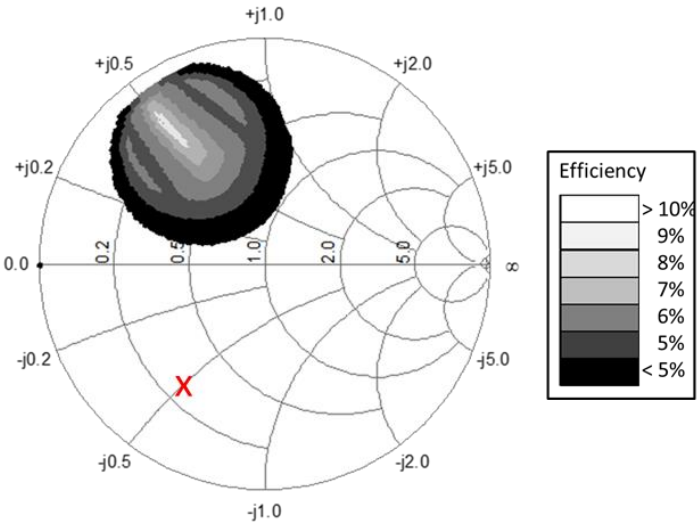

Figure A2.11 - Frequency doubling efficiency contours for diode load pull at 18 GHz. Red x marks the conjugate peak Z=13.5-j25$\boldsymbol{\Omega}$.

So using this analysis and selecting 9 GHz and 18 GHz filter solutions that will match impedance to the diode as closely as possible, the circuit shown in Figure A2.12 was constructed, with its dimensions shown in table A2.2. Optimisation is used at this stage as the filter responses as shown in Figure A2.*6* are not perfect and require some fine tuning. Table A2.2 shows the pre and post fine tuning values and it can be seen that only a few small changes of some dimensions was required.

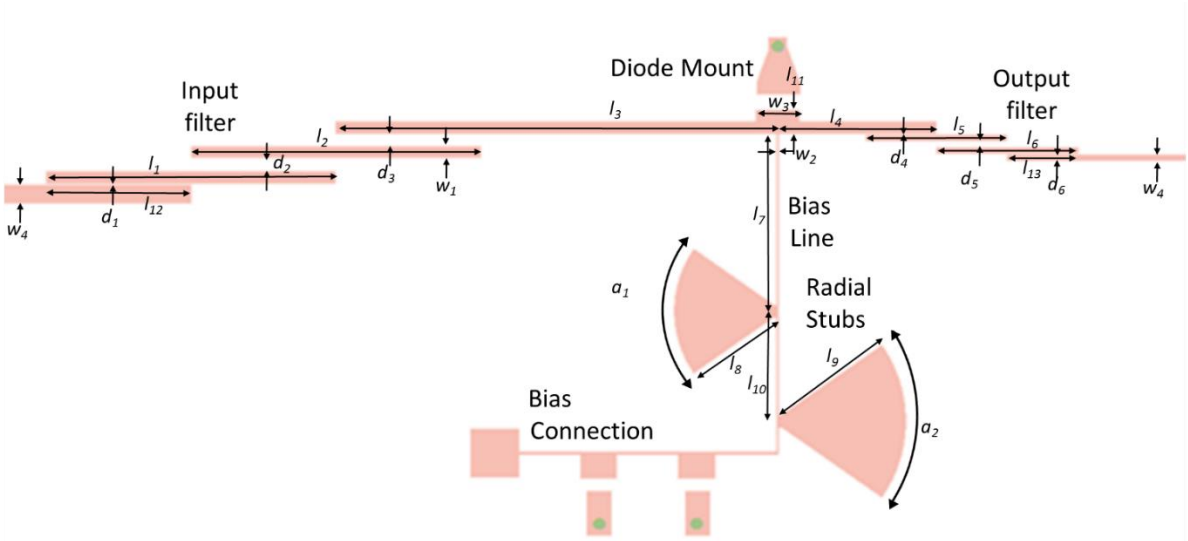

Figure A2.12 - Impedance matching coupling matrix diode frequency doubler layout

Table A2.2 – Diode doubler dimensions

Circuit Parameter	Initial Value	Opt. Value	Unit		Circuit Parameter	Initial Value	Opt. Value	Unit
d_1	0.15	0.09	mm		l_1	12	12.154	mm
d_2	0.55	0.55	mm		l_2	12	12.134	mm
d_3	0.9	0.912	mm		l_3	17.0	17.01	mm
d_4	0.2	0.2	mm		l_4	5.5	5.522	mm
d_5	0.65	0.63	mm		l_5	7.78	7.78	mm
d_6	0.1	0.1	mm		l_6	7.78	7.78	mm
a_1	70	70	deg		l_7	7	7	mm
a_2	70	70	deg		l_8	4	4	mm
w_1	0.5	0.5	mm		l_9	5	5	mm
w_2	0.1	0.1	mm		l_{10}	4	4	mm
w_3	1.778	1.778	mm		l_{11}	0.47	0.47	mm
w_4	0.744	0.744	mm		l_{12}	6.0	6.077	mm
					l_{13}	1.445	1.445	mm

The impedances of the 9 GHz and 18 GHz filter sections are hardly affected from the values shown in Figure A2.9 and Figure A2.11 after the filter optimisation has been performed. The optimsation target was for peak frequency doubling efficiency over a target bandwidth of 1 GHz centred on a fundamental input frequency of 9 GHz and a 22 dBm input power.

A photograph of the constructed circuit is shown in Figure A2.13. A drawback of this design shown in the photograph is that the diode mount track is long for this design to try and get the impedance of the filters to the conjugate points. This extra length has meant that the circuit is no longer able to fit in the universal test fixture, and SMA connectors have had to be fitted for the measurement.

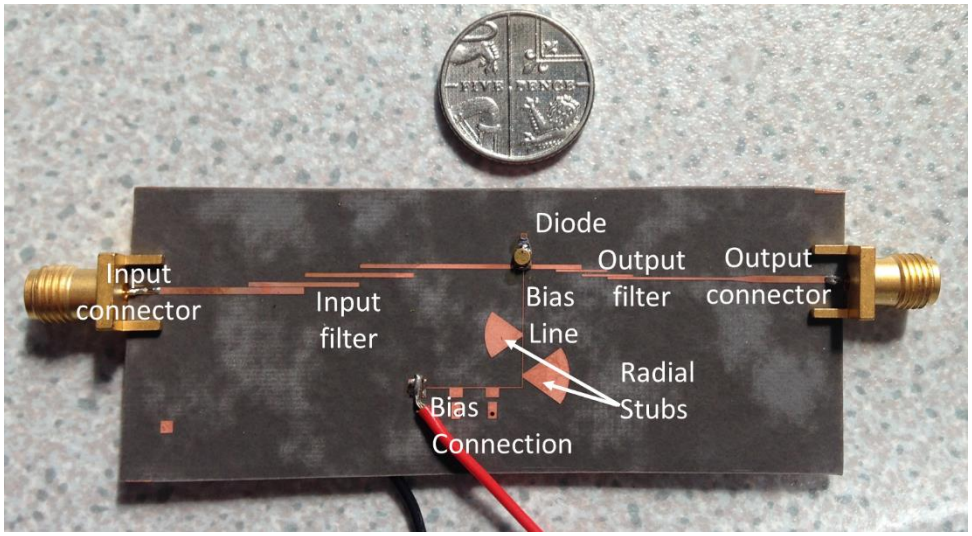

Figure A2.13 - Photograph of the impedance matched coupling matrix diode frequency doubler

The circuit was tested for its doubling efficiency in the same way as the circuit in Chapter 7, and the results are plotted in Figure A2.14, Figure A2.15 and Figure A2.16.

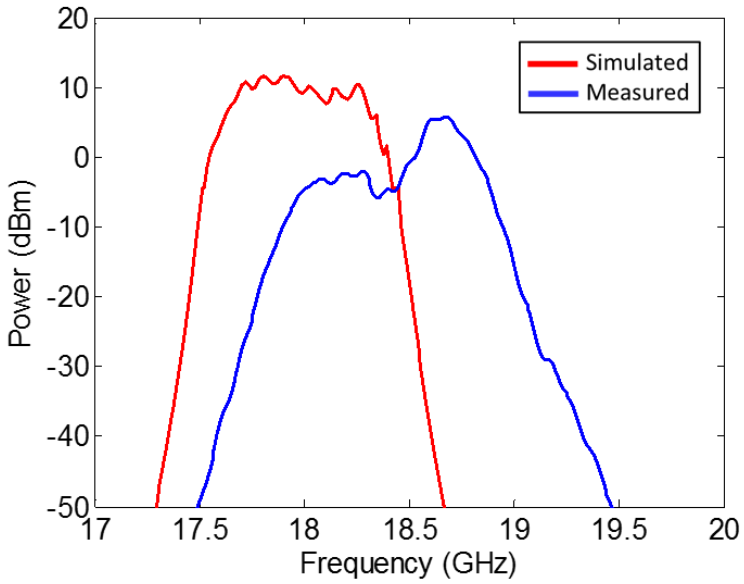

Figure A2.14 - Comparison of simulated and fabricated second harmonic power output of the diode doubler

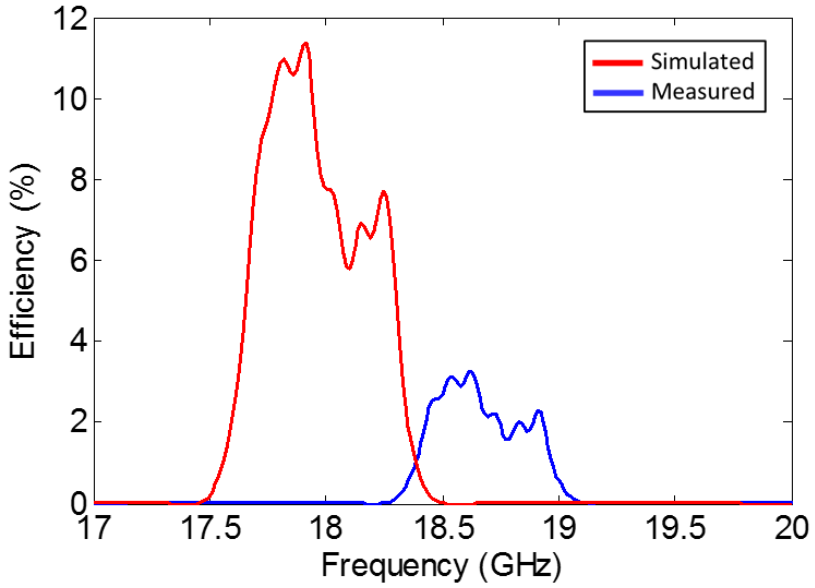

Figure A2.15 - Efficiency of the simulated and fabricated diode frequency doubler

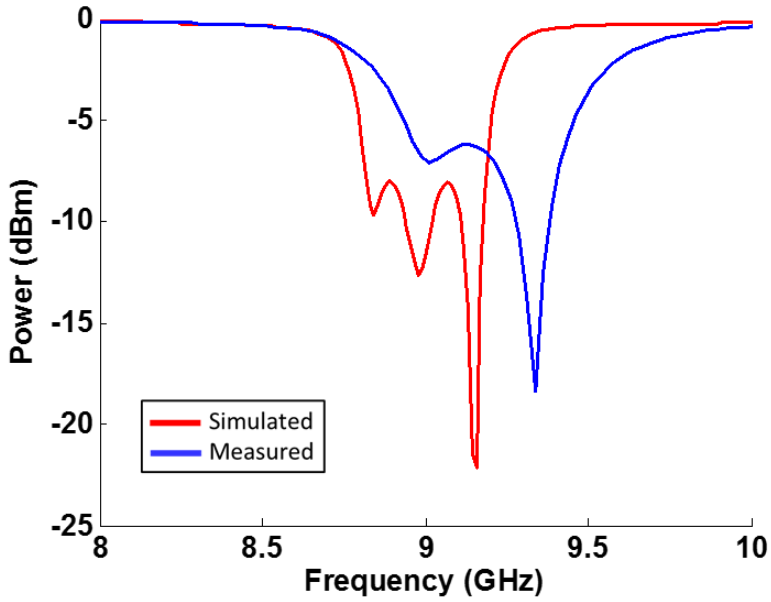

Figure A2.16 - S_{11} response of simulated and measured circuit

It can be seen from the above results that the performance, while not being as good as the result presented in the Chapter 7, is still useable as a diode doubler circuit. The use of the SMA connectors and the manufacturing dimension discrepancies will also factor in the observed result. What this method of doubler design does not take into account is the interaction between the filters from both sides of the circuit in the same way as the design from Chapter 7. While this design finds a matched solution, both sides of the circuit were designed in isolation. This method can therefore not fully account for any 9 GHz interactions with the 18 GHz side of the circuit, and vice versa. Energy is inevitably lost due to coupling mechanisms not accounted for in this impedance matching method, and explains the differences in results. However, this result is included to illustrate the method of using coupling matrix generated solutions to find a desirable impedance solution.

A2.3 Conclusion

This appendix has shown an alternative method of using coupling matrix theory to design circuits that require matched solutions. It demonstrates a versatile method of producing circuit solutions that can be characterised for their impedance, bandwidth or physical properties, allowing the designer an extra tool for innovation.

References

[1] Agilent Advanced Design System[tm]. Keysight Technologies. http://www.keysight.com/

Appendix 3

Curve fit details for Chapter 7

This appendix contains the values of the curve fit coefficients used in Chapter 7, along with reports on the accuracy of the curve fits. The curve fits were performed using Matlab [i] curve fitting tool, 'cftool' using data from simulations as stated in the chapter itself. Table 1 contains the curve fit coefficients quoted in the chapter and used in the matlab software to produce the plots for the resonator gaps.

Table A3.1 – List of Curve Fit Coefficients used in Chapter 7

Coeff.	Value		Coeff.	Value		Coeff.	Value
a_{9a}	0.8786		a_{9c}	0.07719		b_{18d}	-0.1748
b_{9a},	-1		b_{9c}	-0.4688		c_{18d}	-0.3695
a_{18a}	0.8786		c_{9c}	-0.05152		a_{9d}	140.3
b_{18a}	-1		a_{18c}	0.05743		b_{9d}	115.1
a_{9b}	0.06046		b_{18c}	-1.649		c_{9d}	4.035
b_{9b}	-4.839		c_{18c}	7.299		a_{9e}	0.1948
c_{9b}	-6.777		a_{18d}	0.3696		b_{9e}	-0.2288
						c_{9e}	-0.1811

The curve and fit measures are listed in Figure A3.1, Figure A3.2, Figure A3.3, Figure A3.4, Figure A3.5 and Figure A3.6 below.

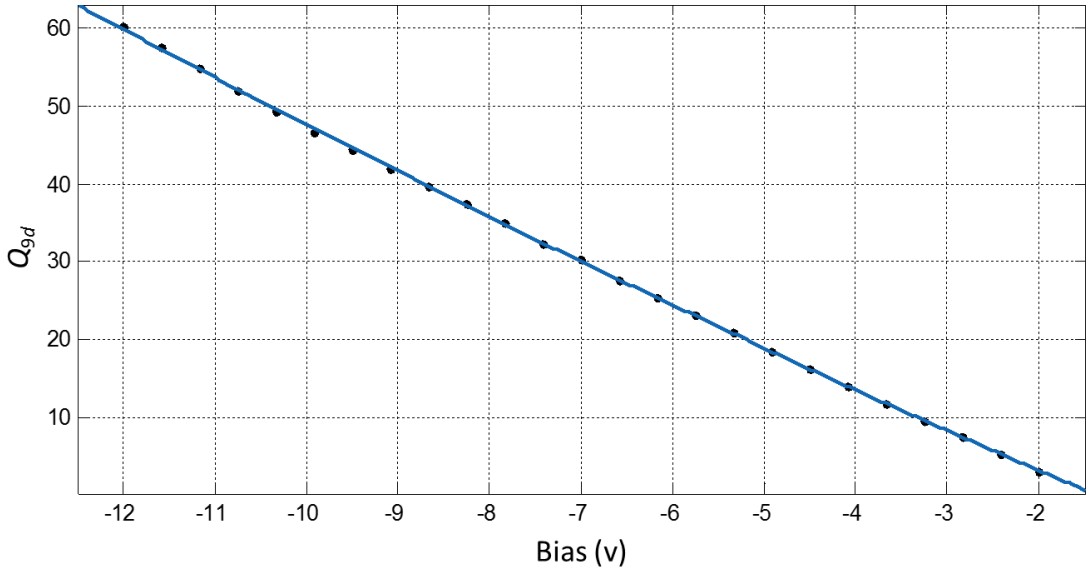

Figure A3.1 Curve fit plot for bias versus Q_{9d}

Matlab goodness of fit: SSE: 0.7603, R-square: 0.9999. RMSE: 0.1859

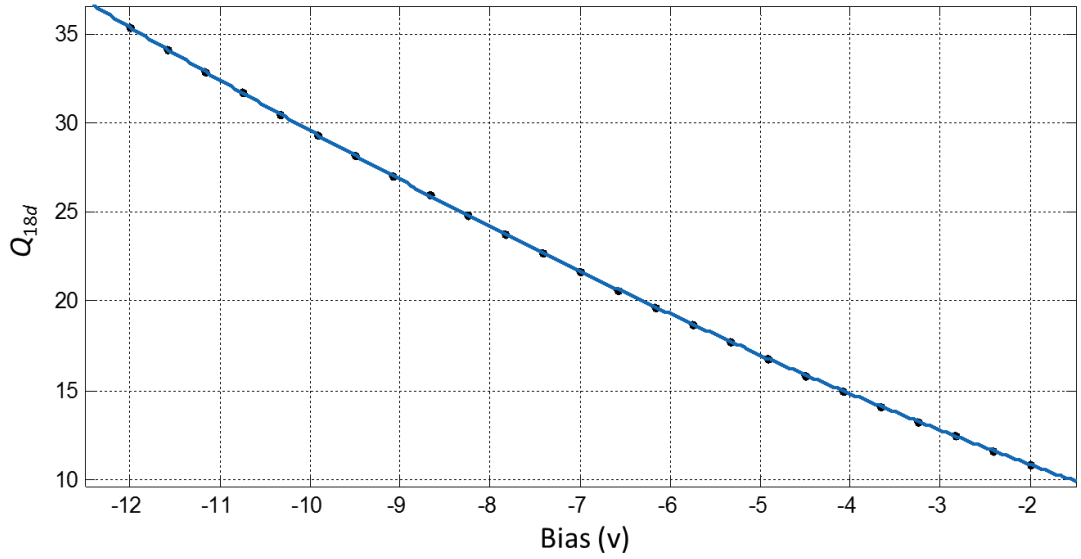

Figure A3.2 Curve fit plot for bias versus Q_{9d}

Matlab goodness of fit: SSE: 0.010873, R-square: 1. RMSE: 0.02223

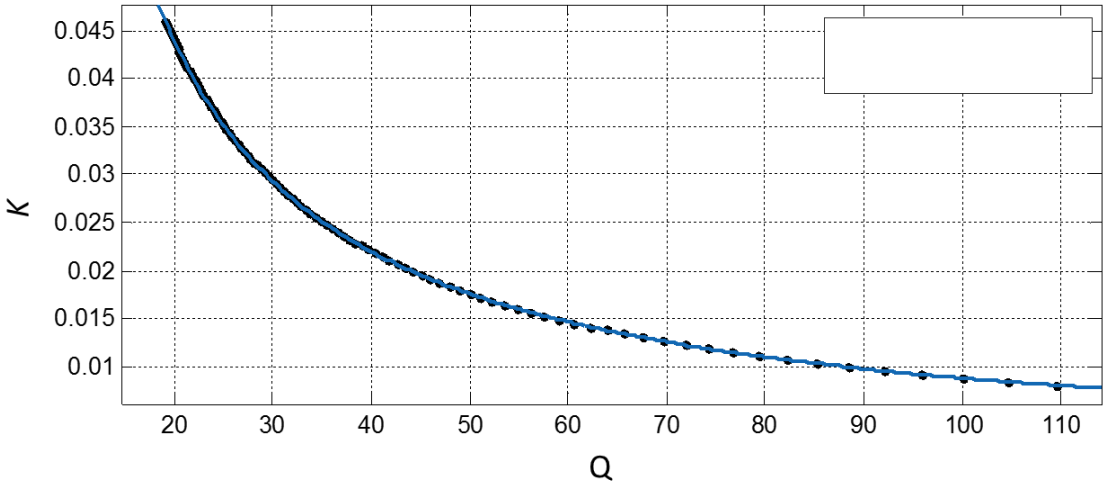

Figure A3.3 – Curve fit plot for *Q* versus *K* at 9 and 18 GHz. S_{11} max = -20dB, *n*=3

Matlab goodness of fit: SSE: 2.631e-32, R-square: 1. RMSE: 1.639e-17

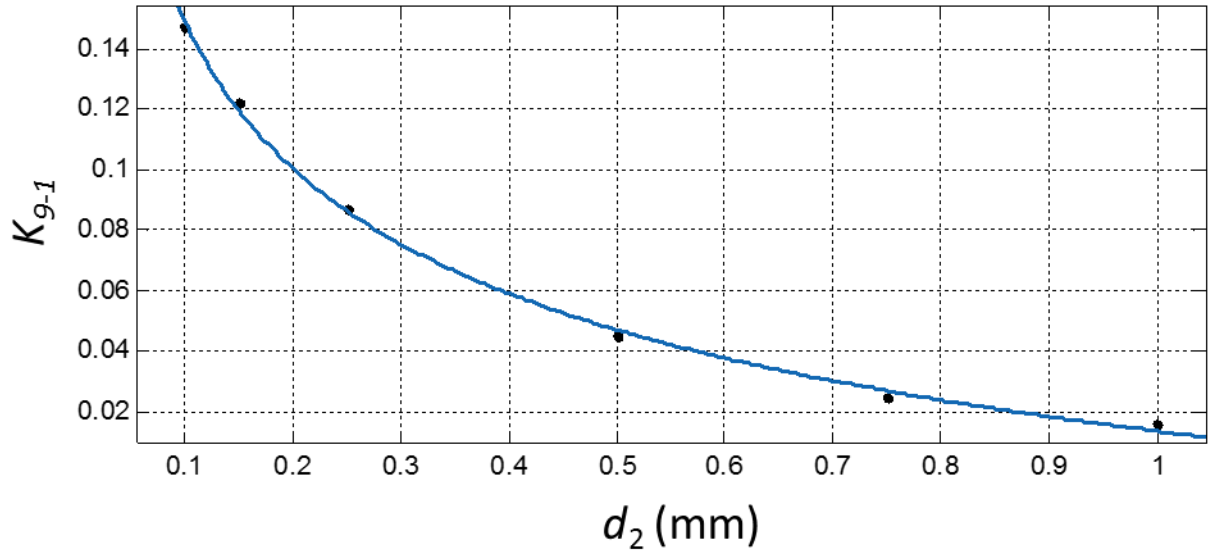

Figure A3.4 Curve fit plot for d_2 versus $K_{9\text{-}1}$

Matlab goodness of fit: SSE: 2.32e-5, R-square: 0.9973. RMSE: 0.002785

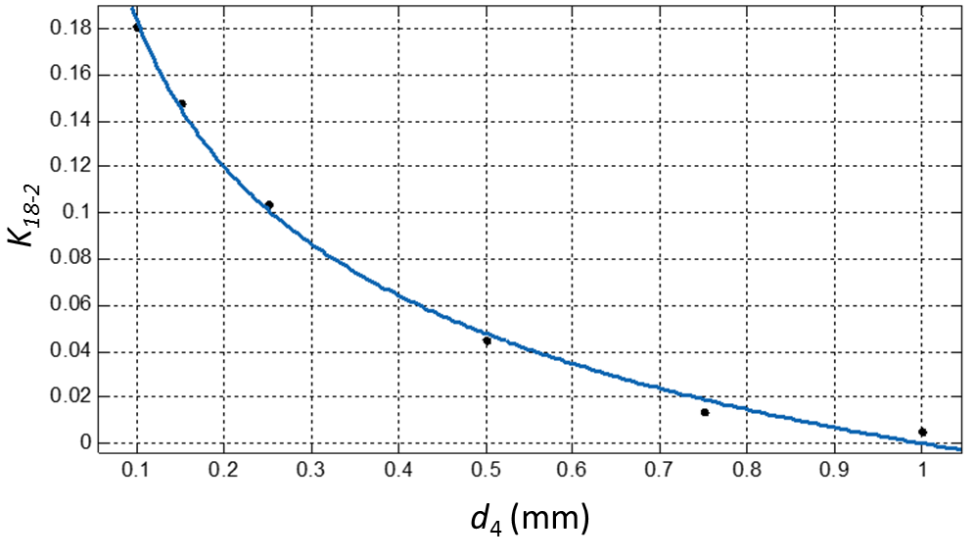

Figure A3.5 - Curve fit plot for d4 versus K18-2

Matlab goodness of fit: SSE: 7.616e-5, R-square: 0.9971. RMSE: 0.005039

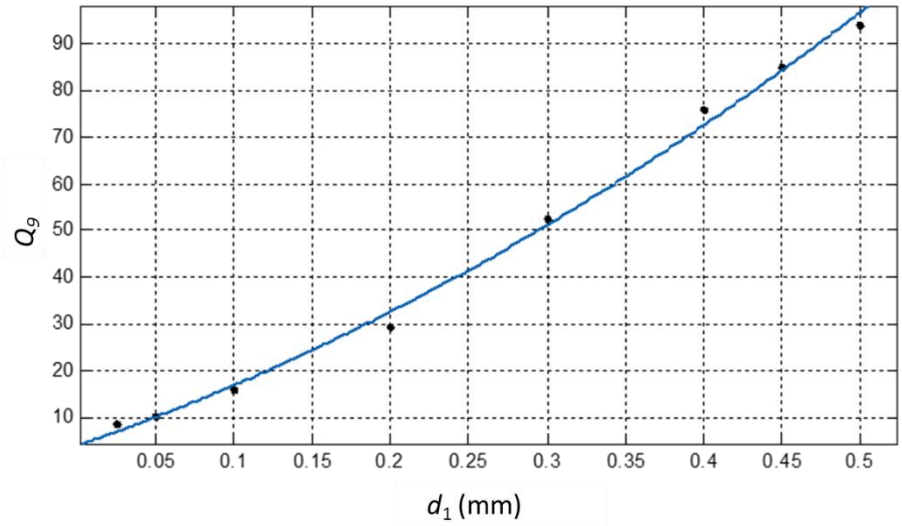

Figure A3.6 - Curve fit plot for d_1 versus Q_9

Matlab goodness of fit: SSE: 36.97, R-square: 0.9957. RMSE: 2.719

[i] MATLAB, The MathWorks Inc. 1 Apple Hill Drive, Natick, MA 01760-2098, UNITED STATES